

UCSF

UC San Francisco Electronic Theses and Dissertations

Title

Harnessing enzymatic activity for in vivo imaging and inhibitor discovery

Permalink

<https://escholarship.org/uc/item/6v35v903>

Author

Bardine, Conner Richard

Publication Date

2022

Peer reviewed|Thesis/dissertation

Harnessing Enzymatic Activity for In Vivo Imaging and Inhibitor Discovery

by
Conner Bardine

DISSERTATION
Submitted in partial satisfaction of the requirements for degree of
DOCTOR OF PHILOSOPHY

in
Chemistry and Chemical Biology

in the
GRADUATE DIVISION
of the
UNIVERSITY OF CALIFORNIA, SAN FRANCISCO

Approved:

DocuSigned by:
Charles Craik Charles Craik
6F8EED39591F4A0... Chair

DocuSigned by:
Michael Evans Michael Evans

DocuSigned by:
Aimee Kao Aimee Kao
745CF57D40DB494...

Committee Members

Copyright 2022

By

Conner R. Bardine

Dedication

I dedicate this thesis to my parents and grandparents who worked hard to provide me with the opportunity to obtain an education, to my friends who supported and believed in me, and to my cat, Touka, who did the rest.

Acknowledgements

Sir Isaac Newton once said, “If I have seen further, it is by standing on the shoulders of giants.” This quote has always stuck with me because I have had many giants in my life, and it is through their many shoulders that I could stand tall and accomplish the work described in this thesis.

First and foremost, I must thank my thesis advisor and mentor, Charly Craik. In 2016, he bought my plane ticket to do an internship in his lab. In 2017, I joined the graduate program he helped create. In 2018, I joined his lab to carry out my thesis. He was among the most influential people in my life and I cannot be more grateful. Through him, I continually learned impactful and translational science, unwavering enthusiasm and optimism, and how to cherish all segments of my research. Without his support I would not be the scientist that I am today.

I am also extremely grateful for Mike Evans, who has been a mentor and advisor during my graduate career. I learned much from his mentorship, diligence, and expert perspectives. Without him, the science that I have worked so hard to develop would not have made anywhere as much impact as it has.

I have to thank André Luiz Pinto Guedes Lourenço, whose name is as long as the ways he has supported me. He has been a best friend, coworker, mentor, and brother to me. He has taught me much of the science and techniques I champion today and kept me consistently optimistic, enthralled, and productive in and out of the lab.

I must express gratitude towards Kaitlin Hulce who was my first mentor when I interned in the Craik Lab six years ago. I always admired the breadth and depth of not only her knowledge but her kindness as well, and to this day I view her as a source of inspiration. Without her I don't know if I would have ended up where I am today.

My cat, Touka, deserves many thanks for helping me get through graduate school, if only she could read this. I still remember going to the animal shelter the third day I moved to San Francisco during the heat of August five years ago. I did not even have all my furniture yet,

but I adopted a feisty two-month-old kitten who grew up with me these past five years. She became a rock that kept me grounded through graduate school, forest fires, an international pandemic, and so much more. I appreciate the many hours she spent on zoom meetings with me during all my project meetings

I wish to acknowledge the many other coworkers and friends I have made along the way. If I named everyone specifically, this acknowledgment section would be its own chapter. So many people in the Craik Lab, in collaborator's labs, and on my thesis Committee, *etc* have made Genentech Hall not just a place I carry out science, but a place where I've formed strong relationships, grew as a person, and hopefully became a giant whose shoulders can be stood on so that the people who come after me can see further.

Contributions

Chapter 1 of this thesis is a reprint of the material as it appears in:

Ning Zhao, **Conner Bardine**, André Luiz Lourenço, Yung-hua Wang, Yangjie Huang, Simon J. Cleary, David M. Wilson, David Y. Oh, Lawrence Fong, Mark R. Looney, Michael J. Evans, and Charles S. Craik. *ACS Central Science*, 2021 7 (10), 1638-1649. DOI: 10.1021/acscentsci.1c00529

Chapter 2 of this thesis is a manuscript under preparation and the work was completed in collaboration with Joseph Blecha, Marie-Caline Abadijan, Henry Vanbrocklin, Christopher Drake, and Charles S. Craik.

Chapter 3 of this thesis is a manuscript under preparation and the work was completed in collaboration with Elissa A. Fink, Stefan Gahbauer, Isha Singh, Kris White, Shuo Gu, Xiaobo Wan, Beatrice Ary, Isabelle Glenn, Henry O'Donnell, Jiankun Lyu, Seth Vigneron, Nicholas Young, Yuroo Moroz, Jack Tauton, Adam Renslo, John J. Irwin, Adolfo Gastia-Sastre, Brian K. Schoichet, and Charles S. Craik.

Harnessing enzymatic activity for in vivo imaging and inhibitor discovery

By

Conner R. Bardine

Abstract

Enzyme function is ubiquitous in living organisms. Assays and biomarkers utilizing enzyme activity have become a pillar of chemical biology with relevance to the discovery of new biology, clinical diagnostics, and streamlining research and industrial pipelines. This thesis project seeks to develop assays and probes harnessing enzyme activity to expand the current repertoire of biomarkers and inhibitory drugs.

Chapter 1 describes restricted interaction peptides (RIPs) as a platform technology for tracking protease activity in vivo in real time. We show the proof of concept for this, as we harness the catalytic activity of proteases for tracking various biological events and disease states. This chapter evinces the most characterized and furthest along adaptation of the RIP technology, tracking immune activation via imaging with positron emission tomography (PET) by harnessing granzyme B (GZMB) catalysis

Chapter 2 continues the concept of harnessing enzyme activity to aid the field of nuclear medicine and radioimaging by detailing the development of a lipoic acid ligase that conjugates radiofluorine onto proteins of interest that contain a specific peptide substrate sequence. This approach would potentially expand the toolbox and broaden the pipelines of proteins amenable to radioimaging.

Chapter 3 describes the inhibition, as opposed to the amplification, of enzyme activity by developing substrates and enzyme functional assays for screening inhibitory drugs against the SARS-CoV-2 major protease (Mpro).

Table of Contents

1. In Vivo Measurement of Granzyme B Proteolysis from Activated Immune Cells with PET	1
1.1 Abstract	2
1.2 Introduction	3
1.3 Results	5
1.4 Discussion	21
1.5 Methods	23
1.6 Supplemental Figures	32
1.7 References	46
2. Enzymatic Radiolabeling of Biomolecules via an Engineered Lipoic Acid Ligase	53
2.1 Abstract	54
2.2 Introduction	55
2.3 Results	59
2.4 Discussion	76
2.5 Methods	77
2.6 References	80
3. Screening for Novel SARS-CoV-2 Major Protease Non-covalent and Covalent Inhibitors	85
3.1 Abstract	86
3.2 Introduction	87
3.3 Results	88
3.4 Discussion	104
3.5 Methods	106
3.6 Supplemental Figures	113
3.7 References	124

List of Figures

Figure 1.1: The development and in vitro characterization of GRIP B, a restricted interaction peptide to measure GZMB proteolysis in vivo with imaging.	7
Figure 1.2: In vitro mechanism of action studies and the synthesis of ⁶⁴ Cu-GRIP B.	10
Figure 1.3: ⁶⁴ Cu-GRIP B detects T cell activation in vivo elicited by immune checkpoint inhibition.	13
Figure 1.4: ⁶⁴ Cu-GRIP B biodistribution in vivo is dependent on GZMB proteolytic activity.	15
Figure 1.5: Post treatment changes in tumoral uptake of ⁶⁴ Cu-GRIP B correlates with the magnitude of volumetric tumor response to CPI in wild type mice, not in GZMB ^{-/-} mice.	17
Figure 1.6: ⁶⁴ Cu-GRIP B PET detects secreted GZMB elicited by an endotoxin mediated inflammatory response.	20
Figure 1.S1: A heat map showing the preferred cleavage sites for recombinant human granzyme B as predicted with multiplex substrate profiling mass spectrometry where 1-8 represents P4-P4', respectively.	32
Figure 1.S2: Stacked HPLC traces showing the cleavage of GRIP B by recombinant human GZMB.	33
Figure 1.S3: Tryptophan insertion experiments and circular dichroism.	34
Figure 1.S4: The structure of DOTA-GRIP B.	35
Figure 1.S5. A plot showing the stability of ⁶⁴ Cu-GRIP B in mouse serum.	35
Figure 1.S6. An example of a compartmental analysis of tumoral uptake of ⁶⁴ Cu-GRIP B.	36
Figure 1.S7: Representative coronal ⁶⁴ Cu-GRIP B PET/CT images of mice bearing CT26 tumors and treated with vehicle or checkpoint inhibitors.	37
Supplemental Figure 1.S8: Analytical HPLC data showing synthesis of ⁶⁴ Cu-D-GRIP B.	38
Figure 1.S9: Immunofluorescence data showing increased staining for the neutrophil marker Ly6G in LPS versus vehicle treated lung tissue.	39
Figure 2.1: Summary of [¹⁸ F]FPOA Radiosyntheses Using Precursors 1, 3, 5, and 6.	60

Figure 2.2: ^{W37I} LpIA Production.	68
Figure 2.3: Michaelis-Menten curve for freshly prepared ^{W37I} LpIA stock solution.	70
Figure 2.4: Michaelis-Menten curves for ^{W37I} LpIA solutions stored at 4 °C and -80 °C for 2 months.	71
Figure 2.5: Imaging of transgenic TNF α mice.	76
Figure 3.1: Substrate design for assay development.	90
Figure 3.2: Non-covalent compound optimization to low-μM potencies.	94
Figure 3.3: Covalent hits from 6.5 million virtual screen.	100
Figure 3.4: Compound optimization of aldehyde '3620.	102
Figure 3.5: Antiviral activity and pan-coronaviral MPro inhibition by covalent analogs.	104
Figure 3.S1: Solvent effect on enzymatic activity.	117
Figure 3.S2.1: Non-covalent docking hits from first virtual screen.	118
Figure 3.S2.2: Non-covalent docking hits from first virtual screen.	119
Figure 3.S2.3: Non-covalent docking hits from second virtual screen.	120
Figure 3.S2.4: Non-covalent docking hits from second virtual screen.	121
Figure 3.S3: Docked poses of covalent hits.	122
Figure 3.S4: Pan-viral enzymatic activities.	123

List of Tables

Table 1.S1: A tabular representation of the biodistribution data collected at various time points post injection of ^{64}Cu -GRIP B in tumor naïve male C57BL/6 mice.	40
Table 1.S2: A summary of the SUVmean values acquired from region of interest analysis of dynamic PET acquisitions.	41
Table 1.S3: A tabular representation of the biodistribution data collected 2h post injection of radiotracer ^{64}Cu -L-GRIP B in male balb/c mice bearing CT26 tumor after receiving 3 antibody/PBS treatment.	42
Table 1.S4: Biodistribution data collected 2 hours post injection of ^{64}Cu -D-GRIP B in male C57Bl6 mice bearing MC38 tumors.	43
Table 1.S5: Biodistribution data collected 2 hours post injection of ^{64}Cu -D-GRIP B in male C57Bl6 mice bearing MC38 tumors.	43
Table 1.S6: Biodistribution data collected 2 hours post injection of ^{64}Cu -GRIP B in female Balb6 mice bearing EMT6 tumors.	44
Table 1.S7: Biodistribution data collected 2 hours post injection of ^{64}Cu -D-GRIP B in female Balb6 mice bearing EMT6 tumors.	44
Table 1.S8: Biodistribution data collected 2 hours post injection of ^{64}Cu -GRIP B in male or female GZMB-/- mice bearing CT26 tumors.	45
Table 1.S9: A summary of the biodistribution data acquired in C57Bl6 mice subjected to an intratracheal instillation of lipopolysaccharide at 0.1 or 3 mg/kg.	45
Table 2.1: Published conditions for the formation of carbon 18-F bonds.	57
Table 2.2: Summary of ELIXYS Sequence for [^{18}F]FPOA Synthesis.	64
Table 2.3: Summary of [^{18}F]FPOA Qualification Syntheses.	65
Table 2.4: Materials Required for [^{18}F]FPOA Radiosynthesis.	66
Table 3.1: Hits from the first non-covalent docking screen.	92
Table 3.2: Hits from the second non-covalent docking screen.	97

Table 3.S1: All compound tested from docking screens and compound optimization.	113
Table 3.S2. Analogs of covalent docking hit '3620 with improved potencies.	114-116
Table 3.S3. Antiviral activities.	117
Table 3.S4. Pan-viral enzymatic activities of '7021.	117

CHAPTER 1

IN VIVO MEASUREMENT OF GRANZYME B PROTEOLYSIS FROM ACTIVATED IMMUNE CELLS WITH PET

IN VIVO MEASUREMENT OF GRANZYME B PROTEOLYSIS FROM ACTIVATED IMMUNE CELLS WITH PET

1.1 Abstract

The biology of human granzymes remains enigmatic in part due to our inability to probe their functions outside of in vitro assays or animal models with divergent granzyme species. We hypothesize that the biology of human granzymes could be better elaborated with a translational imaging technology to reveal the contexts in which granzymes are secreted and biochemically active in vivo. Here, we advance toward this goal by engineering a Granzyme targeting Restricted Interaction Peptide specific to family member B (GRIP B) to measure secreted granzyme B (GZMB) biochemistry with positron emission tomography. A proteolytic cleavage of ^{64}Cu -labeled GRIP B liberates a radiolabeled form of Temporin L, which sequesters the radioisotope by binding to adjacent phospholipid bilayers. Thus, at extended time points postinjection (i.e., hours, not seconds), tissue biodistribution of the radioisotope in vivo reflects relative units of the GZMB activity. As a proof of concept, we show in three syngeneic mouse cancer models that ^{64}Cu -GRIP B detects GZMB from T cells activated with immune checkpoint inhibitors (CPI). Remarkably, the radiotracer detects the proteolysis within tumors but also in lymphoid tissue, where immune cells are activated by a systemic CPI. Control experiments with an uncleavable analogue of ^{64}Cu -GRIP B and tumor imaging studies in germline GZMB knockout mice were applied to show that ^{64}Cu -GRIP B is specific for GZMB proteolysis. Furthermore, we explored a potential noncytotoxic function for GZMB by applying ^{64}Cu -GRIP B to a model of pulmonary inflammation. In summary, we demonstrate that granzyme biochemistry can be assessed in vivo using an imaging modality that can be scaled vertically into human subjects.

1.2 Introduction

The human granzymes consist of five serine proteases (A, B, H, K, M) that are expressed primarily within the secretory vesicles (i.e., granules) of lymphocytes involved in the host defense, namely, natural killer (NK) and cytotoxic T cells (CTLs).¹ In these cell types, granzymes are best understood to be pro-apoptotic effectors against problematic cells, for example, cancer cells or cells infected with pathogens. To impart cytotoxicity, lymphocytes degranulate after docking with a target cell to release granzymes transiently into a pericellular space.^{2,3} Co-secreted with granzymes are perforin molecules, which form a channel in the plasma membrane of the target cell to facilitate the granzyme transit into the cytoplasm.⁴ Granzyme biochemistry subsequently triggers cell death through several mechanisms, for example, proteolytic activation of caspases or direct DNA damage (granzyme B), and SET-mediated activation of DNA cleavage (granzyme A).⁵⁻⁸

Despite decades of research, granzymes in many ways remain an enigmatic enzyme class. For example, virtually no biological functions are defined for the so-called “orphan” granzymes H, K, and M.⁹ Moreover, the secretion of granzymes (including A and B) in abundance during conditions unrelated to host defense has suggested noncytotoxic signaling functions.¹⁰ These data align with a developing narrative suggesting that dysregulated granzyme secretion and proteolysis may contribute to the pathobiology of chronic human disorders, for example, systemic autoimmune diseases.¹¹ Thus, the canon that granzymes are primarily cytotoxic effectors is being challenged by a more complex biological model in which secreted granzymes can also persist in extracellular space to perform noncytotoxic signaling functions.

More fully elaborating the complex biology of granzymes is challenging in part due to the inadequacy of preclinical models to study their functions.¹² In vitro coculture approaches are reductionist models of the more elaborate multicellular conversation occurring in human immunology. In vivo mouse models, for example, germline knockout mice, have revealed roles

for granzymes A and B in host defense, but they carry with them the caveat that mice express a larger repertoire of granzymes than humans, which may confound efforts to reveal other granzyme functions due to compensatory effects. Moreover, mouse granzymes are evolutionarily divergent from their human counterparts and bear different protein substrate preferences.¹³ Thus, any findings in mice by nature will require some corroboration in human cell lines and patients. Collectively, these considerations underscore that an expansion of our knowledge of granzyme biology will ultimately require *in vivo* technologies that can also be scaled to humans.

In humans, studies of granzymes are generally limited to expression analysis at the protein and mRNA level in biopsied tissue or from biofluids. Missing from the field are technologies that enable measurements of granzyme biochemistry *in vivo* with a spatiotemporal control. We hypothesized that an imaging tool could address this unmet need were it capable of selectively capturing when and where immune cells present biochemically active granzymes in the extracellular niche.

Although inducible fluorescent imaging probes have a rich history in biomedical research as tools to study protease biology, the limited sensitivity and resolution of fluorescent tomography limits its application in clinically relevant animal models and humans.^{14,15} Nuclear imaging with positron emission tomography (PET) offers an attractive alternative, as γ -photons are not scattered by tissue and thus produce high-resolution tomographic images of deep tissues. However, developing a protease-activated radiotracer for PET comes with the special design challenge that radioactive decay is continuous and cannot be masked and then conditionally revealed by a proteolytic event. We proposed instead to design an imaging probe in which enzyme catalysis causes probe sequestration in nearby tissues, akin to the biochemical trapping mechanism utilized for metabolic radiotracers like ¹⁸F-fluorodeoxyglucose.

We hypothesized that a “restricted interaction peptide” (RIP) specifically cleaved by an extracellular granzyme could be leveraged to enable *in vivo* measurements of biochemistry on

PET.¹⁶ In general, RIPs consist of three domains from N to C terminus, namely, (1) a nontoxic antimicrobial peptide (AMP) coupled to a radioisotope, (2) a specific endoprotease cleavage site, and (3) a peptide “masking” domain that prevents the AMP from adopting its preferred helical conformation that tightly binds phospholipid bilayers ([Figure 1A](#)). Upon proteolytic cleavage of the full length, pro-peptide form of the RIP, the radiolabeled AMP is liberated, undergoes a spontaneous conformational shift, and deposits within any nearby membrane.

1.3 Results

To identify an optimal cleavage sequence to install in a RIP targeting GZMB, we performed multiplex substrate profiling using mass spectrometry (MSP-MS) against recombinant human GZMB.^{17,18} The MSP-MS library contains 228 tetradecameric peptides, which is a physicochemically diverse population of rationally designed substrates with maximum sequence diversity (**Fig. 1.1b**). On the basis of the observation that most proteases require two optimally positioned amino acids for substrate recognition and cleavage, physicochemical diversity was generated in the peptide library through an incorporation of all neighbor (XY) and near–nearbor (X*Y, X**Y) amino acid pairings. With an incubation of native GZMB at various time points, cleavages were identified by peptide sequencing via liquid chromatography tandem mass spectrometry (LCMS-MS).¹⁹ A statistical analysis that considers both cleaved and uncleaved positions in the peptide library was subsequently performed to construct an iceLogo representation of the preferred substrate sequence spanning the granzyme B P4–P4' sites (**Fig. 1.1c, Supplemental Fig 1.S1**).

The iceLogo results suggested that four sequences with conserved sites of P2 = P and P1 = D (i.e., XXPDXXXX) were equally specific and efficient GZMB substrates. Of these, we nominated the sequence IEPDVSQV for two reasons. First, the P4–P1 sequence was previously discovered by our group to be specific to GZMB using an orthogonal approach, namely, a positional scanning synthetic combinatorial library, and we showed this sequence is specifically recognized by GZMB versus other human granzymes.^{20,21} Second, the IEPD

tetrapeptide has been studied in vivo as part of a covalent reversible aldehyde radiotracer targeting GZMB, and the tetrapeptide aldehyde appeared to be effective at labeling GZMB and stable in vivo.^{22,23}

The kinetics of IEPDVSQV cleavage by GZMB was assayed in vitro using a fluorescent quenched peptide substrate, and the incorporation of the P1'-P4' sequence VSVQ significantly improved the catalytic efficiency (kcat/Km) compared to previously reported values for IEPD alone (~8000 vs ~3300 M⁻¹ s⁻¹, see **Fig. 1.1d**).²¹ Furthermore, the GZMB-optimized substrate was incubated with various other relevant proteases (**Fig. 1.1e**). No cleavage was observed with any of these proteases after 1 h compared to significant cleavage by GZMB, highlighting the specificity of the optimized GZMB cleavage sequence. To generate the full-length GRIP B probe, we chose to flank this sequence using Temporin L as the membrane-interacting domain and the PAR1 peptide as the masking domain (**Fig. 1.1f**).¹⁶ Importantly, the full-length GRIP B was efficiently cleaved by a recombinant human GZMB showing that neither Temporin L nor the masking domain interfered with the proteolysis (**Supplemental Figure 1.S2**).

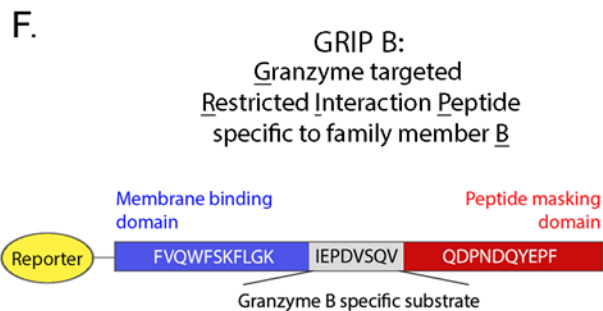
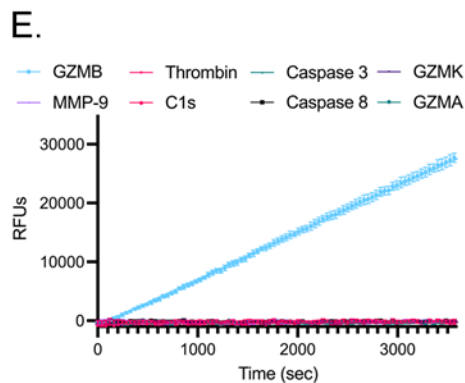
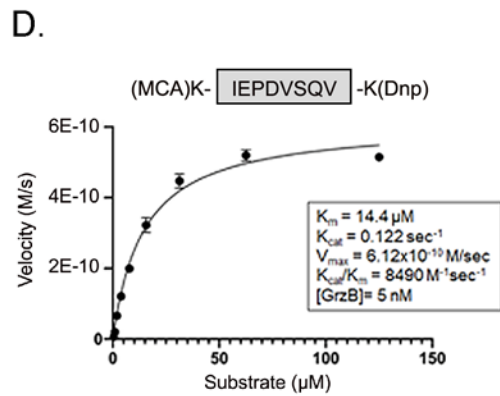
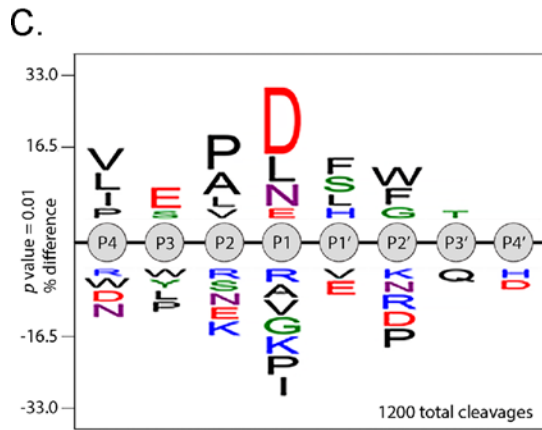
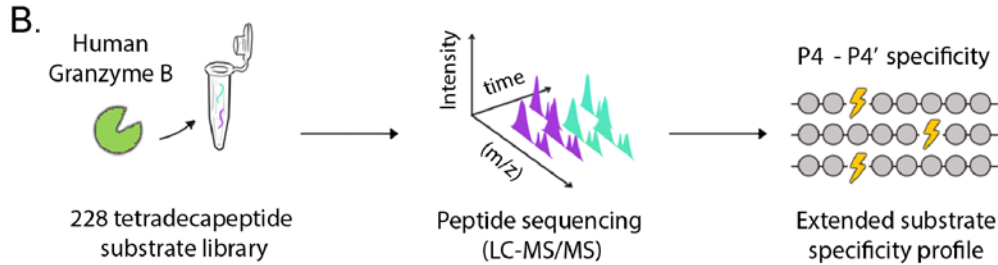
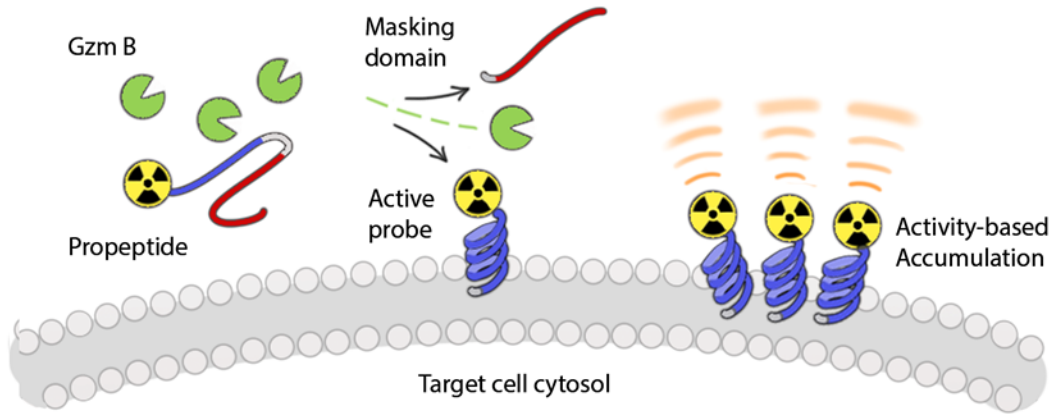
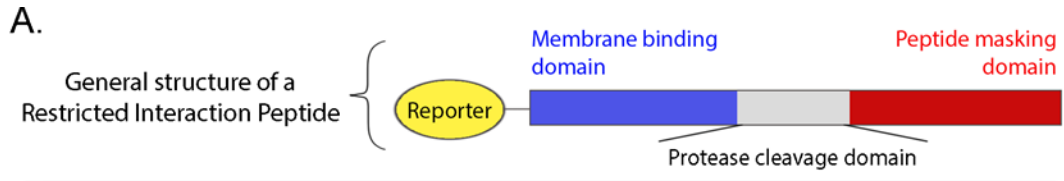


Figure 1.1: The development and in vitro characterization of GRIP B, a restricted interaction peptide to measure GZMB proteolysis in vivo with imaging. **a.** A schematic showing a generalized structure of a restricted interaction peptide, and the in vivo mechanism of action. Cleavage of the full length pro-form by a dedicated endoprotease liberates a tagged (e.g. radiolabeled) antimicrobial peptide, which irreversibly interacts with nearby phospholipid membranes. Thus, the stable accumulation of peptide at extended time points post injection (i.e. hours, not seconds) can reflect the relative units of enzyme activity in a region of interest. **b.** A schema showing the workflow of the MSP-MS study to identify a GZMB cleavage sequence. Proteolytic products from GZMB activity were produced by incubating the enzyme with a physicochemically diverse library of 228 tetradeca-peptides. Peptide sequencing by LC-MS/MS allowed for the determination of GZMB generated cleavages. **c.** An iceLogo showing the consolidated results of an MSP-MS analysis of the P4-P4' substrate preferences for human GZMB. **d.** A plot showing the Michaelis-Menten kinetics of human granzyme B proteolysis of the IEPDVSVQ peptide. Coverage of the non-prime and prime sites of GZMB yielded an optimized substrate with improved catalytic turnover by approximately 2-fold compared to IEPD alone. **e.** A plot showing the IEPDVSVQ peptide is specifically cleaved by GZMB and not by various other relevant proteases. **f.** The final amino acid sequence of GRIP B

We confirmed that the proteolytically cleaved version of GRIP B effectively bound membranes. A N-terminal, 5FAM-tagged version of GRIP B was synthesized and incubated with viable MC38 cells and recombinant human granzyme B or vehicle. Flow cytometry showed that the intact GRIP B had a low interaction with cell membranes, while a preincubation of GRIP B with 20 nM recombinant GZMB, followed by a coincubation with MC38 cells in Hanks' Balanced Salt Solution (HBSS) at 37 °C for 30 min, resulted in fluorescently labeled cell membranes (**Fig. 1.2a**). The insertion of the cleaved GRIP B peptide into lipid micelles was further confirmed by measuring the intrinsic tryptophan fluorescence (**Supplemental Fig. 1.S3a**). Circular dichroism data of full-length GRIP B are indicative of a disordered peptide, showing the efficacy of the masking domain to disrupt the α -helical secondary structure (**Supplemental Fig. 1.S3b**). Circular dichroism of activated GRIP B confirms that the activated peptide retains the α -helical secondary structure of the cell-penetrating peptide Temporin L upon cleavage of the masking domain (**Supplemental Fig. 1.S3c**). Lastly, we verified that full-length or proteolytically cleaved GRIP B did not display toxicity toward human red blood cells in vitro (**Fig. 1.2b**).

To couple GRIP B to a chelator for radiolabeling, the peptide was reacted with 1,4,7,10-tetraazacyclododecane-1,4,7,10-tetracetic acid mono-*N*-hydroxysuccinimide ester (DOTA-NHS-ester) on a solid support, which ligated to the amino group on the N-terminal phenylalanine. DOTA-GRIP B was subsequently deprotected, cleaved from the resin, and purified with semiprep high-performance liquid chromatography (HPLC) (**Supplemental Fig. 1.S4**).

DOTA-GRIP B was next radiolabeled with copper-64, since its half-life ($t_{1/2} \approx 13$ h) would enable studies over a long window of time post injection to identify the optimal time point for imaging. $^{64}\text{CuCl}_2$ was incubated with DOTA-GRIP B in 4-(2-hydroxyethyl)-1-piperazineethanesulfonic acid (HEPES) buffer for 30 min at room temperature. The reaction was monitored for completeness via instant thin-layer chromatography and purified using HPLC (**Fig. 1.2c**). The decay-corrected yield was consistently greater than 95%, with a purity of greater than 99%. The specific activity was ~ 0.4 Ci/ μmol over three radiosyntheses. An incubation of ^{64}Cu -GRIP B with the recombinant human GZMB showed a conversion within 30 min to one radiolabeled product that comigrated on the HPLC with the cold-cleaved DOTA-peptide fragment (**Fig. 1.2d**). Lastly, the serum stability was tested in vitro in mouse serum. We observed on HPLC that ^{64}Cu -GRIP B was greater than 98% stable over 4 h at 37 °C (**Supplemental Fig. 1.S5**).

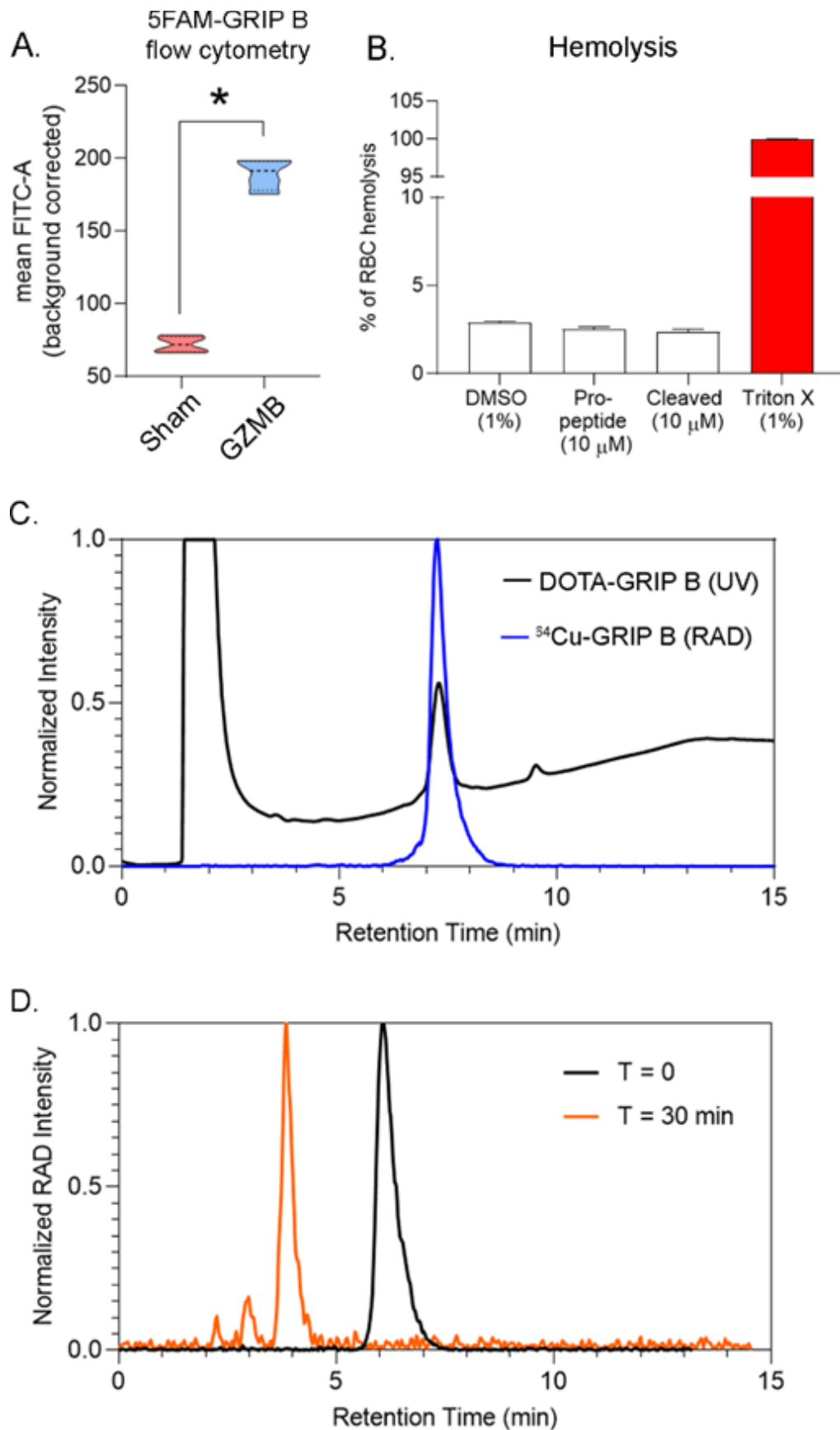


Figure 1.2: In vitro mechanism of action studies and the synthesis of ⁶⁴Cu-GRIP B. **a.** Mean fluorescence intensity data showing the extent of cell labeling by 5FAM-GRIP B in the presence or absence of GZMB by incubation at 37°C for 30min. The data were collected using MC38 cells in triplicate. *P<0.01. **b.** A bar graph representing the extent of red blood cell lysis due to treatment with vehicle (0.1% DMSO), the full length GRIP B pro-peptide, and the proteolytically activated truncated peptide. Triton-X is included as a positive control. **c.** An HPLC trace showing the overlay of the radioactive trace (blue) with the UV trace of the DOTA-GRIP B precursor. The trace was collected 30 min after the start of the reaction. **d.** A radioactive HPLC trace showing the conversion of ⁶⁴Cu-GRIP B to one major product after a 30 min incubation with 400 nM recombinant human GZMB.

To understand tracer pharmacokinetics and normal tissue biodistribution, we first injected ⁶⁴Cu-GRIP B intravenously in balb/c mice and conducted a 60 min dynamic PET acquisition (**Fig. 1.3a**). A region-of-interest analysis showed the probe cleared from a blood pool with $t_{1/2} \approx 8$ min. The dominant mode of clearance was renal, and as with the thrombin RIP probe, the only substantial radiotracer accumulation outside of the kidneys was observed in the liver. We next conducted a biodistribution to evaluate the radiotracer distribution in normal tissues out to 24 h postinjection. The biodistribution data corroborated the imaging findings showing the highest level of tissue-associated activity in the kidney and liver (**Supplemental Table 1.S1**).

We evaluated the effect of immunomodulatory therapies on the ⁶⁴Cu-GRIP B biodistribution in mice bearing subcutaneous CT26 tumors, a mouse colorectal cancer cell line.²⁴ Mice were treated with three intraperitoneal infusions of vehicle or anti-PD1 plus anti-CTLA4 checkpoint inhibitors (CPIs) over 11 d. The radiotracer was injected on day 14, and the tumor uptake was monitored over several time points out to 24 h postinjection on PET. An ROI analysis of static PET/computed tomography (CT) images showed that the ⁶⁴Cu-GRIP B uptake in the treated tumors steadily rose from 0.5 to 2–4 h postinjection (Figure 3B). Notably, the radioactivity persisted in tumors out to 24 h postinjection, which is consistent with a mechanism of irreversible radiotracer trapping at the tumor. Moreover, the tumoral uptake of ⁶⁴Cu-GRIP B was significantly higher in the CPI versus vehicle-treated arm at 2 h postinjection. Time activity curves derived from a dynamic PET acquisition showed that the tumoral

accumulation of ^{64}Cu -GRIP B in CPI-treated mice was rapid, reaching a level of $\sim 5\%$ ID/cc within 10 min postinjection (**Fig. 1.3c, Supporting Table 1.S2**). Furthermore, a compartmental modeling showed that $k_3 \gg k_4$ and $k_4 \approx 0$, which are properties known to be associated with radiotracers like ^{18}F -fluorodeoxyglucose that are irreversibly sequestered in tissues (**Supplemental Fig. 1.S6**).²⁵ By comparison, the radiotracer uptake in vehicle tumors was significantly lower and did not change over time.

We conducted a biodistribution study at 2 h postinjection to determine relative changes in tracer uptake between tissues in the vehicle and treated groups. These data showed $\sim 50\%$ induction of radiotracer uptake in the tumors from treated mice compared to control mice (Figure 3D, Supporting Information Figure 7, and Supporting Information Table 2). We also observed a significant increase in the tracer uptake within the spleen, which is consistent with a stimulation of T cells by systemic immune CPIs that we and others have documented.^{26–28} Digital autoradiography (DAR) showed that ^{64}Cu -GRIP B was significantly higher in the treated versus control tumor. Although the comparatively lower resolution of pseudocolor from DAR limits the ability to rigorously compare the GRIP B localization to the GZMB protein expression on immunofluorescence (IF), qualitatively the regions of the radiotracer binding in tissue appeared to coalign with the expression of GZMB and the T cell marker CD3 (**Fig. 1.3e**).

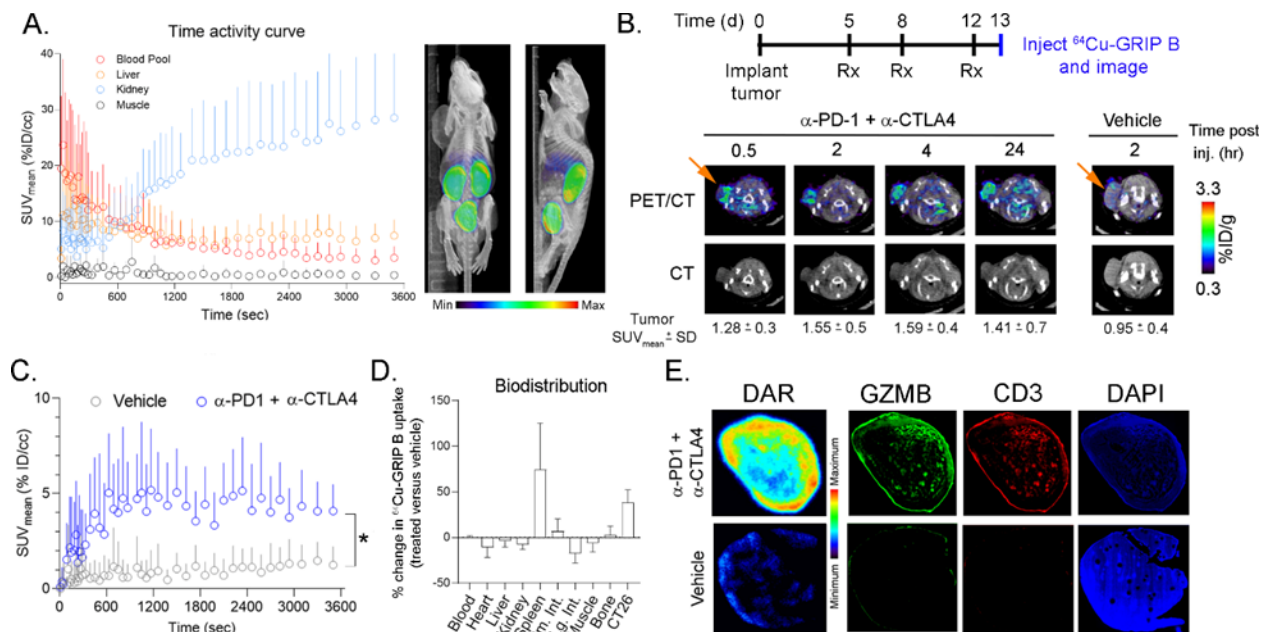


Figure 1.3: ^{64}Cu -GRIP B detects T cell activation in vivo elicited by immune checkpoint inhibition. **a.** A time activity curve showing the renal clearance of ^{64}Cu -GRIP B in a male C57Bl6 mouse bearing a subcutaneous CT26 tumor. **b.** Representative transaxial CT and PET/CT images showing the accumulation over time of ^{64}Cu -GRIP B in a CT26 tumor exposed to anti-PD1 and anti-CTLA4 CPI. Also shown is the uptake of ^{64}Cu -GRIP B in a tumor bearing mouse treated with vehicle. **c.** A time activity curve from a dynamic PET acquisition showing the tumoral uptake of ^{64}Cu -GRIP B in CT26 tumors from mice treated with vehicle or CPI. * $P < 0.05$ **d.** A plot showing the % change in ^{64}Cu -GRIP B uptake per organ in treated versus untreated mice. **e.** Digital autoradiography and immunofluorescence showing the co-localization of ^{64}Cu -GRIP B with GZMB and T cells within CT26 tumor slices from mice exposed to vehicle or CPI.

We tested if the post-treatment changes in the tumoral uptake of ^{64}Cu -GRIP B are driven by the proteolysis of ^{64}Cu -GRIP B. To achieve this, we prepared ^{64}Cu -D-GRIP B, a probe that harbors a d-aspartic acid within the GZMB protease site (IEPdVSQV) to prevent cleavage by GZMB. The probe was functionalized with DOTA and radiolabeled with copper-64 using an approach similar to that for the synthesis of ^{64}Cu -GRIP B (**Supplemental Fig. 1.S8**). Biodistribution studies showed that the CPI treatment did not cause an increase in the tumoral uptake of ^{64}Cu -D-GRIP B compared to the control (Figure 4A).

We compared the biodistribution of ^{64}Cu -GRIP B or ^{64}Cu -D-GRIP B in mice bearing MC38 (mouse colorectal cancer) or EMT6 (mouse mammary breast carcinoma) xenografts. The mice were treated with vehicle or anti-PD1 and anti-CTLA4 CPIs following the schema used for the

CT26 cohort. Biodistribution data showed a significant increase in the tumoral uptake of ^{64}Cu -L-GRIP B in both cohorts, while ^{64}Cu -D-GRIP B was not induced in tumors compared to controls, as expected (**Fig. 1.4a** and **Supplemental Tables 1.S3–7**). Moreover, the absolute levels of the ^{64}Cu -D-GRIP B uptake in treated tumors were low and comparable with the baseline uptake of ^{64}Cu -L-GRIP B in untreated tumors (**Fig. 1.4b**). The basal ^{64}Cu -D-GRIP B uptake in the spleen was also low and unaffected by a treatment with immune checkpoint inhibitors (**Fig. 1.4c,d**).

To confirm that GZMB is responsible for post-treatment changes in the ^{64}Cu -GRIP B biodistribution, we inoculated germline homozygous GZMB knockout mice²⁹ with CT26 tumors and assessed the relative biodistribution of ^{64}Cu -L-GRIP B in mice after a treatment with a vehicle or CPIs. We observed no significant post-treatment changes in the radiotracer uptake among tumors and spleen exposed with CPI compared to vehicle (**Fig. 1.4e,f**, **Supplemental Table 1.S8**).

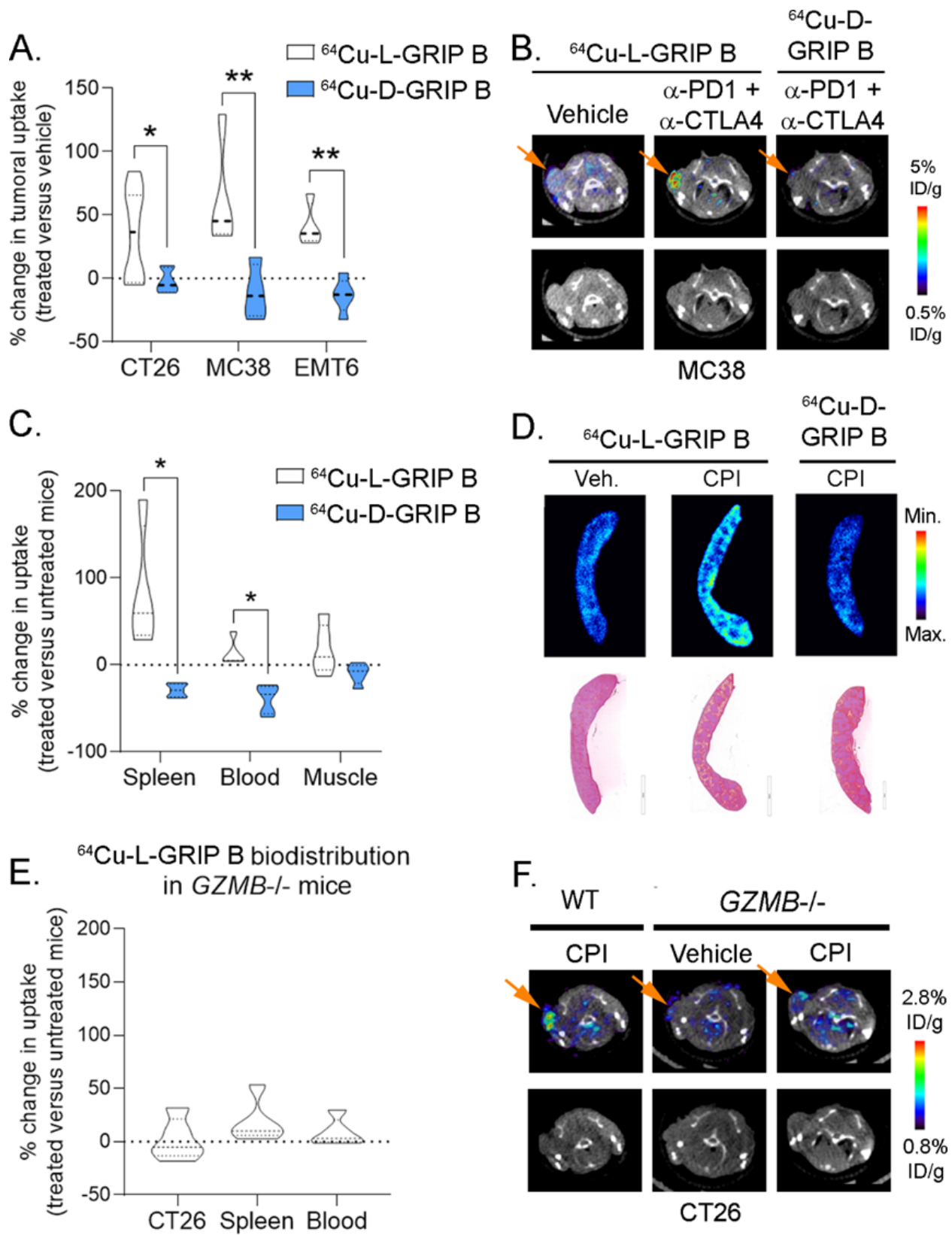


Figure 1.4: ⁶⁴Cu-GRIP B biodistribution in vivo is dependent on GZMB proteolytic activity.

a. A bar graph summarizing the post treatment effects on the tumoral uptake of ⁶⁴Cu-GRIP B (or ⁶⁴Cu-L-GRIP B) and ⁶⁴Cu-D-GRIP B, an uncleavable negative control tracer bearing D-amino acids in the GZMB cut site. Three cohorts of mice bearing subcutaneous CT26, MC38 or EMT6 mice were studied. CT26 and MC38 were implanted in male C57Bl6 mice, and EMT6 were implanted in female Balb/c mice. *P<0.05, **P<0.01. **b.** Representative transaxial PET/CT and CT images from the MC38 cohort showing the tumoral uptake of ⁶⁴Cu-L-GRIP B and ⁶⁴Cu-D-GRIP B in mice treated with vehicle or CPI. **c.** A bar graph showing the post treatment effects on the splenic uptake of ⁶⁴Cu-GRIP B and ⁶⁴Cu-D-GRIP B in mice treated with vehicle versus CPI. These data were taken from the CT26 cohort and similar trends were observed in the other mouse cohorts. *P<0.01 **d.** Autoradiography and H&E showing the relative intensity of ⁶⁴Cu-L-GRIP B and ⁶⁴Cu-D-GRIP B uptake in spleen sections. **e.** A bar graph summarizing the post treatment effects on the tumoral and splenic uptake of ⁶⁴Cu-GRIP B in germline *GZMB*^{-/-} treated with vehicle or CPI. The *GZMB*^{-/-} were inoculated with CT26 tumors for this study. **f.** Representative transaxial PET/CT and CT images from the CT26 cohort showing the tumoral uptake of ⁶⁴Cu-L-GRIP B in C57Bl6 mice treated with CPI or germline *GZMB*^{-/-} mice treated with vehicle or CPI.

Tumors enriched with comparatively higher levels of GZMB activity could be expected to more significantly debulk compared to GZMB-poor tumors. Thus, we next asked if post-treatment changes in the tumoral uptake of ⁶⁴Cu-GRIP B correlated with antitumor effects. The tumoral uptake of ⁶⁴Cu-GRIP B at day 11 was significantly anticorrelated with the percent change in tumor volume at day 11 compared to day 0 (**Fig. 1.5a**). ⁶⁴Cu-GRIP B tumor-to-blood ratios at day 11 also significantly correlated with the percent change in tumor volume. In contrast, neither the tumoral uptake nor the tumor-to-blood ratio of ⁶⁴Cu-GRIP B correlated with percent changes in the tumor volume in the *GZMB* knockout mouse background (**Fig. 1.5b**).

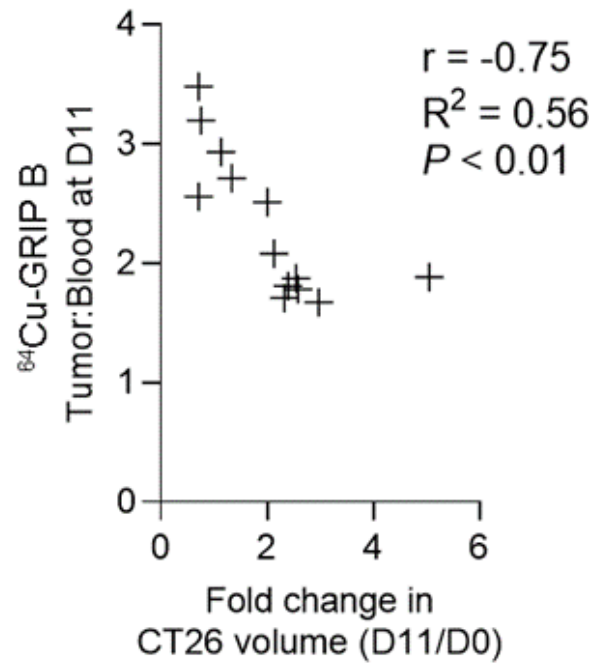
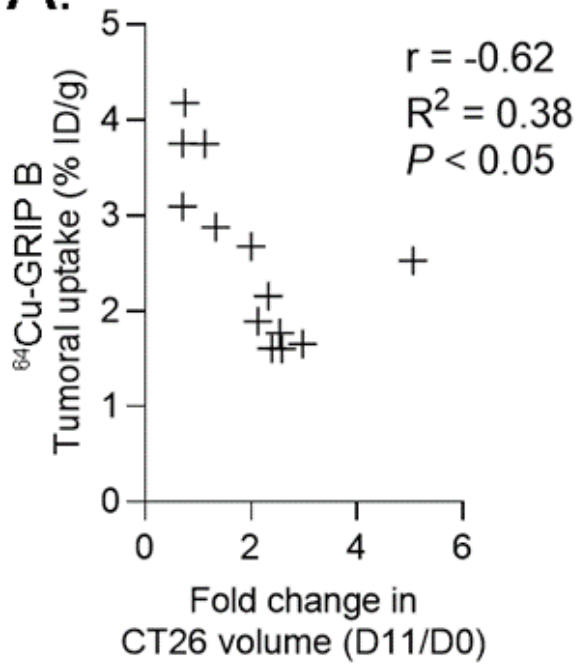
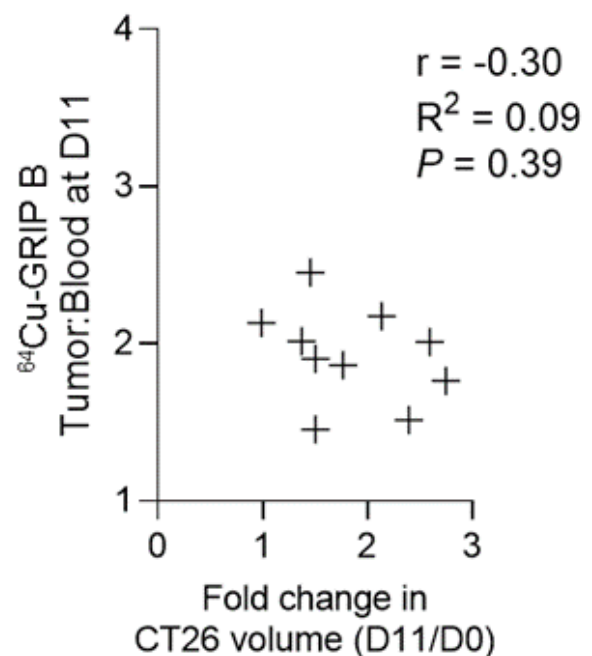
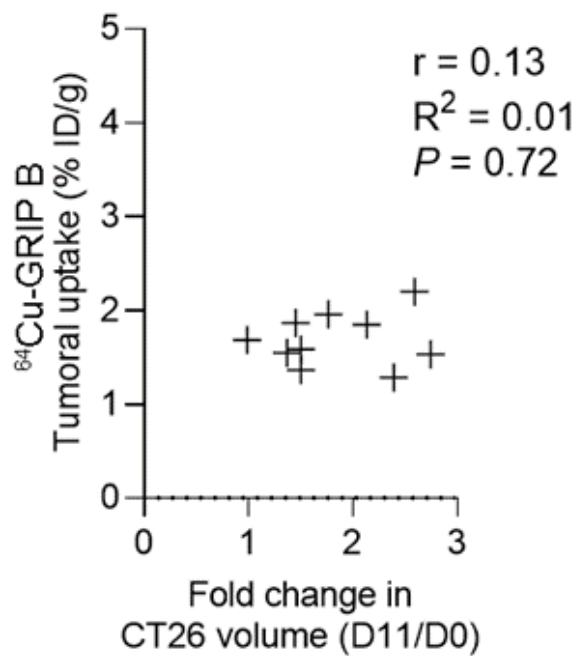
A.**Wild type mice****B.*****GZMB*^{-/-} mice**

Figure 1.5: Post treatment changes in tumoral uptake of ^{64}Cu -GRIP B correlates with the magnitude of volumetric tumor response to CPI in wild type mice, but not in GZMB-/- mice. **a.** Scatter plots showing the correlation between fold change in tumor volume from day 11 to day 0 and ^{64}Cu -GRIP B tumoral uptake (left) or tumor to blood ratio (right). The data were collected from two cohorts of wild type mice bearing CT26 tumors. **b.** Scatter plots showing the correlation between fold change in tumor volume from day 11 to day 0 and ^{64}Cu -GRIP B tumoral uptake (left) or tumor to blood ratio (right). The data were collected from two cohorts of GZMB-/- mice bearing CT26 tumors.

Though not well-defined, noncytotoxic functions for secreted GZMB have been proposed in several physiological processes, including inflammation.³⁰⁻³² To test if ^{64}Cu -GRIP B can localize potentially pathogenic reservoirs of secreted GZMB due to inflammation, we next performed ^{64}Cu -GRIP B PET/CT on wild-type mice that had received intratracheal instillations of lipopolysaccharide (LPS). PET/CT was performed 4 d after the instillation, a time point at which a T cell recruitment to the lungs has occurred.^{33,34} An ROI analysis showed a significantly higher radiotracer accumulation in the lungs of mice treated with low (0.1 mg/kg) and high (3 mg/kg) doses of LPS compared to a vehicle (**Fig. 1.6a,b**). Autoradiography and immunofluorescence of the lungs showed a visually higher radiotracer binding in the LPS-treated lung. Consistent with the autoradiography, the overall levels of GZMB, CD3, Ly6G, and NKp46/NCR1 staining were higher in the lung parenchyma of LPS versus vehicle-treated mice (**Fig. 1.6c, Supplemental Fig. 1.S9**).

We observed regions in the lung that were positive for GZMB but lacked evidence of ^{64}Cu -GRIP B binding. We hypothesize these regions harbor high levels of GZMB positive immune cells that are not actively secreting GZMB. Since 3 mg/kg LPS can trigger a system-wide T cell activation, we further examined a radiotracer uptake in a larger panel of mouse organs. Ex vivo biodistribution studies showed that ^{64}Cu -GRIP B was significantly higher in numerous tissues in the LPS-treated versus vehicle mice at either dose, including lymphoid organs like the spleen and thymus (**Fig 1.6d, Supplemental Table 1.S9**). Remarkably, the system-wide impact on T cell activation due to the intratracheal instillation of LPS was also

visually obvious by a comparison of maximum intensity projections between treatment arms
(Fig. 1.6e).

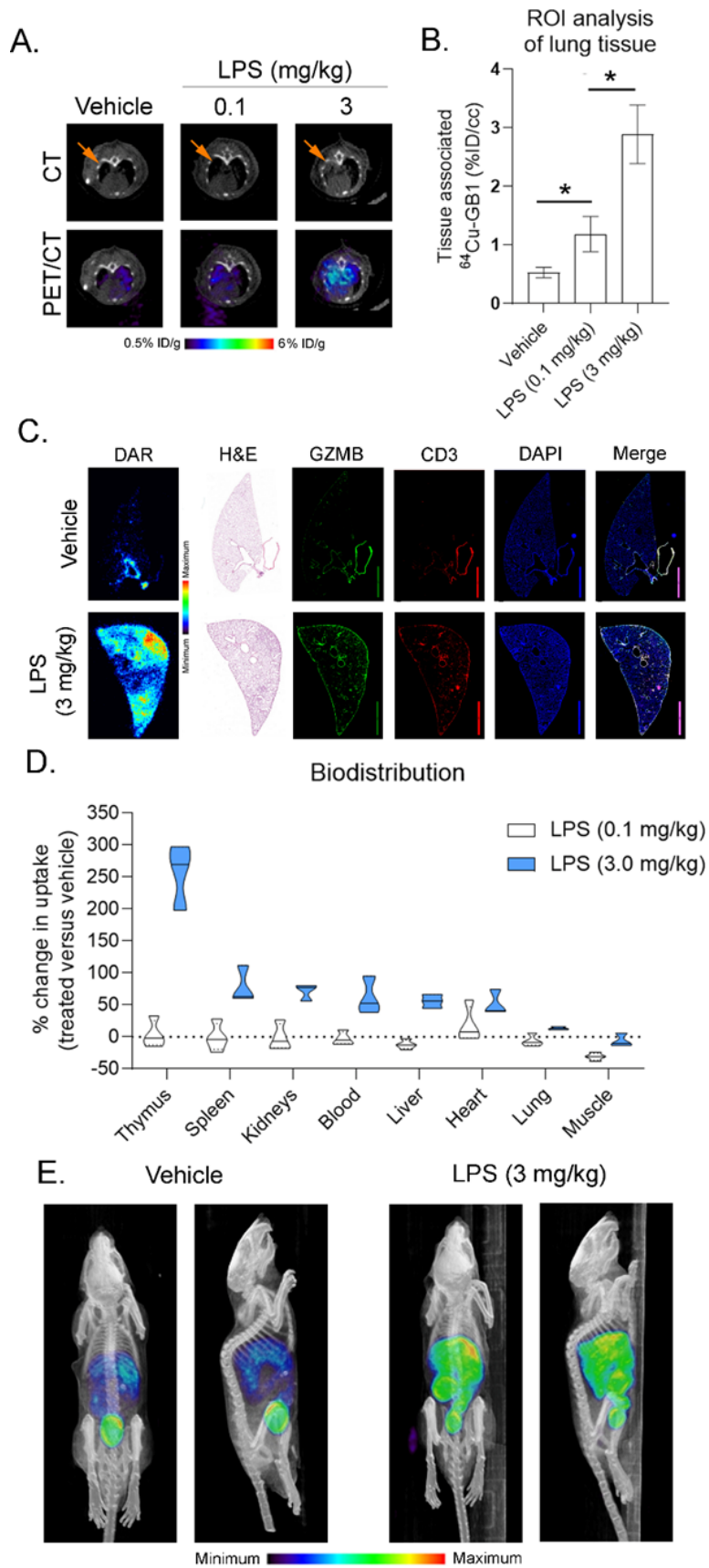


Figure 1.6: ⁶⁴Cu-GRIP B PET detects secreted GZMB elicited by an endotoxin mediated inflammatory response. **a.** Representative ⁶⁴Cu-GRIP B PET/CT studies showing higher radiotracer accumulation in the lungs of mice treated with 0.1 or 3.0 mg/kg LPS compared to mice that received sham. **b.** Region of interest analysis of the right lung lobe shows significantly higher radiotracer uptake in LPS treated versus sham treated mice (n = 3/arm). *P<0.01 **c.** Autoradiography, immunofluorescence, and H&E of the right lung lobe shows higher tracer accumulation in the treated lung, as well as higher GZMB and CD3 staining. **d.** A bar graph showing the percent change in radiotracer uptake per organ between the LPS versus sham treated mice (n = 4/arm). All changes were determined to be statistically significant, P < 0.05. **e.** Representative maximum intensity projections showing the system wide changes in tracer biodistribution due to treatment with 3.0 mg/kg LPS.

1.4 Discussion

In this report, we show that granzyme biochemistry can be detected in vivo with nuclear imaging. This was achieved by a development of ⁶⁴Cu-GRIP B, a peptide-based chemosensor whose biodistribution was engineered to be controlled by the proteolytic activity of secreted GZMB. Crucial to the design of GRIP B was the discovery of a highly efficient P4–P4' substrate sequence for GZMB that gates the activation of the probe. Subsequently, in vitro and in vivo studies demonstrated that GZMB cleaves GRIP B and that changes in the tissue uptake of ⁶⁴Cu-GRIP B are driven by immune cell activation and the secretion of GZMB. Applying ⁶⁴Cu-GRIP B in vivo identified in real time multiple organs with elevated GZMB, a feature that we expect will enable a more holistic mapping of complex human immunology through quantitative imaging. Moreover, the exploratory study that applied ⁶⁴Cu-GRIP B to an inflammatory model in which the secreted GZMB has an unknown significance shows how this imaging technology may be used to begin a probing of noncytotoxic functions for this enzyme class.

These imaging data come at an exciting time, as ongoing work from other laboratories have shown that active site-directed inhibitors of GZMB can also be rendered into Ga-68 or F-18 radiopharmaceuticals designed to detect GZMB in vivo.^{22,23,35} As with ⁶⁴Cu-GRIP B, the tumoral uptake of these active site inhibitors is enhanced by a systemic CPI treatment, and the magnitude of post-treatment changes in the tumoral uptake is anticorrelated with volumetric tumor responses. The development of ⁶⁴Cu-GRIP B complements these innovations by

enabling a readout of enzyme turnover to pair with the measurement of biochemically active GZMB molecules provided by the peptide aldehydes. The unique mechanism of GRIP B may also enable an imaging at extended time points postinjection (i.e., >4 h), which could improve the signal-to-background and/or reveal occult tumors through a catalytic amplification of probe retention.

Our data suggest that ^{64}Cu -GRIP B may have a role in monitoring an early treatment response to immunotherapies. The documentation of early tumor responses to CPIs is currently a challenge clinically with standard of care ^{18}F fluorodeoxyglucose (FDG) PET and CT. In the case of PET, the immunoresponsive tumor newly perfused with metabolically active cytotoxic T cells tends to consume the same or more ^{18}F FDG than it did in its pretreatment state, which mimics the imaging findings of an unresponsive, progressing tumor.³⁶ Pseudoprogession is also observed on CT in up to 10% of all patients,³⁷ presumably due to the transient increase in cellularity within the immunoresponsive tumors. Custom algorithms (e.g., PERCIMT, iRECIST) are under development to better interpret ^{18}F FDG PET/CT post-immunotherapies, but the challenges with ^{18}F FDG PET/CT have rightly motivated a swell of new experimental radiotracers to more clearly distinguish responsive from nonresponsive tumors.^{38–41} The detection of a system-wide T-cell activation in normal tissues also implies that ^{64}Cu -GRIP B might be useful for the identification of patients at risk for developing immune-related adverse events. Direct detection of extracellular GZMB proteolysis may have advantages over biomarkers that measure immune cell markers (e.g., CD4, CD8) but do not distinguish between indolent or activated T cells.⁴² We are currently translating ^{64}Cu -GRIP B into patients to study these applications.

Lastly, these data provide an important confirmation that the RIP platform can be engineered to image functionally discrete proteases beyond thrombin. The versatility of the RIP platform to conjugate with chemically discrete payloads may also permit radiolabeling with other diagnostic (e.g., Zr-89, F-18) or therapeutic (e.g., Lu-177, Ac-225) radioisotopes. The granzyme

family has divergent, highly specific substrate specificities from which we expect the RIP technology's activity-based accumulation benefits. Moving forward, we aim to expand this platform to enable a preclinical imaging with other modalities (e.g., fluorescence tomography) and develop imaging probes to detect the other granzyme species.

1.5 Methods

General Methods

All reagents were purchased from commercial sources and used without further purification.

⁶⁴Cu-hydrochloride acid was purchased from University of Wisconsin Madison. Recombinant human GZMB was purchased from Sigma-Aldrich. The mouse cancer cell lines CT26 and EMT6 were purchased from ATCC. MC38 was purchased from Kerafast. Antimouse PD-1 (CD279) (BE0146) and antimouse CTLA-4 (CD152) (BE0164) were purchased from Bio X Cell; Anti granzyme B (ab4059) was purchased from Abcam; anti-CD3 (MCA1477) was purchased from Bio-Rad; AF488 anti-Rabbit (A21206), AF546 anti-Mouse (A111081), and AF633 anti-Mouse (A21052) secondary antibodies were purchased from Invitrogen. AF2225 anti-mouse NKp46/NCR1 was purchased from R&D system. BE0075-1 anti-mouse Ly6G was purchased from Bio X Cell. AF488 anti-RAT (A48269) and AF647 anti-goat (A21446) were purchased from Invitrogen. 4',6-Diamidino-2-phenylindole (DAPI) (D1306) was purchased from Life Technologies Corporation. Antibodies for immunofluorescence. All cell lines were cultured according to manufacturer's instructions. Active, human MMP-9 was purchased from Millipore Sigma. Human, activated Complement C 1s protease was purchased from Millipore Sigma. Thrombin from human plasma was purchased from Sigma-Aldrich. Active, human placenta cathepsin B was purchased from Sigma-Aldrich. Active, human recombinant caspase-8 was purchased from Enzo Lifesciences. Active, human recombinant caspase-3 was purchased from Enzo Lifesciences. Recombinant human granzyme A was purchased from R&D Systems. Recombinant human granzyme K was purchased from Enzo Lifesciences.

Multiplex Substrate Profiling by Mass Spectrometry

Human GZMB (100 nM) was incubated with a library containing 228 synthetic tetra-decapeptides (500 nM). Aliquots (10 μ L) were removed at three time intervals and subsequently quenched with 10 μ L of 8 M guanidinium hydrochloride. Aliquots were then flash frozen until all time points were taken. Prior to the mass spectrometry, samples were desalted using C18 tips (Rainin). Aliquots were then analyzed by LC-MS/MS sequencing using a Quadrupole Orbitrap mass spectrometer (LTQ Orbitrap XL) coupled to a 10 000 psi nanoACQUITY Ultra Performance Liquid Chromatography (UPLC) System (Waters) for a peptide separation by reverse-phase liquid chromatography (RPLC). Peptides were separated over a Thermo ES901 C18 column (75 μ m inner diameter, 50 cm length) coupled to an EASY-Spray ion source and eluted by the application of a flow rate of 300 nL/min with a 65 min linear gradient from 2–50% in Buffer B (acetonitrile, 0.5% formic acid). Survey scans were recorded over a 325–1500 m/z range and up to the three most-intense precursor ions (MS1 features of charge ≥ 2) were selected for a higher-energy collisional dissociation (HCD) at a resolution of 30 000 at m/z 200 for MS/MS[CB2]. Data were acquired using Xcalibur software and processed as previously described.^{17,43} Briefly, raw mass spectrometry data were processed to generate peak lists using MSConvert. Peak lists were then searched in Protein Prospector ver. 6.2.2 against a proprietary database containing the sequences from the 228 tetra-decapeptide library.⁴⁴ Searches used a mass accuracy tolerance of 20 ppm for precursor ions and 30 ppm for fragment ions. Variable modifications included a N-terminal pyroglutamate conversion from glutamine or glutamate and an oxidation of tryptophan, proline, and tyrosine. Searches were subsequently processed using the MSP-xtractor software (<http://www.craiklab.ucsf.edu/extractor.html>), which extracts the peptide cleavage site and spectral counts of the corresponding cleavage products. Spectral counts were used for the relative quantification of peptide cleavage products. Human GZMB samples were processed as three biological replicates per time point, and a nonenzyme control was used for each replicate to remove unspecific cleavages from the data analysis.

Fmoc-Solid-Phase Peptide Synthesis

A quenched fluorogenic peptide synthesized of the sequence NH₂-K(MCA)IEPDVSQVK(DNP)-COOH (MCA = 7-methoxycoumarin-4-acetic acid, DNP = 2-dinitrophenyl) was synthesized by an Fmoc solid-phase synthesis on a Biotage Syroll peptide synthesizer at ambient temperature. The synthesis scale was at 12.5 μM using a preloaded lysine DNP Wang resin, where the DNP quencher was linked to the epsilon nitrogen of the lysine. Coupling reactions were performed with 4.9 equiv of *O*-(1*H*-6-chlorobenzotriazole-1-yl)-1,1,3,3-tetramethyluronium hexafluorophosphate (HCTU), 5 equiv of Fmoc-amino acid-OH, and 20 equiv of *N*-methylmorpholine (NMM) in 500 μL of *N,N*-dimethylformamide (DMF) for 8 min while being shaken. Each amino acid position was double-coupled, and subsequent Fmoc deprotection was performed with 500 μL of 40% 4-methylpiperadine in DMF for 10 min followed by six washes with 500 μL of DMF for 3 min. The final amino acid coupling contained the fluorophore, lysine (MCA), where MCA was linked to the epsilon nitrogen of the lysine. Peptides were cleaved from Wang's resin with 500 μL of solution composed of 95% trifluoroacetic acid, 2.5% water, and 2.5% triisopropylsilane for 1 h while being shaken. The crude peptide product was then precipitated in 30 mL of cold 1:1 diethyl ether/hexanes and then solubilized in a 1:1:1 mixture of DMSO/water/acetonitrile. The solubilized crude was purified by high-performance liquid chromatography (HPLC) using an Agilent Pursuit 5 C18 column (5 mm bead size, 150 × 21.2 mm) on an Agilent PrepStar 218 series preparative HPLC. The mobile phases A and B were water + 0.1% trifluoroacetic acid (TFA) and acetonitrile + 0.1% TFA, respectively. The purified peptide product had the solvent removed under a reduced atmosphere and was solubilized into a DMSO stock with a final concentration of 10 mM. The purity was confirmed by liquid chromatography–mass spectrometry, and the stock was stored at –20 °C. Fluorescently labeled 5FAM-GRIP B was purchased from CPC Scientific at 95–98% purity.

Synthesis of DOTA-GRIP B

DOTA-GRIP B (Dota-hexanoic acid-FVQWFSKFLGKIEPDVSQVQDPNDQYEPF-COOH) was synthesized first by the use of standard solid-phase peptide synthesis conditions as outlined above. The resin-bound peptide with N-terminal hexanoic acid was triply coupled with 2 equiv of dota-NHS, 5 equiv of HCTU, and 20 equiv of *N,N*-diisopropylethylamine (DIPEA) for 12 h. The DOTA-GRIP B probe was then cleaved, purified, and analyzed as described for the fluorogenic peptide.

In Vitro Kinetics

Kinetic measurements were performed in Corning black 384-well flat-bottom plates and read on a BioTek H4 multimode plate reader. The proteolysis of the quenched fluorogenic peptide (NH₂-K(MCA)IEPDVSQVK(DNP)-COOH) by GZMB was performed at a final enzyme concentration of 5 nM in phosphate-buffered saline (PBS). Michaelis–Menten kinetics were performed in triplicate at 37 °C, and activity was monitored for 1 h. The *V*_o value was calculated at 1–30 min in RFU/s. Initial velocities were then converted to molar per second using a standard curve of cleaved substrate. Specificity experiments were done with all final enzyme concentrations of 5 nM and final quenched fluorogenic peptide concentration of 60 μM. The specificity assay buffer was PBS with 1 mM dithiothreitol (DTT). Kinetics were performed in quadruplicate at 37 °C, and the activity was monitored for 1 h.

Intrinsic Tryptophan Fluorescence Spectroscopy Measuring Lipid Insertion

The fluorescence of the tryptophan within the full-length and activated GRIP B was monitored in the presence or absence of lipid micelles on a BioTek H4 multimode plate reader. Sodium dodecyl sulfate (SDS) was solubilized as a 5 mg mL⁻¹ stock. Full-length and activated GZMB-RIP were solubilized in PBS to a final concentration of 0.01 mg mL⁻¹ with a final peptide/lipid molar ratio of 1:40. Tryptophan emission spectra of the peptide/lipid suspension were acquired with an excitation wavelength of 295 nm and by scanning from 310 to 450 nm. The bandwidth was 5 nm for both excitation and emission. The spectra of the peptides in PBS in the absence of SDS lipids were acquired at the same concentration of 0.01 mg mL⁻¹.

Circular Dichroism of Activated GRIP B

Spectra were acquired on a Jasco J-810 spectrometer with samples maintained at 310 K.

Spectra were recorded from 250 to 200 nm using a spectral bandwidth of 1 nm and a scan rate of 100 nm min⁻¹. The buffer was 20 mM Na₂HPO₄. Final peptide concentrations were 0.1 mg/mL, and SDS lipid concentrations were kept at a minimum of a 1:40 peptide/lipid molar ratio. Spectra were treated using Jasco spectra analysis software, where a spectrum of the peptide-free suspension was subtracted and means-movement smoothing with a convolution width of five points was applied.

Toxicity Assay Measuring Hemolysis of Human Erythrocytes

Blood from healthy anonymous donors was harvested from Trima Leukoreduction chambers (Vitalant). Erythrocytes were isolated from the anonymous blood samples. Full-length GRIP B and activated GRIP B were measured for their hemolytic activity on healthy human erythrocytes in triplicate. Aliquots of human erythrocytes were suspended in PBS (pH 7.4) and incubated with serial dilutions of both peptides, which were initially solubilized in DMSO. DMSO and 1% Triton X-100 were incubated in parallel as negative and positive controls, respectively. The incubation was for 1 h at 37 °C. After the incubation, the samples were centrifuged for 5 min at 2000g, after which the supernatant was collected. The supernatant was measured for the release of hemoglobin by the erythrocytes using a BioTek H4 multimode plate reader, monitoring the optical density of the supernatant at a wavelength of 540 nm.

Flow Cytometry with 5FAM-GRIP B

MC38 cells (2 × 10⁵/well) were seeded into a 12-well plate and incubated at 37 °C for 48 h.

5FAM-GRIP B (200 nM) and GZMB (20 nM) were dissolved in HBSS and incubated at 37 °C for 2 h. The 200 nM RIP with/without 50 nM GZMB in HBSS (300 µL) was added into the well with the cells, followed by an incubation at 37 °C for 30 min. The probe solution was removed, and cells were washed with PBS four to five times. Trypsin (100 µL) was added, followed by 3 min of incubation at 37 °C. PBS was added into the wells, and all cells were collected and washed with PBS for one time before being further diluted with PBS (300 µL) and passed through a cell

strainer. Experiments were performed on a BD FACSCanto II Cell Analyzer. Data were analyzed by the use of FlowJo and Prism 8.0.

Radiosynthesis and In Vitro Characterization of ^{64}Cu -GRIP B

Into a 1.5 mL reaction vial was added 5 mCi of ^{64}Cu -chloride (aqueous), and the pH was adjusted to 7.0 with Na_2CO_3 (2 M). A solution of DOTA-GRIP B (50 μg in 20 μL of DMSO) and 0.1 M NH_4OAC buffer (200 μL) was added into this reaction vial. The reaction mixture was incubated at 50 °C for 30 min. The reaction progress was monitored by analytical HPLC equipped with an Agilent Pursuit analytical column (C18, 200 Å, 4.6 mm \times 10 cm, 5 μm) or Phenomenex Luna analytical column (C18, 100 Å, 4.6 mm \times 250 cm, 10 μm) (70:30 MeOH/H₂O to 95:5 MeOH/H₂O over 10 min). The crude reaction was purified using a C18 Sep-Pak cartridge and eluted with a small volume of CH₃CN. The CH₃CN was then removed at 50 °C under vacuum and a gentle stream of N₂(g) to afford neat ^{64}Cu -GRIP B. The chelation efficacy is usually greater than 90% based on the HPLC. A formulation comprising 10% DMSO, 10% tween 80, and 80% saline was adopted for further mice studies. The cleavage of ^{64}Cu -GRIP B by granzyme B was verified in vitro by an addition of the radiotracer (~200 μCi) to the recombinant granzyme B (10 nM) in 500 μL of PBS. The vial was then incubated at 37 °C. Rad-HPLC was used to monitor the cleavage of the radiotracer at the dedicated time points.

Animal Studies

All animal experiments were approved by the Institutional Animal Care and Use Committee at UCSF. Four to six week old male or female balb/c mice and C57BL6/J mice were purchased from Jackson Laboratory and housed with free access to the water and food. All mice were inoculated with 5×10^6 CT26, MC38, or EMT6 cells in a mixture of media and Matrigel (Corning) (v/v 1:1) subcutaneously into the left shoulder. Antimouse PD-1 (CD279) (BE0146) and antimouse CTLA-4 (CD152) (BE0164) were purchased from Bio X Cell and stored at 4 °C during the treatment studies. Mice bearing subcutaneous tumors received antimouse CTLA-4 (200 μg) or/and antimouse PD-1 (200 μg) and as a combination therapy or PBS as the vehicle

on days 5, 8, and 11 following the tumor inoculation. Mice were weighed, and the tumor volume was measured with calipers on the same day of the treatment. On day 14, all mice were used for PET/CT or BioD studies.

GZMB Homozygous Knockout Mice

Germline homozygous GZMB knockout cluster mice were created with a homozygous null mutation in the GZMB gene. GZMB knockout cluster mice were generously donated by Dr. T. Ley.²⁹

Small Animal PET/CT

⁶⁴Cu-L-GRIP B or ⁶⁴Cu-D-GRIP B (~100 µCi/mouse) in 100–150 µL of 10% DMSO and 10% Tween 80 in saline was injected via tail vein. After a period of uptake time, mice were anesthetized with isoflurane (~2%) and imaged with a microPET/CT scanner (Inveon, Siemens). For a static imaging, mice were scanned for 30 min for a PET data acquisition and 10 min for a CT data acquisition. For the dynamic acquisitions, the mice were anesthetized, positioned on the scanner bed, and injected intravenously with a radiotracer. The dynamic acquisition was performed for 60 min followed by a 10 min CT acquisition.

List-mode PET data were histogrammed to generate sinograms that were reconstructed using a 2D ordered subsets expectation maximization algorithm provided by the scanner manufacturer. An attenuation correction was applied using the coregistered CT data that were acquired immediately following the PET data acquisition. The CT data were acquired using the following setting: 220° angular coverage with 120 steps, X-ray tube operating at 80 kVp and 0.5 mA with each angular step exposure time set as 175 ms. All reconstructed three-dimensional (3D) PET volume image voxels were calibrated to becquerel per milliliter using a precalibrated quantification factor. AMIDE software was used for the reconstruction of PET/CT data and an image analysis.

Biodistribution Studies

At dedicated time points post-radiotracer injection, mice were euthanized with CO₂(g) asphyxiation, and the blood was collected by a direct cardiac puncture. Tissues were harvested,

weighed, and counted on a γ -counter (Hidex). The amount of radioactivity in the tissues was determined by comparison with a standard of known activity. The samples were decay-corrected and expressed as the percentage of the injected dose/weight of the harvested tissues (%ID/g).

Digital Autoradiography

Tumors or designated tissue were flash frozen in an optimal cutting temperature (OCT) in dry ice. The tissues were sectioned with a microtome (Leica) into slices with 10–20 μ m thickness and directly mounted on glass slides (VWR). A GE Storage Phosphor Screen was exposed by such slides with radioactive tissue. After 10 half-lives of copper-64, the screen was developed on a phosphorimager (Typhoon 9400). The images were further analyzed by using Fiji software.

Histology

Hematoxylin and eosin (H&E) staining and immunofluorescence staining were performed by the Pathology core facility at UCSF and Acepix Biosciences. For IF studies, tumor samples were soaked in acetone at $-20\text{ }^{\circ}\text{C}$ for 20 min, followed by a soak in MeOH at $4\text{ }^{\circ}\text{C}$ for 10 min. Antigen retrieval was conducted with citrate buffer 10 mM pH = 6, and samples were blocked with a universal blocking buffer plus 5% goat and donkey serum. The primary antibodies, namely, anti-GZMB (ab4059, Abcam) (1:50), anti NKp46/NCR1(1:1000, R&D system), anti Ly6G (1:5000, Bio X Cell), and anti-CD3 (MCA1477, Bio-Rad) (1:100), were added into samples and incubated at $4\text{ }^{\circ}\text{C}$ overnight. Such primary antibodies were detected by AF488 anti-Rabbit (A21206, Invitrogen) (1:200), AF546 anti-Mouse (A111081, Invitrogen) (1:200), AF488 anti-Rat (A48269, Invitrogen) (1:500), AF647 anti-goat (A21446, Invitrogen) (1:500), and AF633 anti-Mouse (A21052, Invitrogen) (1:200) secondary antibodies by an incubation with samples. DAPI Nucleic Acid Stain (D1306, Life Technologies Corporation) was used to stain the nucleus by being incubating with samples (10 min at room temperature). Immunofluorescence results were performed by the Gladstone Institutes' Histology & Light Microscopy Core. Images of whole sections were acquired on a VERSA automated slide scanner (Leica Biosystems), equipped

with an Andor Zyla 5.5 sCMOS camera (Andor Technologies). Individual images were created with the ImageScope software (Aperio Technologies).

Statistics

All statistical analyses were performed by using PRISM v8.0 or ORIGIN software. A statistically significant difference was determined by an unpaired, two-tailed Student's *t* test. Changes only at the 95% confidence level ($P < 0.05$) were regarded as statistically significant.

1.6 Supplementary Materials

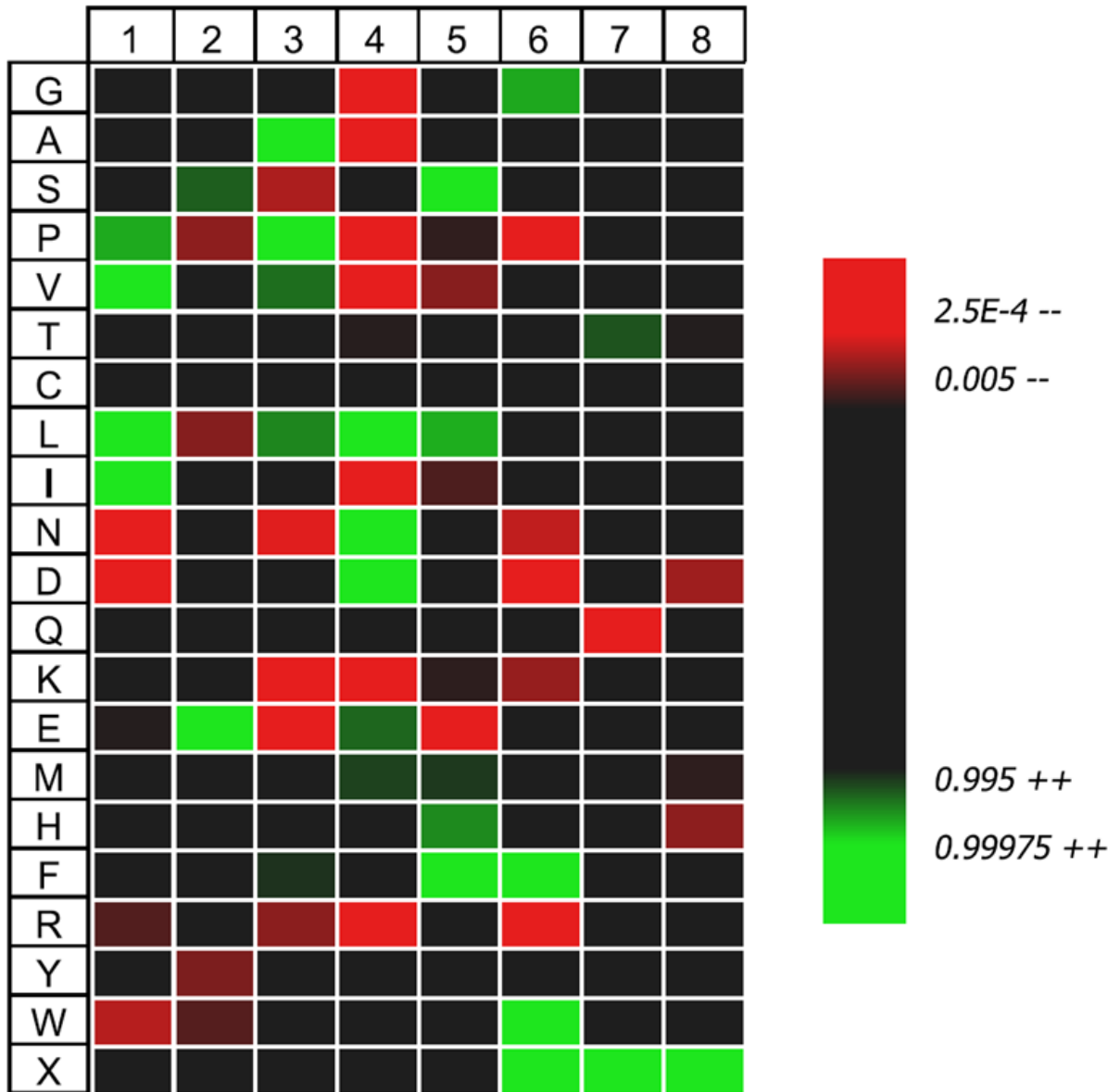


Figure 1.S1: A heat map showing the preferred cleavage sites for recombinant human granzyme B as predicted with multiplex substrate profiling mass spectrometry where 1-8 represents P4-P4', respectively.

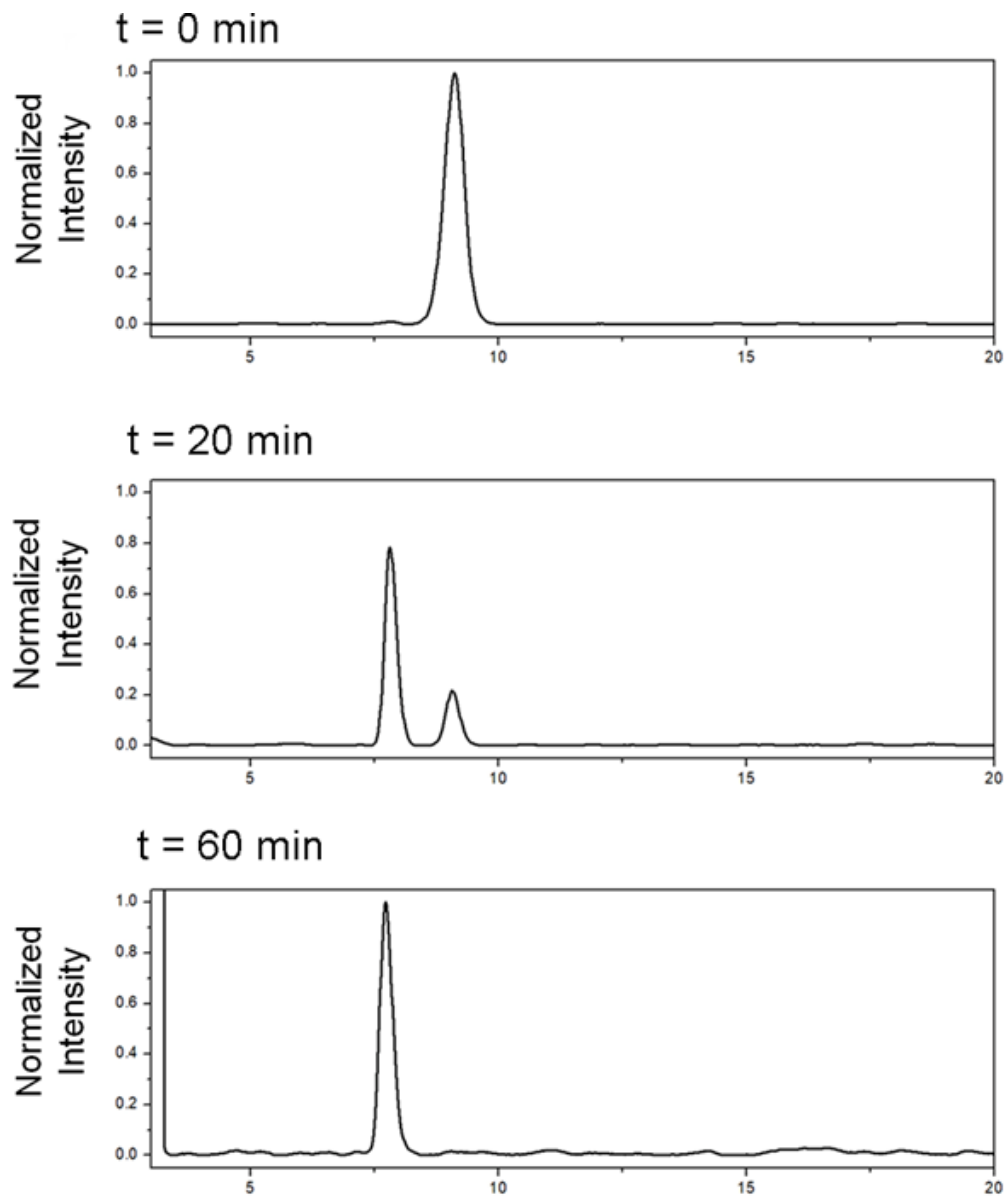


Figure 1.S2: Stacked HPLC traces showing the cleavage of GRIP B by recombinant human GZMB. The single product peak at ~7.7 minutes comigrates with the peptide standard FVQWFSKFLGKIEPD. The data are reflective of three independent experiments.

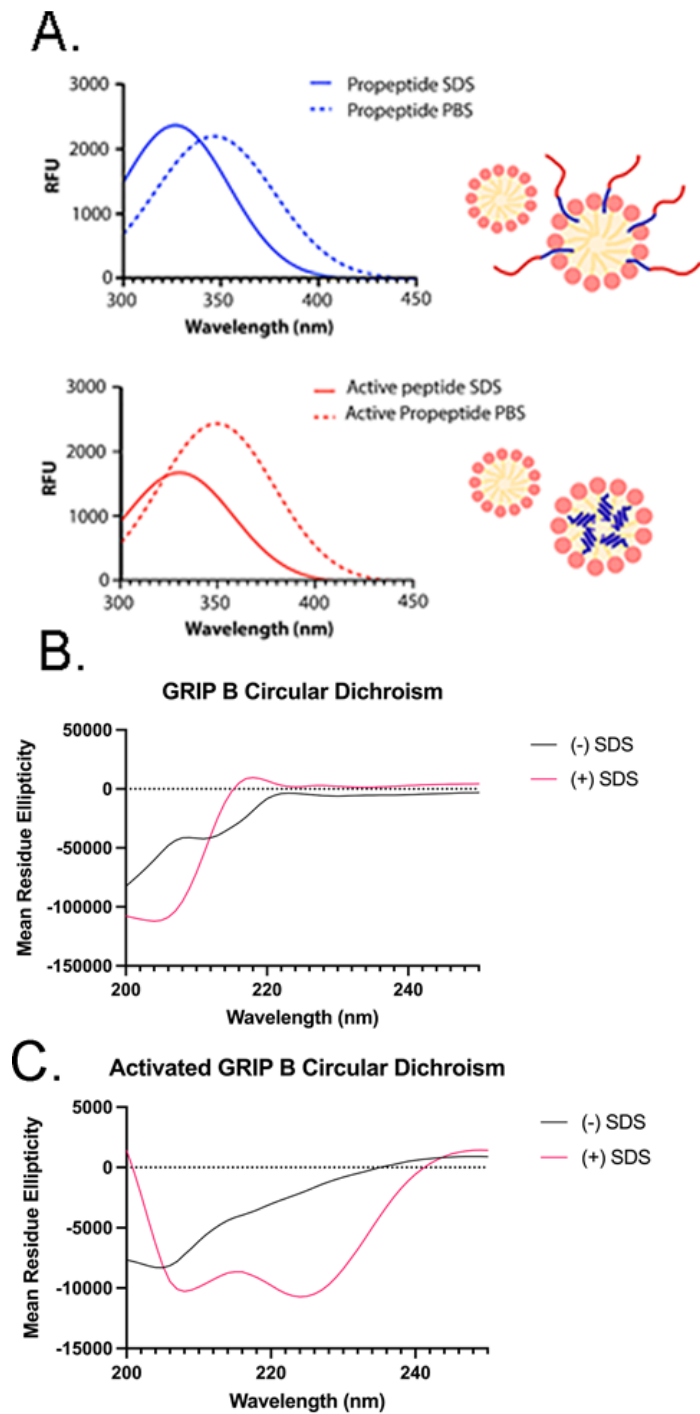


Figure 1.S3: Tryptophan insertion experiments and circular dichroism.

A. Probing membrane interaction dynamics with SDS-micelles through tryptophan intrinsic fluorescence reveals partial interaction of the full-length propeptide, and complete internalization of the activated GRIP B. **B.** Circular dichroism of full-length GRIP B shows a spectrum indicative of a disordered peptide, suggesting that the masking domain is effective in disrupting the alpha helical secondary structure of the cell penetrating peptide module. **C.** Circular dichroism of activated GRIP B reveals the characteristic spectra of alpha helical peptides, showing that the probe retains the secondary structure of Tempurin L.

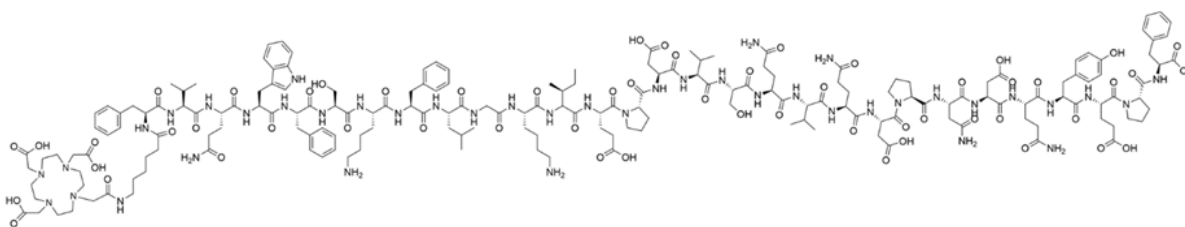


Figure 1.S4: The structure of DOTA-GRIP B. The 2-D chemical structure of the synthetic GRIP B probe.

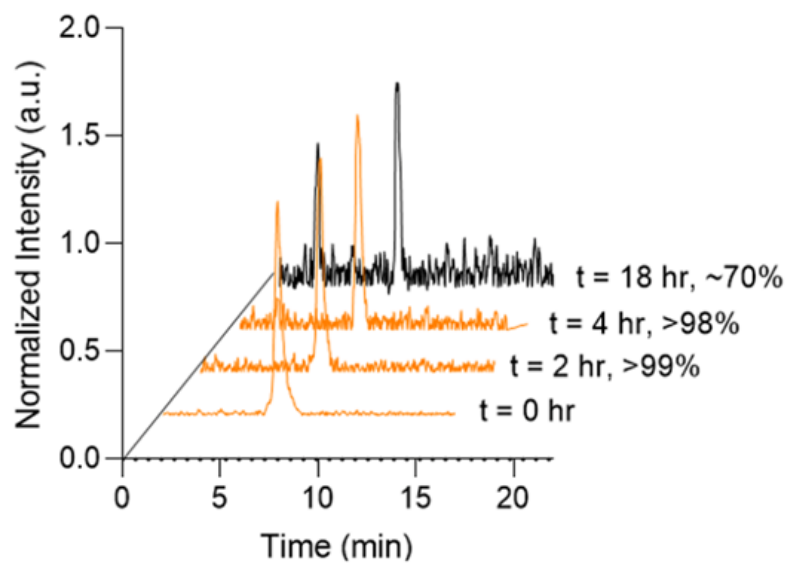


Figure 1.S5. A plot showing the stability of ^{64}Cu -GRIP B in mouse serum. The probe was incubated at 37°C , and the radioactive species were separated and quantified on RAD-HPLC.

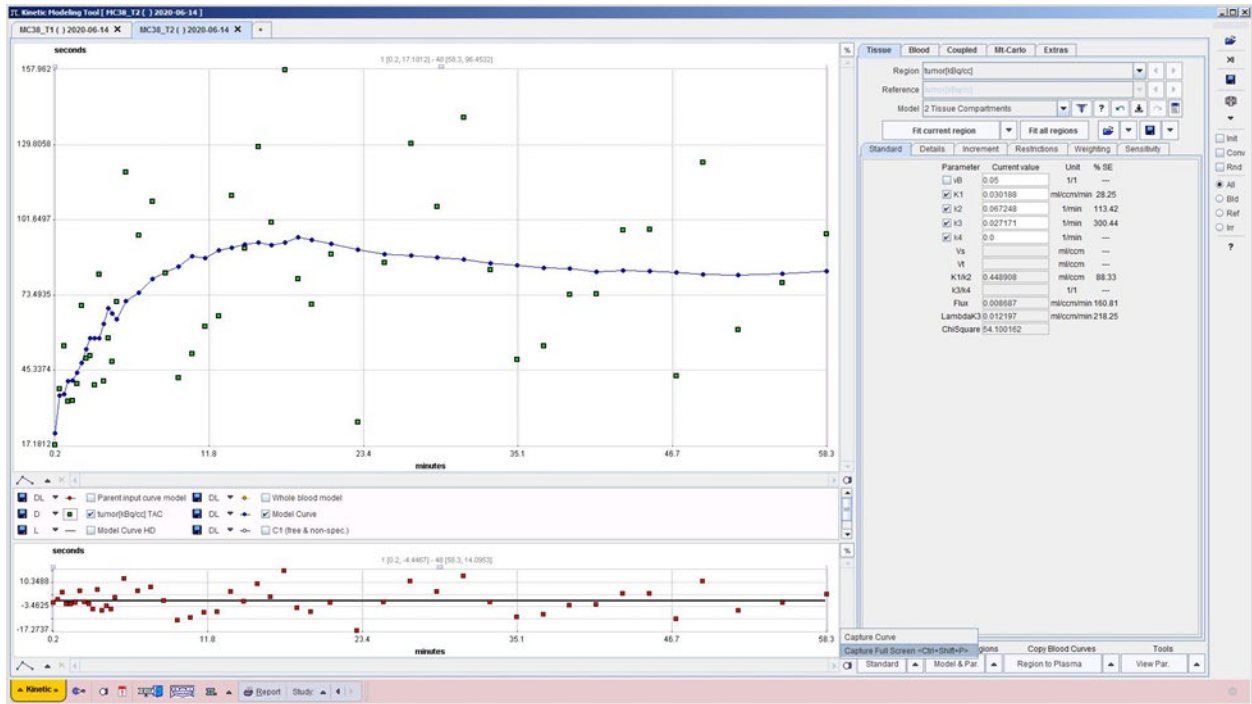


Figure 1.S6. An example of a compartmental analysis of tumoral uptake of ^{64}Cu -GRIP B. The analysis was performed using a 1 hour dynamic PET acquisition from a Balb/c mouse bearing a MC38 tumor with was treated with CPI. The analysis show $k_3 > k_4$ and $k_4 \sim 0$. These data are representative of similar outcomes for C57Bl6 mice bearing CT26 tumors.

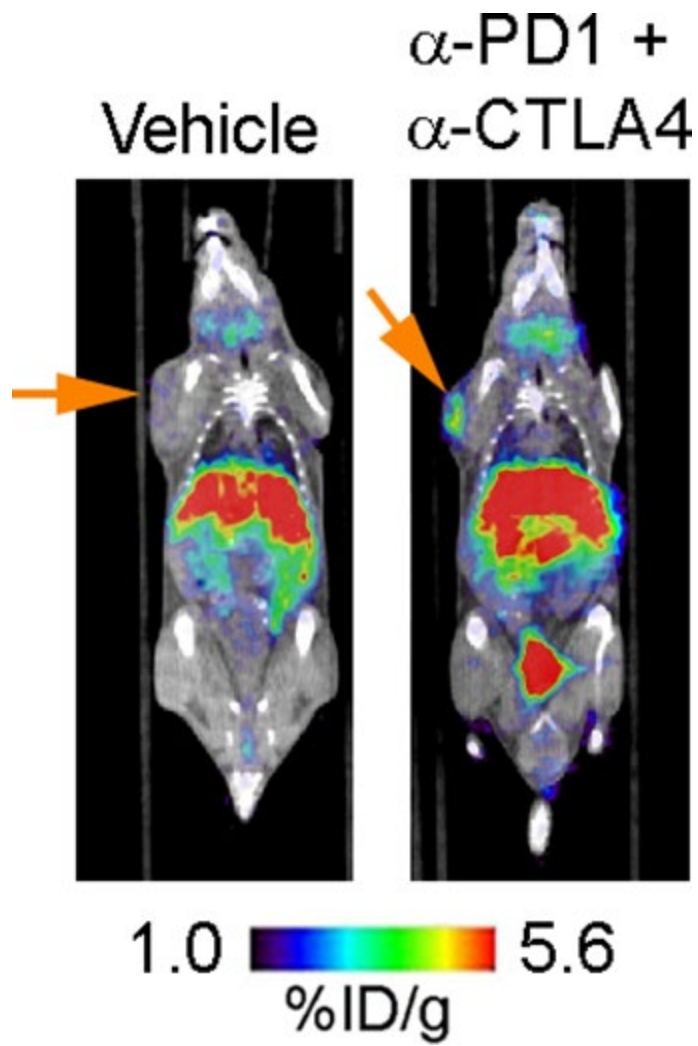


Figure 1.S7: Representative coronal ^{64}Cu -GRIP B PET/CT images of mice bearing CT26 tumors and treated with vehicle or checkpoint inhibitors. The position of the CT26 tumor is indicated with an orange arrow.

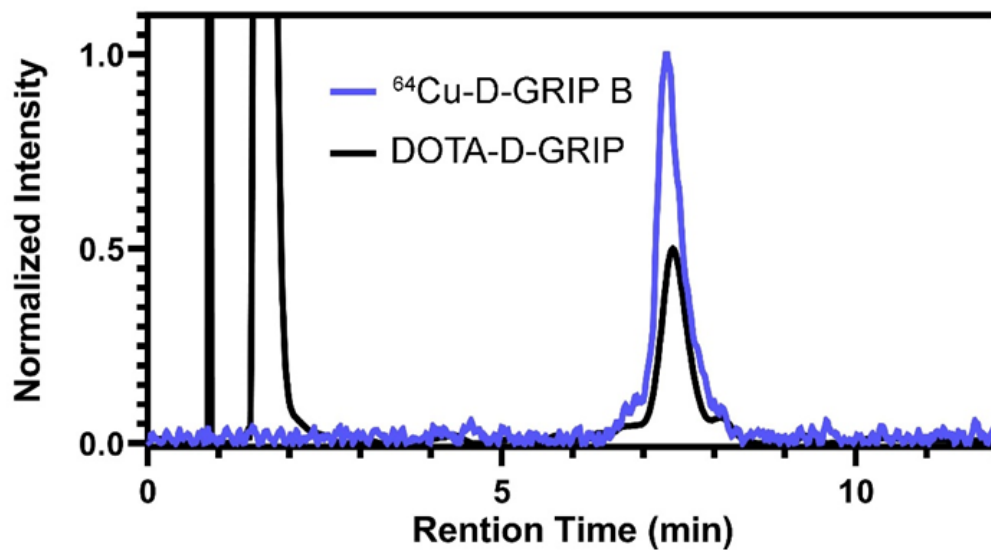


Figure 1.S8: Analytical HPLC data showing the synthesis of $^{64}\text{Cu-D-GRIP B}$. The blue trace shows the RAD peak from the complex reaction mixture. The black peak shows the UV of the DOTA-D-GRIP B starting material.

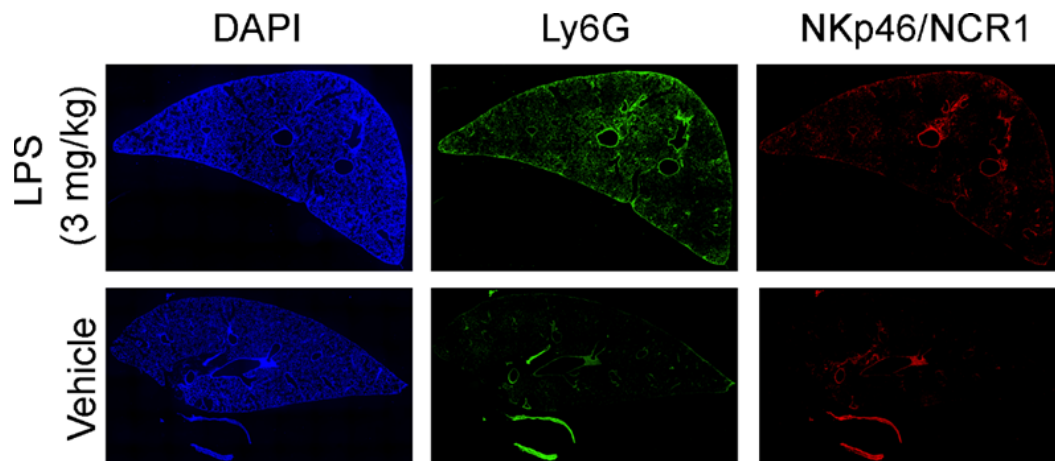


Figure 1.S9: Immunofluorescence data showing increased staining for the neutrophil marker Ly6G in LPS versus vehicle treated lung tissue. No obvious difference was observed between arms in the intensity of the natural killer cell marker NKp46/NCR1. The stained slides were adjacent to the slices shown in Figure 6.

Table 1.S1: A tabular representation of the biodistribution data collected at various time points post injection of ⁶⁴Cu-GRIP B in tumor naïve male C57BL/6 mice. The data represent the mean ± standard deviation, n = 4 per time point.

Tissue	Time post injection (hr)				
	0.5	1	2	4	24
Blood	4.58 ± 0.3	3.07 ± 1.3	1.55 ± 0.1	1.61 ± 0.2	1.15 ± 0.06
Brain	0.33 ± 0.06	0.31 ± 0.02	0.32 ± 0.02	0.39 ± 0.03	0.43 ± 0.02
Heart	3.07 ± 0.3	2.49 ± 0.4	2.22 ± 0.2	2.62 ± 0.2	2.73 ± 0.3
Liver	16.94 ± 1.1	20.38 ± 2.2	24.98 ± 2.7	22.78 ± 1.3	21.56 ± 1.6
Kidneys	148.36 ± 7.9	90.35 ± 7.2	54.39 ± 9.5	54.16 ± 12.6	14.58 ± 3.3
Spleen	2.72 ± 0.3	2.92 ± 0.6	2.22 ± 0.3	2.42 ± 0.8	2.07 ± 0.09
Pancreas	1.67 ± 0.1	1.84 ± 0.8	1.77 ± 0.6	1.49 ± 0.2	1.54 ± 0.08
Stomach	2.83 ± 0.9	3.24 ± 0.7	4.28 ± 0.4	3.72 ± 1.5	3.27 ± 0.2
Small Intestine	8.4 ± 0.07	11.08 ± 1.9	8.14 ± 0.8	9.98 ± 1.7	6.15 ± 0.8
Large Intestine	4.64 ± 0.2	5.64 ± 0.8	10.69 ± 3.1	13.78 ± 1.3	6.8 ± 0.9
Skeletal Muscle	1.19 ± 0.1	1.17 ± 0.3	0.75 ± 0.1	0.66 ± 0.07	0.67 ± 0.06
Bone	1.86 ± 0.4	1.45 ± 0.3	1.21 ± 0.01	1.46 ± 0.3	1.29 ± 0.1
Lung	5.81 ± 0.8	5.81 ± 0.7	6.88 ± 0.2	7.43 ± 0.7	6.72 ± 0.6
Thymus	2.49 ± 0.3	2.43 ± 0.2	2.2 ± 0.1	2.48 ± 0.5	2.67 ± 0.4
Brown Fat	3.34 ± 0.4	2.2 ± 0.2	2.93 ± 0.5	3.25 ± 0.8	3.15 ± 0.7
White Fat	0.97 ± 0.5	0.46 ± 0.09	0.47 ± 0.1	0.3 ± 0.04	0.33 ± 0.1

Table 1.S2: A summary of the SUVmean values acquired from region of interest analysis of dynamic PET acquisitions. The data are reported as SUVmean \pm standard deviation.

Time (sec)	Control		CPI	
	SUV _{mean}	SD	SUV _{mean}	SD
10	0.03	0.3	0.11	0.3
30	0.29	0.7	0.67	1.3
50	0.49	1.2	0.24	0.6
70	0.67	1.6	2.27	2.4
110	1.04	2.1	2.77	3.7
130	0.49	0.8	2.46	3.0
150	0.55	1.0	2.28	3.3
170	1.19	1.9	2.32	3.9
210	1.02	1.9	2.58	3.0
270	0.81	1.5	3.29	4.4
330	0.88	1.1	2.56	1.8
390	0.75	1.1	3.20	3.1
450	0.60	1.0	2.95	2.4
510	0.74	1.4	4.11	4.7
570	0.86	1.3	3.70	3.3
630	0.75	0.9	4.73	3.3
690	1.14	1.8	3.88	2.8
750	1.06	1.5	3.21	2.5
810	0.72	1.1	3.55	2.7
870	0.66	0.8	3.87	2.6
990	1.06	1.5	4.01	2.5
1050	0.86	0.9	3.46	3.7
1110	0.70	1.1	4.42	2.8
1170	1.17	1.6	3.82	2.8
1260	1.04	1.3	4.86	2.3
1380	0.59	0.7	3.89	2.3
1500	1.10	1.0	4.65	2.3
1620	0.72	0.7	4.57	2.4
1740	1.25	1.1	3.69	1.9
1860	0.84	0.8	4.51	2.4
1980	1.31	1.2	4.27	1.9
2220	1.20	1.1	4.98	2.2
2340	1.11	0.9	5.34	2.8
2580	1.11	1.1	4.91	3.2
2700	0.98	1.2	4.66	2.5
2820	1.21	1.1	4.63	2.3
3100	1.46	1.3	4.76	1.7
3500	1.33	1.0	4.34	1.6

Table 1.S3: A tabular representation of the biodistribution data collected 2h post injection of radiotracer ⁶⁴Cu-L-GRIP B in male balb/c mice bearing CT26 tumor after receiving 3 antibody/PBS treatment. The P value indicates the result of an unpaired, two-tailed Student's t test between the two different arms (n = 8/group).

Tissue	Vehicle	CPI
Blood	0.55 ± 0.05	0.56 ± 0.02
Brain	0.12 ± 0.02	0.12 ± 0.01
Heart	1.53 ± 0.8	1.32 ± 0.4
Liver	8.54 ± 0.8	8.15 ± 1.4
Kidneys	34.51 ± 4.9	33.83 ± 7.1
Spleen	0.89 ± 0.3	1.62 ± 1.1
Pancreas	1.44 ± 1.3	1.07 ± 0.4
Stomach	1.68 ± 0.9	1.66 ± 0.6
Small Intestine	3.96 ± 0.6	4.28 ± 1.3
Large Intestine	4.48 ± 1.4	3.8 ± 1.1
Muscle	0.39 ± 0.1	0.35 ± 0.1
Bone	0.53 ± 0.1	0.54 ± 0.1
Lung	3.53 ± 1.5	3.76 ± 2.2
Tumor	1.73 ± 0.4	2.43 ± 0.5

Table 1.S4: Biodistribution data collected 2 hours post injection of ⁶⁴Cu-D-GRIP B in male C57Bl6 mice bearing MC38 tumors. The data are expressed as mean %ID/g ± standard deviation, n = 8 per treatment arm.

Tissue	Vehicle	Treatment
Blood	1.10 ± 0.2	1.0 ± 0.2
Brain	0.19 ± 0.05	0.21 ± 0.09
Heart	1.38 ± 0.1	1.2 ± 0.08
Liver	13.18 ± 3.2	10.24 ± 3.5
Kidneys	34.28 ± 7.1	28.19 ± 2.2
Spleen	1.25 ± 0.2	1.24 ± 0.3
Pancreas	1.12 ± 0.8	0.91 ± 0.2
Stomach	2.36 ± 0.2	2.95 ± 0.8
Small Intestine	6.28 ± 2.1	6.57 ± 2.55
Large Intestine	4.54 ± 1.9	6.17 ± 2.5
Muscle	0.36 ± 0.1	0.42 ± 0.2
Bone	0.70 ± 0.1	0.82 ± 0.1
Lung	4.0 ± 0.5	3.84 ± 0.5
Tumor	2.29 ± 0.3	3.74 ± 1.2

Table 1.S5: Biodistribution data collected 2 hours post injection of ⁶⁴Cu-D-GRIP B in male C57Bl6 mice bearing MC38 tumors. The data are expressed as mean %ID/g ± standard deviation, n = 5 per treatment arm.

Tissue	Vehicle	CPI
Blood	1.21 ± 0.09	0.39 ± 0.03
Muscle	0.31 ± 0.06	0.21 ± 0.03
Spleen	1.06 ± 0.1	0.43 ± 0.02
Kidneys	34.10 ± 3.7	16.44 ± 2.5
Tumor	2.09 ± 0.2	2.22 ± 0.5

Table 1.S6: Biodistribution data collected 2 hours post injection of ⁶⁴Cu-GRIP B in female Balb6 mice bearing EMT6 tumors. The data are expressed as mean %ID/g ± standard deviation, n = 5 per treatment arm.

Tissue	Vehicle	CPI
Blood	0.55 ± 0.05	0.56 ± 0.02
Brain	0.12 ± 0.02	0.12 ± 0.01
Heart	1.53 ± 0.8	1.32 ± 0.44
Liver	8.54 ± 0.8	8.15 ± 1.42
Kidneys	34.51 ± 4.9	33.83 ± 7.16
Spleen	0.89 ± 0.34	1.62 ± 1.12
Pancreas	1.44 ± 1.39	1.07 ± 0.45
Stomach	1.68 ± 0.97	1.66 ± 0.65
Small Intestine	3.96 ± 0.63	4.28 ± 1.32
Large Intestine	4.48 ± 1.43	3.8 ± 1.11
Muscle	0.39 ± 0.19	0.35 ± 0.1
Bone	0.53 ± 0.17	0.54 ± 0.13
Lung	3.53 ± 1.54	3.76 ± 2.27
Tumor	1.83 ± 0.47	2.4 ± 0.59

Table 1.S7: Biodistribution data collected 2 hours post injection of ⁶⁴Cu-D-GRIP B in female Balb6 mice bearing EMT6 tumors. The data are expressed as mean %ID/g ± standard deviation, n = 5 per treatment arm.

Tissue	Vehicle	CPI
Blood	2.11 ± 0.12	1.29 ± 0.34
Muscle	0.36 ± 0.05	0.32 ± 0.04
Spleen	2.38 ± 0.19	1.83 ± 0.26
Kidneys	33.48 ± 3	41.7 ± 5.17
Tumor	1.55 ± 0.1	1.35 ± 0.21

Table 1.S8: Biodistribution data collected 2 hours post injection of ⁶⁴Cu-GRIP B in male or female *GZMB*^{-/-} mice bearing CT26 tumors. The data are expressed as mean %ID/g ± standard deviation, n = 6 per treatment arm.

Tissue	Vehicle	CPI
Blood	0.84 ± 0.1	0.92 ± 0.1
Brain	0.10 ± 0.01	0.10 ± 0.04
Heart	0.97 ± 0.1	0.81 ± 0.4
Liver	8.12 ± 1.2	8.35 ± 1.6
Kidneys	30.50 ± 7.5	30.26 ± 4.5
Stomach	2.06 ± 1.0	2.02 ± 0.3
Small Intestine	4.91 ± 0.8	5.47 ± 1.1
Large Intestine	3.78 ± 1.6	2.61 ± 0.5
Skeletal Muscle	0.24 ± 0.05	0.36 ± 0.1
Bone	0.48 ± 0.09	0.49 ± 0.05
Pancreas	0.73 ± 0.5	0.76 ± 0.1
Spleen	0.68 ± 0.1	0.64 ± 0.1
Lung	2.62 ± 0.4	2.86 ± 0.4
Tumor	1.66 ± 0.3	1.74 ± 0.3

Table 1.S9: A summary of the biodistribution data acquired in C57Bl6 mice subjected to an intratracheal instillation of lipopolysaccharide at 0.1 or 3 mg/kg. The data are expressed as mean %ID/g ± standard deviation, n = 5 per treatment arm.

Tissue	Vehicle	LPS (0.1 mg/kg)	LPS (3 mg/kg)
Blood	0.73 ± 0.01	0.71 ± 0.07	1.19 ± 0.2
Brain	0.11 ± 0.02	0.11 ± 0.01	0.21 ± 0.02
Heart	1.09 ± 0.1	1.29 ± 0.3	1.66 ± 0.2
Liver	9.81 ± 0.5	8.65 ± 0.7	15.3 ± 1.0
Kidneys	20.58 ± 2.9	20.32 ± 4.2	35.26 ± 2.7
Spleen	0.77 ± 0.3	0.76 ± 0.1	1.38 ± 0.2
Pancreas	1.13 ± 0.09	1.13 ± 0.07	1.5 ± 0.1
Stomach	2.98 ± 0.7	2.39 ± 0.5	2.53 ± 0.2
Small Intestine	4.49 ± 0.5	4.37 ± 0.6	6.52 ± 0.3
Large Intestine	4.13 ± 2.7	2.81 ± 0.2	4.45 ± 1.1
Muscle	0.39 ± 0.1	0.26 ± 0.02	0.36 ± 0.04
Bone	0.73 ± 0.1	0.50 ± 0.1	0.71 ± 0.07
Lung	3.64 ± 0.2	3.41 ± 0.3	4.14 ± 0.09
Thymus	1.18 ± 0.07	1.22 ± 0.2	4.18 ± 0.6

1.7 References

- (1) Voskoboinik, I.; Whisstock, J. C.; Trapani, J. A. Perforin and Granzymes: Function, Dysfunction and Human Pathology. *Nature Reviews Immunology* **2015**, *15* (6), 388–400. <https://doi.org/10.1038/nri3839>.
- (2) Ritter, A. T.; Angus, K. L.; Griffiths, G. M. The Role of the Cytoskeleton at the Immunological Synapse. *Immunological Reviews* **2013**, *256* (1), 107–117. <https://doi.org/10.1111/imr.12117>.
- (3) Yannelli, J. R.; Sullivan, J. A.; Mandell, G. L.; Engelhard, V. H. Reorientation and Fusion of Cytotoxic T Lymphocyte Granules after Interaction with Target Cells as Determined by High Resolution Cinemicrography. *J. Immunol.* **1986**, *136* (2), 377.
- (4) Bykovskaja, S. N.; Rytenko, A. N.; Rauschenbach, M. O.; Bykovsky, A. F. Ultrastructural Alteration of Cytolytic T Lymphocytes Following Their Interaction with Target Cells: II. Morphogenesis of Secretory Granules and Intracellular Vacuoles. *Cellular Immunology* **1978**, *40* (1), 175–185. [https://doi.org/10.1016/0008-8749\(78\)90325-8](https://doi.org/10.1016/0008-8749(78)90325-8).
- (5) Shi, L.; Kam, C. M.; Powers, J. C.; Aebersold, R.; Greenberg, A. H. Purification of Three Cytotoxic Lymphocyte Granule Serine Proteases That Induce Apoptosis through Distinct Substrate and Target Cell Interactions. *Journal of Experimental Medicine* **1992**, *176* (6), 1521–1529. <https://doi.org/10.1084/jem.176.6.1521>.
- (6) Nakajima, H.; Henkart, P. A. Cytotoxic Lymphocyte Granzymes Trigger a Target Cell Internal Disintegration Pathway Leading to Cytolysis and DNA Breakdown. *J. Immunol.* **1994**, *152* (3), 1057.
- (7) Henkart, P. A. Lymphocyte-Mediated Cytotoxicity: Two Pathways and Multiple Effector Molecules. *Immunity* **1994**, *1* (5), 343–346. [https://doi.org/10.1016/1074-7613\(94\)90063-9](https://doi.org/10.1016/1074-7613(94)90063-9).
- (8) Sutton, V. R.; Trapani, J. A. Proteases in Lymphocyte Killer Function: Redundancy, Polymorphism and Questions Remaining. **2010**, *391* (8), 873–879.

- <https://doi.org/10.1515/bc.2010.088>.
- (9) Grossman, W. J.; Revell, P. A.; Lu, Z. H.; Johnson, H.; Bredemeyer, A. J.; Ley, T. J. The Orphan Granzymes of Humans and Mice. *Current Opinion in Immunology* **2003**, *15* (5), 544–552. [https://doi.org/10.1016/S0952-7915\(03\)00099-2](https://doi.org/10.1016/S0952-7915(03)00099-2).
- (10) van Daalen, K. R.; Reijneveld, J. F.; Bovenschen, N. Modulation of Inflammation by Extracellular Granzyme A. *Frontiers in Immunology* **2020**, *11*.
- (11) Darrah, E.; Rosen, A. Granzyme B Cleavage of Autoantigens in Autoimmunity. *Cell Death & Differentiation* **2010**, *17* (4), 624–632. <https://doi.org/10.1038/cdd.2009.197>.
- (12) Granville, D. J. Granzymes in Disease: Bench to Bedside. *Cell Death & Differentiation* **2010**, *17* (4), 565–566. <https://doi.org/10.1038/cdd.2009.218>.
- (13) Kaiserman, D.; Bird, C. H.; Sun, J.; Matthews, A.; Ung, K.; Whisstock, J. C.; Thompson, P. E.; Trapani, J. A.; Bird, P. I. The Major Human and Mouse Granzymes Are Structurally and Functionally Divergent. *Journal of Cell Biology* **2006**, *175* (4), 619–630. <https://doi.org/10.1083/jcb.200606073>.
- (14) Yang, Y.; Hong, H.; Zhang, Y.; Cai, W. Molecular Imaging of Proteases in Cancer. *Cancer Growth & Metastasis* **2009**, *2*, CGM.S2814. <https://doi.org/10.4137/CGM.S2814>.
- (15) Nguyen Anh; Ramesh Anujan; Kumar Sahana; Nandi Dipika; Brouillard Anthony; Wells Alexandria; Pobezinsky Leonid; Osborne Barbara; Kulkarni Ashish A. Granzyme B Nanoreporter for Early Monitoring of Tumor Response to Immunotherapy. *Science Advances* **6** (40), eabc2777. <https://doi.org/10.1126/sciadv.abc2777>.
- (16) Page, M. J.; Lourenço, A. L.; David, T.; LeBeau, A. M.; Cattaruzza, F.; Castro, H. C.; VanBrocklin, H. F.; Coughlin, S. R.; Craik, C. S. Non-Invasive Imaging and Cellular Tracking of Pulmonary Emboli by near-Infrared Fluorescence and Positron-Emission Tomography. *Nature Communications* **2015**, *6* (1), 8448. <https://doi.org/10.1038/ncomms9448>.

- (17) O'Donoghue, A. J.; Eroy-Reveles, A. A.; Knudsen, G. M.; Ingram, J.; Zhou, M.; Statnekov, J. B.; Greninger, A. L.; Hostetter, D. R.; Qu, G.; Maltby, D. A.; Anderson, M. O.; DeRisi, J. L.; McKerrow, J. H.; Burlingame, A. L.; Craik, C. S. Global Identification of Peptidase Specificity by Multiplex Substrate Profiling. *Nature Methods* **2012**, *9* (11), 1095–1100. <https://doi.org/10.1038/nmeth.2182>.
- (18) Lapek, J. D., Jr.; Jiang, Z.; Wozniak, J. M.; Arutyunova, E.; Wang, S. C.; Lemieux, M. J.; Gonzalez, D. J.; O'Donoghue, A. J. Quantitative Multiplex Substrate Profiling of Peptidases by Mass Spectrometry *. *Molecular & Cellular Proteomics* **2019**, *18* (5), 968–981. <https://doi.org/10.1074/mcp.TIR118.001099>.
- (19) Ivry, S. L.; Meyer, N. O.; Winter, M. B.; Bohn, M. F.; Knudsen, G. M.; O'Donoghue, A. J.; Craik, C. S. Global Substrate Specificity Profiling of Post-Translational Modifying Enzymes. *Protein Science* **2018**, *27* (3), 584–594. <https://doi.org/10.1002/pro.3352>.
- (20) Mahrus, S.; Craik, C. S. Selective Chemical Functional Probes of Granzymes A and B Reveal Granzyme B Is a Major Effector of Natural Killer Cell-Mediated Lysis of Target Cells. *Chemistry & Biology* **2005**, *12* (5), 567–577. <https://doi.org/10.1016/j.chembiol.2005.03.006>.
- (21) Ruggles, S. W.; Fletterick, R. J.; Craik, C. S. Characterization of Structural Determinants of Granzyme B Reveals Potent Mediators of Extended Substrate Specificity *. *Journal of Biological Chemistry* **2004**, *279* (29), 30751–30759. <https://doi.org/10.1074/jbc.M400949200>.
- (22) Larimer, B. M.; Wehrenberg-Klee, E.; Dubois, F.; Mehta, A.; Kalomeris, T.; Flaherty, K.; Boland, G.; Mahmood, U. Granzyme B PET Imaging as a Predictive Biomarker of Immunotherapy Response. *Cancer Research* **2017**, *77* (9), 2318–2327. <https://doi.org/10.1158/0008-5472.CAN-16-3346>.
- (23) Larimer, B. M.; Bloch, E.; Nesti, S.; Austin, E. E.; Wehrenberg-Klee, E.; Boland, G.; Mahmood, U. The Effectiveness of Checkpoint Inhibitor Combinations and

- Administration Timing Can Be Measured by Granzyme B PET Imaging. *Clinical Cancer Research* **2019**, *25* (4), 1196–1205. <https://doi.org/10.1158/1078-0432.CCR-18-2407>.
- (24) Lechner, M. G.; Karimi, S. S.; Barry-Holson, K.; Angell, T. E.; Murphy, K. A.; Church, C. H.; Ohlfest, J. R.; Hu, P.; Epstein, A. L. Immunogenicity of Murine Solid Tumor Models as a Defining Feature of In Vivo Behavior and Response to Immunotherapy. *Journal of Immunotherapy* **2013**, *36* (9).
- (25) Wang, G.; Qi, J. Direct Estimation of Kinetic Parametric Images for Dynamic PET. *Theranostics* **2013**, *3* (10), 802–815. <https://doi.org/10.7150/thno.5130>.
- (26) Pai, C.-C. S.; Simons, D. M.; Lu, X.; Evans, M.; Wei, J.; Wang, Y.; Chen, M.; Huang, J.; Park, C.; Chang, A.; Wang, J.; Westmoreland, S.; Beam, C.; Banach, D.; Bowley, D.; Dong, F.; Seagal, J.; Ritacco, W.; Richardson, P. L.; Mitra, S.; Lynch, G.; Bousquet, P.; Mankovich, J.; Kingsbury, G.; Fong, L. Tumor-Conditional Anti-CTLA4 Uncouples Antitumor Efficacy from Immunotherapy-Related Toxicity. *J Clin Invest* **2019**, *129* (1), 349–363. <https://doi.org/10.1172/JCI123391>.
- (27) Ise, W.; Kohyama, M.; Nutsch, K. M.; Lee, H. M.; Suri, A.; Unanue, E. R.; Murphy, T. L.; Murphy, K. M. CTLA-4 Suppresses the Pathogenicity of Self Antigen-Specific T Cells by Cell-Intrinsic and Cell-Extrinsic Mechanisms. *Nature Immunology* **2010**, *11* (2), 129–135. <https://doi.org/10.1038/ni.1835>.
- (28) Brahmer, J. R.; Lacchetti, C.; Schneider, B. J.; Atkins, M. B.; Brassil, K. J.; Caterino, J. M.; Chau, I.; Ernstoff, M. S.; Gardner, J. M.; Ginex, P.; Hallmeyer, S.; Holter Chakrabarty, J.; Leighl, N. B.; Mammen, J. S.; McDermott, D. F.; Naing, A.; Nastoupil, L. J.; Phillips, T.; Porter, L. D.; Puzanov, I.; Reichner, C. A.; Santomaso, B. D.; Seigel, C.; Spira, A.; Suarez-Almazor, M. E.; Wang, Y.; Weber, J. S.; Wolchok, J. D.; Thompson, J. A. Management of Immune-Related Adverse Events in Patients Treated With Immune Checkpoint Inhibitor Therapy: American Society of Clinical Oncology Clinical Practice Guideline. *JCO* **2018**, *36* (17), 1714–1768. <https://doi.org/10.1200/JCO.2017.77.6385>.

- (29) Heusel, J. W.; Wesselschmidt, R. L.; Shresta, S.; Russell, J. H.; Ley, T. J. Cytotoxic Lymphocytes Require Granzyme B for the Rapid Induction of DNA Fragmentation and Apoptosis in Allogeneic Target Cells. *Cell* **1994**, *76* (6), 977–987.
[https://doi.org/10.1016/0092-8674\(94\)90376-X](https://doi.org/10.1016/0092-8674(94)90376-X).
- (30) Hiebert, P. R.; Granville, D. J. Granzyme B in Injury, Inflammation, and Repair. *Trends in Molecular Medicine* **2012**, *18* (12), 732–741.
<https://doi.org/10.1016/j.molmed.2012.09.009>.
- (31) Cullen, S. P.; Brunet, M.; Martin, S. J. Granzymes in Cancer and Immunity. *Cell Death & Differentiation* **2010**, *17* (4), 616–623. <https://doi.org/10.1038/cdd.2009.206>.
- (32) Hirota, J. A.; Hiebert, P. R.; Gold, M.; Wu, D.; Graydon, C.; Smith, J. A.; Ask, K.; McNagny, K.; Granville, D. J.; Knight, D. A. Granzyme B Deficiency Exacerbates Lung Inflammation in Mice after Acute Lung Injury. *Am J Respir Cell Mol Biol* **2013**, *49* (3), 453–462. <https://doi.org/10.1165/rcmb.2012-0512OC>.
- (33) Su, X.; Looney, M.; Robriquet, L.; Fang, X.; Matthay, M. A. DIRECT VISUAL INSTILLATION AS A METHOD FOR EFFICIENT DELIVERY OF FLUID INTO THE DISTAL AIRSPACES OF ANESTHETIZED MICE. *null* **2004**, *30* (6), 479–493.
<https://doi.org/10.1080/01902140490476382>.
- (34) D'Alessio, F. R.; Tsushima, K.; Aggarwal, N. R.; West, E. E.; Willett, M. H.; Britos, M. F.; Pipeling, M. R.; Brower, R. G.; Tuder, R. M.; McDyer, J. F.; King, L. S. CD4+CD25+Foxp3+ Tregs Resolve Experimental Lung Injury in Mice and Are Present in Humans with Acute Lung Injury. *J Clin Invest* **2009**, *119* (10), 2898–2913.
<https://doi.org/10.1172/JCI36498>.
- (35) Goggi, J. L.; Tan, Y. X.; Hartimath, S. V.; Jieu, B.; Hwang, Y. Y.; Jiang, L.; Boominathan, R.; Cheng, P.; Yuen, T. Y.; Chin, H. X.; Tang, J. R.; Larbi, A.; Chacko, A. M.; Renia, L.; Johannes, C.; Robins, E. G. Granzyme B PET Imaging of Immune Checkpoint Inhibitor Combinations in Colon Cancer Phenotypes. *Molecular Imaging and Biology* **2020**, *22*

- (5), 1392–1402. <https://doi.org/10.1007/s11307-020-01519-3>.
- (36) Aide, N.; Hicks, R. J.; Le Tourneau, C.; Lheureux, S.; Fanti, S.; Lopci, E. FDG PET/CT for Assessing Tumour Response to Immunotherapy. *European Journal of Nuclear Medicine and Molecular Imaging* **2019**, *46* (1), 238–250. <https://doi.org/10.1007/s00259-018-4171-4>.
- (37) Martin-Romano, P.; Castanon, E.; Ammari, S.; Champiat, S.; Hollebecque, A.; Postel-Vinay, S.; Baldini, C.; Varga, A.; Michot, J. M.; Vuagnat, P.; Marabelle, A.; Soria, J.-C.; Féré, C.; Massard, C. Evidence of Pseudoprogression in Patients Treated with PD1/PDL1 Antibodies across Tumor Types. *Cancer Medicine* **2020**, *9* (8), 2643–2652. <https://doi.org/10.1002/cam4.2797>.
- (38) Seo, J. W.; Tavaré, R.; Mahakian, L. M.; Silvestrini, M. T.; Tam, S.; Ingham, E. S.; Salazar, F. B.; Borowsky, A. D.; Wu, A. M.; Ferrara, K. W. CD8+ T-Cell Density Imaging with ⁶⁴Cu-Labeled Cys-Diabody Informs Immunotherapy Protocols. *Clinical Cancer Research* **2018**, *24* (20), 4976–4987. <https://doi.org/10.1158/1078-0432.CCR-18-0261>.
- (39) Freise, A. C.; Zettlitz, K. A.; Salazar, F. B.; Lu, X.; Tavaré, R.; Wu, A. M. ImmunoPET Imaging of Murine CD4+ T Cells Using Anti-CD4 Cys-Diabody: Effects of Protein Dose on T Cell Function and Imaging. *Molecular Imaging and Biology* **2017**, *19* (4), 599–609. <https://doi.org/10.1007/s11307-016-1032-z>.
- (40) Lee, J. T.; Campbell, D. O.; Satyamurthy, N.; Czernin, J.; Radu, C. G. Stratification of Nucleoside Analog Chemotherapy Using 1-(2'-Deoxy-2'-¹⁸F-Fluoro-β-d-Arabinofuranosyl)Cytosine and 1-(2'-Deoxy-2'-¹⁸F-Fluoro-β-|-Arabinofuranosyl)-5-Methylcytosine PET. *J Nucl Med* **2012**, *53* (2), 275. <https://doi.org/10.2967/jnumed.111.090407>.
- (41) Ronald, J. A.; Kim, B.-S.; Gowrishankar, G.; Namavari, M.; Alam, I. S.; D'Souza, A.; Nishikii, H.; Chuang, H.-Y.; Ilovich, O.; Lin, C.-F.; Reeves, R.; Shuhendler, A.; Hoehne, A.; Chan, C. T.; Baker, J.; Yaghoubi, S. S.; VanBrocklin, H. F.; Hawkins, R.; Franc, B. L.;

- Jivan, S.; Slater, J. B.; Verdin, E. F.; Gao, K. T.; Benjamin, J.; Negrin, R.; Gambhir, S. S. A PET Imaging Strategy to Visualize Activated T Cells in Acute Graft-versus-Host Disease Elicited by Allogenic Hematopoietic Cell Transplant. *Cancer Research* **2017**, *77* (11), 2893–2902. <https://doi.org/10.1158/0008-5472.CAN-16-2953>.
- (42) van de Donk, P. P.; Kist de Ruijter, L.; Lub-de Hooge, M. N.; Brouwers, A. H.; van der Wekken, A. J.; Oosting, S. F.; Fehrmann, R. S.; de Groot, D. J. A.; de Vries, E. G. Molecular Imaging Biomarkers for Immune Checkpoint Inhibitor Therapy. *Theranostics* **2020**, *10* (4), 1708–1718. <https://doi.org/10.7150/thno.38339>.
- (43) Ivry, S. L.; Sharib, J. M.; Dominguez, D. A.; Roy, N.; Hatcher, S. E.; Yip-Schneider, M. T.; Schmidt, C. M.; Brand, R. E.; Park, W. G.; Hebrok, M.; Kim, G. E.; O'Donoghue, A. J.; Kirkwood, K. S.; Craik, C. S. Global Protease Activity Profiling Provides Differential Diagnosis of Pancreatic Cysts. *Clinical Cancer Research* **2017**, *23* (16), 4865–4874. <https://doi.org/10.1158/1078-0432.CCR-16-2987>.
- (44) Salcedo, E. C.; Winter, M. B.; Khuri, N.; Knudsen, G. M.; Sali, A.; Craik, C. S. Global Protease Activity Profiling Identifies HER2-Driven Proteolysis in Breast Cancer. *ACS Chem. Biol.* **2021**, *16* (4), 712–723. <https://doi.org/10.1021/acscchembio.0c01000>.

CHAPTER 2

ENZYMATIC RADIOLABELING OF BIOMOLECULES VIA AN ENGINEERED LIPOIC ACID

LIGASE

ENZYMATIC RADIOLABELING OF BIOMOLECULES VIA AN ENGINEERED LIPOIC ACID LIGASE

2.1 Abstract

Positron emission tomography (PET) is an imaging modality that has made strong impacts in the clinic due to its ability to quantitatively and accurately measure disease biochemistry. PET, unlike ex-vivo tissue analysis that requires surgical resection, is a wholistic, noninvasive technology that does not suffer from tissue heterogeneity and has impacted cancer treatments via diagnostics, patient selection for targeted therapies, and quantifying patient responses. The most common PET radiotracer, fluorine-18 (¹⁸F) has made remarkable impacts in the field of immunoPET due to its sensitivity and high resolution images. Although ¹⁸F-conjugated antibodies have found much success, there is currently minimal widespread use of other ¹⁸F protein probes in the clinic. This can be attributed to the fact that there is an unmet need for more straightforward and consistent ¹⁸F radiofluorination techniques for more diverse protein scaffolds. Here, we describe a method that could broaden the application and targets of radiofluorination by developing a pipeline for enzymatically radiolabeling ¹⁸F onto proteins of interest that contain a specific recognition sequence. We engineered a variant of lipoic acid ligase (LP1A) to accommodate diverse scaffolds of ¹⁸F small molecules. Finally, the ligase was used in an application of a clinical molecule, Certolizumab pegol, which was expressed with the LP1A recognition sequence, enzymatically radiolabeled with the LP1A construct, and then imaged in an inflammatory murine model. Thus, we hope to have provided the radioimaging community with a potential avenue for radiolabeling other proteins of interest.

2.2 Introduction

PET is an imaging modality that has led to a regime change in clinical diagnostics, patient selection for immunotherapeutics, and quantitating responses to various therapies. Fluorodeoxyglucose (FDG) PET is the current imaging standard that is used for a broad range of cancer treatment regimes.¹ Fluorine-18 (¹⁸F) has unique characteristics due to his high positron decay ratio (97%), which leads to superb sensitivity. The low energy of the positrons (635 KeV) leads to high resolution images. F18 also benefits from a worldwide network of production that eases the barrier of clinical translation. With a half-life of ~109.7 minutes, this radionuclide allows quick imaging ~4-6 hours post-injection. Although all of these characteristics lead to beneficial properties in the clinic, the rapid decay associated with the half-life of ¹⁸F provides challenges, as the in vivo clearance of proteins conjugated with ¹⁸F must be matched to those of the radionuclide itself.

The vast majority of these immunoPET probes have been IgG antibodies labeled with radiotracers that have extended half-lives such as ⁸⁹Zr, ¹²⁴I, and ⁶⁴Cu.² This approach has shown clear clinical efficacy, but it is not without flaws. IgGs have significant circulation times in vivo (7-21 days) and they require an arduous protocol where PET imaging is acquired several days after probe injection to minimize background. Because of the long half-life of these radionuclide conjugated antibodies, patients are exposed to higher radiation doses ((~39.8-49.5 mSv^{3,4} compared to ~7 mSv⁵ for an ¹⁸F-FDG scan). Due to these caveats, lower molecular weight scaffolds such as Fabs have been introduced that still retain the high affinity binding properties of full length antibodies, but have much shorter circulating half-lives of 1-12 hours. These minimized half-lives allow for same day imaging and the utilization of the shorter half-life radiotracer ¹⁸F.

¹⁸F engineered protein scaffolds have found much success, including: affibodies, nanobodies, diabodies, and Fabs.⁶⁻⁹ With examples of these constructs finding success, it further highlights the stark contrast where there are little to no other ¹⁸F protein probes that are

widely used in the clinic.^{10,11} This evinces an unmet need where there is a lack of consistent and reliable radiofluorination techniques for other diverse protein constructs.¹⁰

The chemical conditions that are necessary for the formation of a stable, covalent carbon-18F bond are too severe for directly labeling the majority of proteins. Due to this obvious setback, researchers have developed numerous other radiofluorination protocols, summarized in Table 1. This list does not fully encapsulate the entirety of the literature regarding 18F conjugation^{6,7,9,12-14}, it provides a broad example of the main philosophies and methodologies currently in use. The simplest approach is to ligate an 18F-prosthetic, synthesized immediately before protein-of-interest (POI) labeling, onto endogenous residues. A hallmark of this approach utilized N-succinimidyl 4-18F-fluorobenzoate (**Table 2.1, line 1**), where an activated ester promiscuously reacts with any lysines exposed on the POI. This approach, albeit its popularity, suffers from multistep syntheses, low yields, large POI amounts required, and a severe lack of control over reactivity sites. This approach has even been shown to lead to reduced binding and immunoreactivity of antibody scaffolds.¹⁵ A similar approach has been used with cysteines and several prosthetics that take advantage of maleimide conjugations, including 18F-FBAM and 18F-FPEGMA.^{15,16} This approach has many caveats, as solvent-exposed cysteine are exceedingly rare, requiring the engineered variants that include them.¹⁵ Introducing unnatural cysteine creates very reactive residues that can lead to complications in expression and conjugation, yet it highlights a promising progression for the field of radiofluorine conjugation—the introduction of unnatural, reactive residues and tags onto a POI can be a advantageous approach.

Table 2.1: Published conditions for the formation of carbon 18-F bonds

	Methodology	Amount of peptide (nmol)	Solvent(s)	Time (mins)	Conjugation Temp (°C)	Yield (%)
1	[18F]-SFB/Lysine ¹⁵	135	MeCN/NaHPO ₄ (aq) (pH 8.5)	110	50	21-30
2	[18F]-Benzaldehyde/Oxime ¹⁷	25-100	Na(OAc) ₂ (pH 2.5)	90	60	40
3	[18F]-FBAM/Cysteine ¹⁵	5	MeOH/PBS	70	60	23
4	[18F]-trans-Cyclooctene/Tetrazine ¹⁸	10	DMSO/Ethanol	90	40	70
5	[18F]/SiFA ¹⁹	10-25	MeCN/DMSO	25	RT	46
6	Al[18F]/NOTA ²⁰	363	Na(OAc) ₂ (pH 4)	45	105	50
7	[18F]/Aryltrifluoroborate ¹²	50	DMF/Pyridazine(aq) (pH 2)	30	45	50

Rather than relying on single residue conjugation which currently relies on the functionality reactive amino acids, carrying all the caveats described above, other approaches have been proposed where reactive sites can be introduced through unnatural amino acids^{21,22} or by engineering endogenous site-specific tags that utilize protein ligation^{14,23–25}. Perhaps the furthest along approach in this regard is copper-free click chemistry. Copper-free click chemistry conjugates a tetrazine moiety onto a POI, and then ligates an ¹⁸F-trans-cyclooctene.²⁶ This protocol has many advantages, as the chemical reactions have a high yield at mildly high temperatures and also requires minimal POI (~10nmol). Yet, it should be noted that this method introduces a large hydrophobic moiety into the protein, which can directly impact pharmacokinetics of the diagnostic or therapeutic molecule. All the methods described above require preceding radiosynthesis of ¹⁸F-prosthetics. Methods that do directly radiofluorinate POIs at the site of the cyclotron have been reported which significantly streamlines the protocol. On the other hand, each of these methods require a preceding conjugation of an acceptor group onto the protein beforehand, and also rely on harsh reaction conditions such as acidic pH and extremely high temperatures (i.e. protein-NOTA/DOXA conjugations and Al-¹⁸F), while others rely on extremely large amounts of peptide precursor.^{7,13,20} These methods introduce further complications, such as increased uptake of Al-¹⁸F affibody in the kidney.²⁷

In an ideal scenario, radiofluorination would utilize a straightforward, high yielding prosthetic group during synthesis. The coupling of the ¹⁸F-prosthetic group onto the POI would be rapid, site specific, and high-yield under physiologically relevant conditions (aqueous, ambient temperature, neutral to physiological pH, etc). The resulting radiolabeled protein of interest would be stable and provide limited to no difference in protein pharmacokinetics, while the conjugation would require efficiently low amounts of protein reactant. This further highlights an unmet need, as there is no single methodology in existence that fulfills each of these criteria. Here, we strive towards the goal of approaching this unmet need by developing a pipeline for rapid, reliable, kit-based methodology for radiofluorination under mild conditions. This method

should be accessible to researchers and clinicians alike, and be able to be utilized with a broad range of protein constructs, promoting the discovery and use of a broad array of protein radiotracers in the clinic.

Here, we take advantage of work previously done in the Craik lab in collaboration with the Drake and VanBrocklin groups to show a proof-of-concept methodology where radiolabeling was enzymatically catalyzed.²³ In this case, an ¹⁸F-prosthetic was ligated onto proteins that were tagged with a 13-amino acid sequence (LAP-tag, **Fig. 2.1**). The ligation was shown to be rapid and high yielding in aqueous condition at physiological pH and ambient temperature. In these conditions, minimal protein loss is observed. The enzyme, lipoic acid ligase (LP1A), shows exquisite specificity, only ligating when the 13 amino acid tag is present, and only catalytic amounts of the ligase are required. Previously, the methodology revolved around the generation of a 7-(4-¹⁸F-fluorophenyl)-7-oxyheptanoic acid (FPOA). This FPOA ligation utilizes enzymatic amplification leading to a radiofluorinated product, which is a significant advance in the field of radiofluorination. To allow for more diverse radiofluorine containing small molecule scaffolds, W37ILPLA-His6 was utilized.²³ Here, we also describe the progress in optimizing the FPOA starting scaffold for the efficient ligation using the W37I variant, as well as showing the proof of concept of this platform with an inflammatory rheumatoid arthritic murine model.

2.3 Results

One of our first goals was to identify efficient precursors for the FPOA small molecule and then develop a full synthesis sequence and kit components to make ¹⁸F-FPOA on an ELIXYS system.

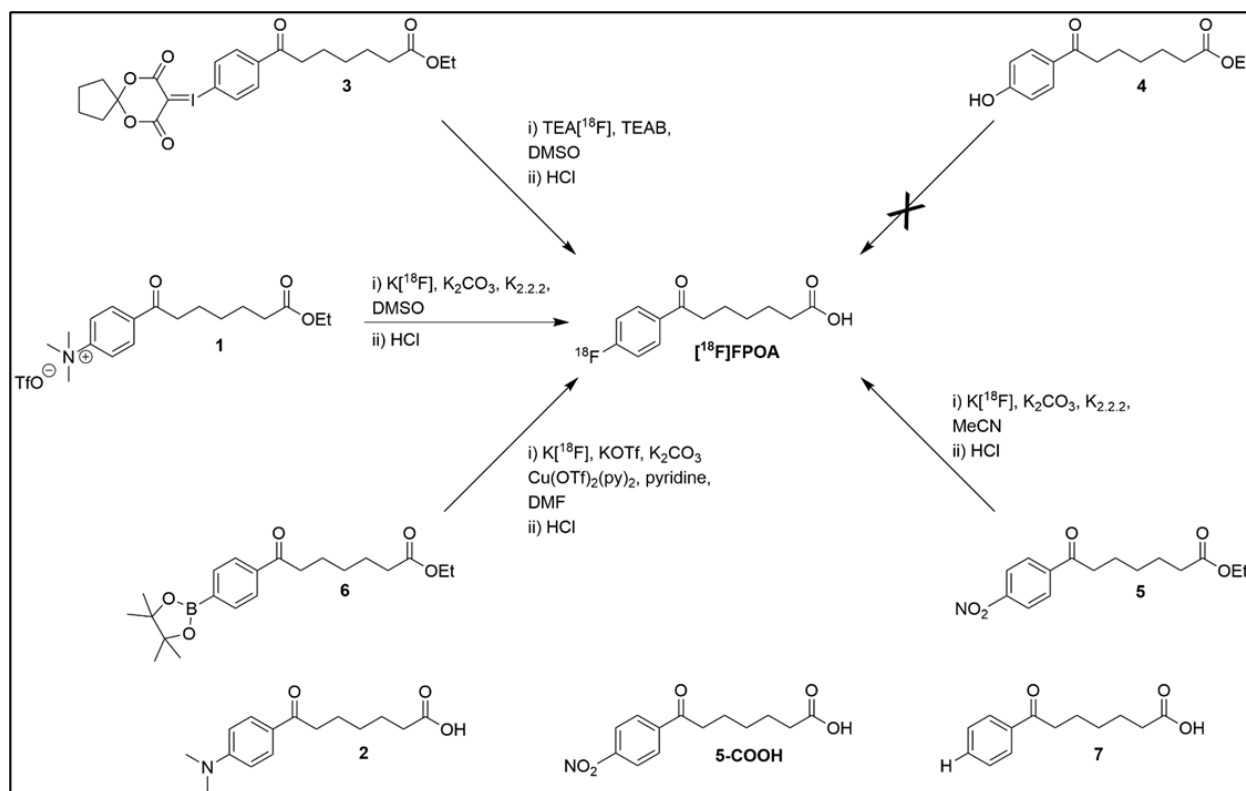


Figure 2.1: Summary of [^{18}F]FPOA Radiosyntheses Using Precursors 1, 3, 5, and 6. Optimal reagents shown for each precursor along with encountered impurities (2, 5-COOH, 7).

Precursor **5** was purchased from a commercial source (Rieke Metals). Various typical conditions for nucleophilic aromatic radiofluorinations were explored using radio-TLC to measure radiofluorination yields. A summary of the conditions/reagents screened is: Solvents including t -Butanol (t BuOH), Dimethylsulfoxide (DMSO), Acetonitrile (MeCN), Bases/eluents including Potassium carbonate / Kryptofix (K_2CO_3 / $\text{K}_{2.2.2}$), a reaction volume of 1.0 mL, base to precursor ratios of 0.3-2.0, and temperatures including 130 $^\circ\text{C}$, 150 $^\circ\text{C}$, 180 $^\circ\text{C}$. The optimal conditions identified, which gave radiofluorination yields of 71% ($n=2$), were 4.5-5.0 mg precursor **5**, 1.0 mg K_2CO_3 / 6.0 mg $\text{K}_{2.2.2}$; 1.0 mL acetonitrile; 180 $^\circ\text{C}$; 10 min.

Precursor **6** was synthesized by CalChem (San Diego, CA) on a 250 mg scale; the identity of the compound was confirmed by ^1H NMR and mass spectrometry and its purity was measured to be >95% by analytical HPLC. Various radiofluorination conditions based on literature precedent for boronate pinacol esters were explored^{28,29} and radiofluorination yields

were measured using radio-TLC. A summary of the conditions/reagents screened is: the solvent Dimethylformamide (DMF), Catalysts including $\text{Cu}(\text{OTf})_2 + \text{pyridine}$, $\text{Cu}(\text{OTf})_2(\text{py})_2 + \text{pyridine}$, $\text{Cu}(\text{OTf})_2(\text{py})_2$, bases/eluents including $\text{K}_2\text{CO}_3 / \text{K}_{2.2.2}$, Tetrabutylammonium bicarbonate (TBAHCO_3), Potassium acetate (KOAc), Potassium oxalate ($\text{K}_2\text{C}_2\text{O}_4$), Potassium triflate (KOTf) / K_2CO_3 , reaction volumes including 0.53-1.04 mL, base to precursor ratios including 1.36-6.8, and temperatures of 110 °C, 120 °C.

Initial radiofluorination tests were executed using 1.4-2.8 mg of precursor **6** and low radiofluorination yields of $\leq 25\%$ were obtained. Raising the amount of precursor **6** to 3.23-4.29 resulted in higher radiofluorination yields of 51-70%. The optimal conditions identified, which gave radiofluorination yields of $63 \pm 6\%$ ($n=17$) were 3-3.8 mg precursor **6**, 14-15 mg $\text{Cu}(\text{OTf})_2(\text{Py})_2$ catalyst with 30 μL pyridine additive, 0.5 mL DMF as solvent, 6 mg KOTf and 100 μg K_2CO_3 as base, 120 °C, 20 mins.

Precursor **3** was synthesized by CalChem on a 250 mg scale; the identity of the compound was confirmed by ^1H NMR and mass spectrometry and its purity was measured to be $>95\%$ by analytical HPLC. Various radiofluorination conditions based on literature precedent for iodonium salts were explored³⁰ and radiofluorination yields were measured using radio-TLC. A summary of the conditions/reagents screen is: solvents including DMF, DMSO, bases/eluents including $\text{K}_2\text{CO}_3 / \text{K}_{2.2.2}$, TBAHCO_3 , Tetraethylammonium bicarbonate (TEAB), reaction volumes including 0.4 mL, 0.5 mL, base to precursor ratios of 4-20, and temperatures of 120 °C, 150 °C.

The optimal conditions identified, which gave radiofluorination yields of $41 \pm 7\%$ ($n=6$) were 2 mg of precursor **3**, 0.5 mL DMSO as solvent, 4.2 mg TEAB as base/eluent, 150 °C, 20 mins. In summary, three potential [^{18}F]FPOA precursors were tested for radiofluorination and optimal conditions identified for each one. Precursor **5** met the criteria of radiofluorination yields of $>50\%$ in ≤ 10 mins reaction time and was investigated further in SA 1.2. Precursor **3** achieved radiofluorination yields of $41 \pm 7\%$ after 20 mins reaction time and precursor **6** achieved

radiofluorination yields of 63 ± 6 % after 20 mins reaction time. Both precursors **3** and **6** were also investigated in SA 1.2 due to the difficulties encountered purifying [^{18}F]FPOA using precursor **5**. Precursor **4** was not investigated as satisfactory radiofluorination yields were achieved with precursors **3**, **5**, and **6**.

Extensive optimization studies were undertaken with the aim of generating an ELIXYS sequence to synthesize [^{18}F]FPOA from **5**. Although radiofluorination yields of [^{18}F]FPOA were found to be >50% in 10 minutes, it was discovered that the hydrolyzed precursor (**5-COOH**, **Fig. 2.1**) co-eluted with the desired product ([^{18}F]FPOA) during purification by reverse-phase semi-preparative HPLC (SP-HPLC). This was confirmed by comparing the HPLC UV chromatogram of freshly prepared **5-COOH** with a non-radioactive reference standard of [^{18}F]FPOA. The co-elution of the undesired byproduct **5-COOH** greatly lowered the chemical purity and thus the effective specific activity of [^{18}F]FPOA. As a consequence, the required threshold for effective specific activity of 1000 Ci/mmol could not be achieved.

Due to the difficulties encountered purifying [^{18}F]FPOA synthesized from precursor **5**, ELIXYS sequences for [^{18}F]FPOA synthesis were developed for both precursors **3** and **6** despite their lower radiofluorination yields. In both cases reliably purifying [^{18}F]FPOA proved to be challenging. In the case of precursor **6**, an impurity was discovered to nearly co-elute with [^{18}F]FPOA on reverse-phase HPLC, complicating purification. Based on literature precedent²⁹ and previous experience with radiofluorination of analogous aryl Bpin precursors, the impurity was presumed to be **7** (**Fig. 2.1**), the product of competing protodeboronation of **6**. Using the optimized SP-HPLC conditions developed, satisfactory chemical purities and effective specific activities could be achieved. However the synthesis was not reliable, presumably due to variations in the amount of **7** formed during the radiofluorination step and this impurity was frequently observed in the [^{18}F]FPOA product, lowering effective specific activities to <1000 Ci/mmol. Similarly for precursor **5**, a close eluting impurity was observed which complicated

[¹⁸F]FPOA purification and again, despite extensive attempts to optimize the purification conditions, prevented the development of a reliable [¹⁸F]FPOA synthesis.

At this juncture, four productive precursors for [¹⁸F]FPOA synthesis had been identified (**1**, **3**, **5**, **6**), however the use of each one had been stymied by chemically similar impurities which proved difficult to remove. Reviewing the impurities generated for each precursor, it was decided to refocus efforts on [¹⁸F]FPOA synthesis using precursor **1**. The rationale was that the known major interfering impurity from **1** was the dimethylaniline **2** whose affinity for reverse-phase solid phases could presumably be altered via protonation under strongly acidic conditions. In contrast, the presumed impurities generated from precursor **5** (**5-COOH**) and **3/6** (**7**) could not be similarly manipulated as they do not contain ionizable moieties. A further extensive optimization of purification conditions for [¹⁸F]FPOA synthesized from precursor **1** was completed and an optimal protocol was identified. Following deprotection, the crude reaction mixture was acidified via the addition of 1% trifluoroacetic acid (TFA) and passed over a C₁₈ SPE cartridge, trapping [¹⁸F]FPOA and various impurities. The C₁₈ cartridge was then sequentially washed with 20% MeCN in 1% TFA, 30% MeCN in 1% TFA, and finally 40% MeCN in 1% TFA. The semi-purified product was then washed from the cartridge and terminally purified via SP-HPLC. See table 1 for a summary of the full optimized [¹⁸F]FPOA synthesis from **1**.

Table 2.2: Summary of ELIXYS Sequence for [¹⁸F]FPOA Synthesis

Step 1	[¹⁸ F]Fluoride trapped on QMA light solid-phase extraction cartridge and subsequently eluted into ELIXYS reaction vial with a solution of K ₂ CO ₃ (1 mg) and K _{2.2.2} (6.2 mg) in 1:1 MeCN/H ₂ O (1 mL)
Step 2	[¹⁸ F]Fluoride and eluent mixture azeotropically dried using 2 x additions of MeCN (1 mL each), forming K _{2.2.2} ¹⁸ F complex
Step 3	Precursor 1 in anhydrous DMSO (0.5 mL) added and resulting solution heated at 130 °C for 5 mins
Step 5	Solution diluted with 1% aqueous TFA (3.5 mL) and resulting crude reaction mixture passed over C18 plus short cartridge
Step 6	C ₁₈ plus short cartridge washed with 20:80, v:v, MeCN:0.1% aqueous TFA (3 mL)
Step 7	C ₁₈ plus short cartridge washed with 30:70, v:v, MeCN:0.1% aqueous TFA (3 mL)
Step 8	C ₁₈ plus short cartridge washed with 40:60, v:v, MeCN:0.1% aqueous TFA (3 mL)
Step 9	C ₁₈ plus short cartridge eluted with MeCN (2 mL) into second ELIXYS reactor and MeCN evaporated
Step 10	1:1 6 M HCl/ MeCN (2 mL) added and resulting solution heated at 130 °C for 5 mins for affect hydrolysis/deprotection of ester moiety
Step 11	Hydrolysis reaction was diluted in 1:1 MeCN/ water (2 mL) and purified via semi preparative HPLC using a Hamilton PRP-1 10 mm 250 x 10 mm column eluted at 6 mL/min with 40:60:0.1% MeCN/ water/ TFA
Step 12	Purified [¹⁸ F]FPOA diluted with 40 mL of water and reformulated into MeCN (2 mL) using C ₁₈ plus short extraction cartridge

Following the establishment of an optimized [¹⁸F]FPOA synthesis, three sequential qualification syntheses were executed, measuring time-of-synthesis, decay-corrected yield, radiochemical purity by HPLC, chemical purity by HPLC, and effective specific activity. (Table 2.3)

Table 2.3: Summary of [¹⁸F]FPOA Qualification Syntheses

Date	Reaction time (mins)	Decay-corrected Yield	Radiochemical purity	Chemical purity	Effective specific activity (Ci/mmol)
01/15/21	121	16.9	>99%	40%	2250
01/20/21	120	33.3	>99%	85%	1820
01/22/21	122	32.1	>99%	46%	1920

During the three-in-series validation syntheses, uniformly high radiochemical purities (>99%) and effective specific activities (>1000 Ci/mmol) were obtained, meeting the acceptance criteria. The chemical purity varied between 40-85%, presumably due to varying amounts of impurity **2** generated during the syntheses. Despite the chemical purities falling below the desired threshold of 95%, the high effective specific activities made us confident that high conjugation yields to LAP-tagged peptides could be achieved. Decay-corrected yields were within expectations for 2/3 syntheses; the yield of 16.9% on 01/15/21 was lower than expected. Taken together, it was judged that these features were sufficient to proceed onto conjugation [¹⁸F]FPOA to peptides.

Due to stability issues encountered with the ^{W371}LpLA enzyme (*vide infra*), no attempts were made to generate kit components for this methodology. However, as assessment can be made of the suitability of the reagents for [¹⁸F]FPOA synthesis for inclusion within a kit. A list of all required reagents for the optimized synthesis, along with suppliers and maximum amounts available commercially. (**Table 2.4**)

Table 2.4: Materials Required for [¹⁸F]FPOA Radiosynthesis

Material	Amount used per [¹⁸F]FPOA synthesis	Supplier	Maximum amount available
Precursor 1	5.0 mg	N/A	N/A
K ₂ .2.2	6.2 mg	Sigma Aldrich	1 g
K ₂ CO ₃	1 mg	Sigma Aldrich	5 g
MeCN	10.2 mL	Sigma Aldrich	100 mL
DMSO	0.5 mL	Sigma Aldrich	100 mL
HCl (12 M)	0.5 mL	Sigma Aldrich	1 L
TFA	0.1 mL	Sigma Aldrich	100 mL
Water (HPLC grade)	55.5 mL	Sigma Aldrich	4 L
QMA SPE cartridge	1	Waters	Box of 50
C18 plus short SPE cartridge	2	Waters	Box of 50

Apart from precursor **1** all materials are available commercially in sufficient quantity for kit production. With respect to precursor **1**, the starting material required for its production (ethyl 7-[4-(*N,N*-dimethylamino)phenyl]-7-oxoheptanoate) is available on a multi-gram scale from Rieke Metals. The 1-step synthesis required to synthesize **1** is amenable to scale-up due to the straightforward synthesis and work-up, high yield (~75%) and purification via recrystallization.

At the outset of work on this aim, we decided to simplify our planned purification scheme for the radiofluorinated final products. Previously,²³ nickel-affinity chromatography was used to purify the radiofluorinated protein products of ECR from the ligation reaction mixture. While effective, the procedure was time-consuming and generated the products in a 250 mM imidazole solution, potentially requiring further buffer exchange prior to use. Instead, we decided to use nickel-affinity chromatography to remove ^{W371}LpIA from the reaction mixture and then employ size-exclusion chromatography (SEC) to terminally purify the final product. If the radiofluorinated protein product was sufficiently resolved from ^{W371}LpIA via SEC, then even the nickel-affinity chromatography step would not be required.

With this optimization of the purification protocol in mind, we scaled-up production of ^{W371}LpIA with the His₆ tag still attached. ^{W371}LpIA was cloned into a PQE-2, ampicillin-resistant bacterial vector, which was then transformed into BL21 bacterial cells. The plasmid was purified and characterized to verify it contained the correct ^{W371}LpIA sequence. 10 mL overnight cultures of BL21 cells with the expression vector were started in LB-broth containing ampicillin. Each 10 mL starter culture was then added to 1 L LB media with ampicillin and shaken at 200 rpm at 37°C. OD was monitored and upon OD₆₀₀=0.6, isopropyl β-D-1-thiogalactopyranoside was added to induce ^{W371}LpIA expression. Upon initiation of induction, cells were shaken at 200 rpm at 30 °C for 4 hours. Cell-containing media was then centrifuged to pellet cells, which were subsequently resuspended in lysis buffer. Resuspended cells were then disrupted using sonication and the resultant cell lysate centrifuged. The supernatant was decanted and incubated with Nickel-NTA beads overnight while rotating at 4°C. Beads were then washed with

20 mM imidazole and then eluted with 500 mM imidazole and at least ten 1.5 mL fractions were collected. Fractions were analyzed via SDS-gel and fractions containing bands at ~39 kDa, the molecular weight of W371 LpIA, were carried forward. Fractions containing W371 LpIA correlating bands were buffer exchanged into PBS, pooled, and purified via SEC. Purified product was then verified for purity using FPLC, SDS-PAGE, and anti-His-tag staining immunoblotting (**Fig. 2.2**). Yield was verified by BCA assay to determine protein concentration.

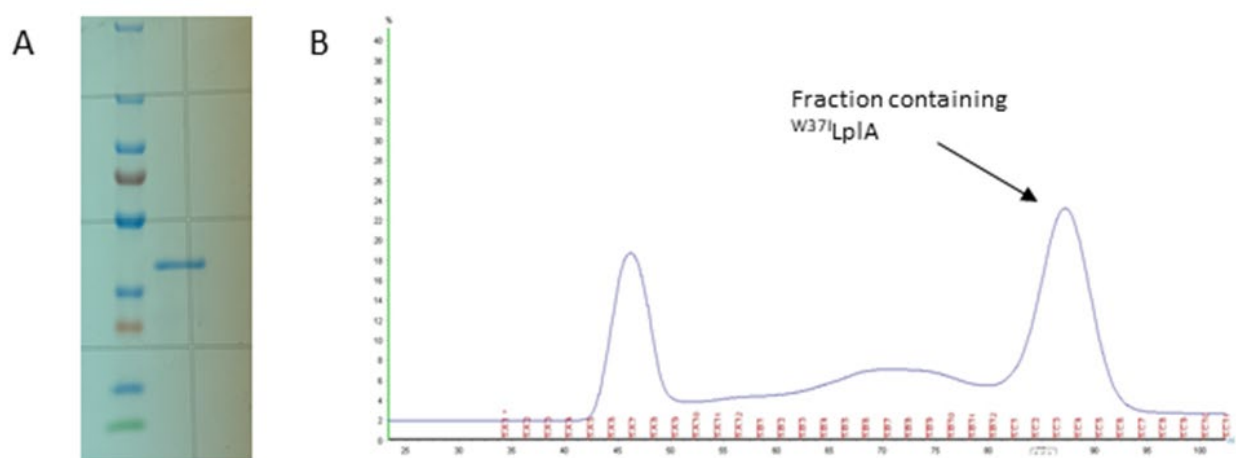


Figure 2.2: W371 LpIA Production. A: Analysis of purified W371 LpIA via SDS-PAGE demonstrating high purity, ii) FPLC chromatogram from W371 LpIA purification.

W371 LpIA production was executed on a 6 L scale, generating 102 mg of the enzyme at a concentration of 17 mg/mL. With W371 LpIA in hand, a non-radioactive enzymatic activity assay for W371 LpIA was developed based on a previously reported protocol for another LpIA variant.³¹ The W371 LpIA enzyme (500 nM) was incubated with LAP peptide (750 μ M), ATP (300 mM), and $Mg(OAc)_2$ (2 mM) with various concentrations of non-radioactive reference standard FPOA (10, 50, 100, 250, and 500 μ M; n =3 for each concentration) at 30 °C. At 1, 3, 5, 10, 15, and 30 minute time-points, aliquots were taken and quenched with an EDTA solution to a final concentration of 50 mM. The conversion of LAP to the ligated LAP-FPOA species was measured via HPLC and peak intensities were converted to molar concentrations using a

standard curve of LAP-FPOA. Molar concentration was calculated over time for each FPOA concentration to calculate molar velocities that were then used to plot Michaelis-Menten curves and derive the kinetic values K_M , k_{cat} , and V_{max} . The Michaelis-Menten curve from the initial ^{37}I LpIA solution (prior to storage) is shown in figure 2.3; values of $K_M = 59 \mu\text{M}$, $k_{cat} = 0.086 \text{ sec}^{-1}$ and $V_{max} = 0.043$ were calculated from this data. (**Fig. 2.3**)

The ^{37}I LpIA produced was then combined with ATP (final concentration, 3 mM) and $\text{Mg}(\text{OAc})_2$ (final concentration, 5 mM) to generate the Ligation Reagent. To simplify the composition of the Ligation Reagent, it was decided to reconstitute the $[^{18}\text{F}]\text{FPOA}$ in 9:1, v:v, PBS:DMSO prior to addition of the Ligation Reagent, rather than include DMSO in this solution. The efficiency of the Ligation Reagent for $[^{18}\text{F}]\text{FPOA}$ ligations to a known model system was then investigated. Due to COVID-related restrictions at the time of these studies, it was not possible to generate 2G10-LAP for these studies; instead, the isolated LAP peptide was used and the ligation data benchmarked against that reported previously.¹ The LAP peptide (5 μM , 1 nmol) was incubated with the Ligation Reagent (containing 2.5 μM ^{37}I LpIA) and $[^{18}\text{F}]\text{FPOA}$ reconstituted in 9:1, v:v, PBS:DMSO (90 μCi – 2.6 mCi); the final reaction volumes for these tests were 200 μL and the solutions were incubated at 30 °C for 10 mins prior to analysis via TLC using the previously reported method.⁴ Ligation yields of 84% (90 μCi $[^{18}\text{F}]\text{FPOA}$), 91% (850 μCi $[^{18}\text{F}]\text{FPOA}$), and 72% (2.6 mCi $[^{18}\text{F}]\text{FPOA}$) were measured. Previously, using 2G10-LAP as a model system, far higher amounts of LAP-tagged protein (10 nmol) had been required to achieve high ligation yields with >2 mCi $[^{18}\text{F}]\text{FPOA}$. Thus, achieving ligation yields of 72% using ^{37}I LpIA and $[^{18}\text{F}]\text{FPOA}$ with only 1 nmol LAP suggests a significant improvement of this second-generation ECR protocol.

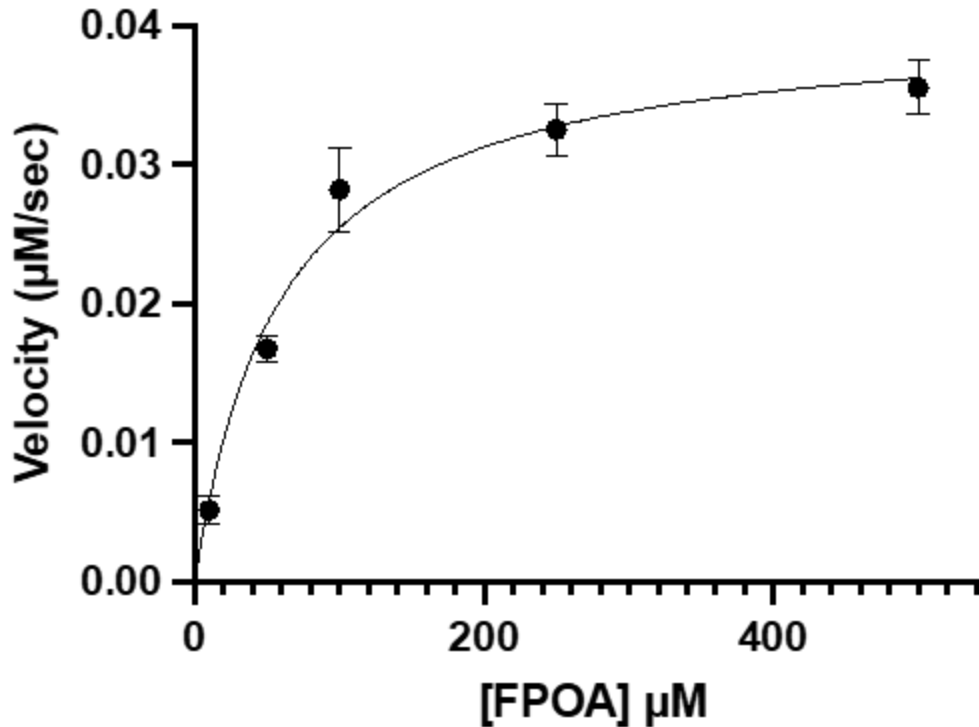


Figure 2.3: Michaelis-Menten curve for freshly prepared W371 LpIA stock solution.

The stability of the W371 LpIA stock solutions at 4 °C and -80 °C after 2 months storage was also evaluated using the enzymatic activity assay described above (**Fig. 2.4**). The enzymatic activity was retained at -80 °C, however activity was significantly reduced after only 2 months at 4 °C. At this juncture, restrictions imposed by the COVID-19 pandemic required cessation of enzyme activity measurements for the -80 °C sample and no data for -20 °C storage could be acquired. When it was possible to measure the activity of the -80 °C sample again, in parallel with the Cimzia-LAP labeling studies, it was discovered that its activity had decreased by ~88% ($V_{500\mu\text{M}} = 0.0043 \mu\text{M}/\text{sec}$, compared to $0.036 \mu\text{M}/\text{sec}$ for freshly prepared W371 LpIA), indicating that even storage at -80 °C was not sufficient for long-term storage.

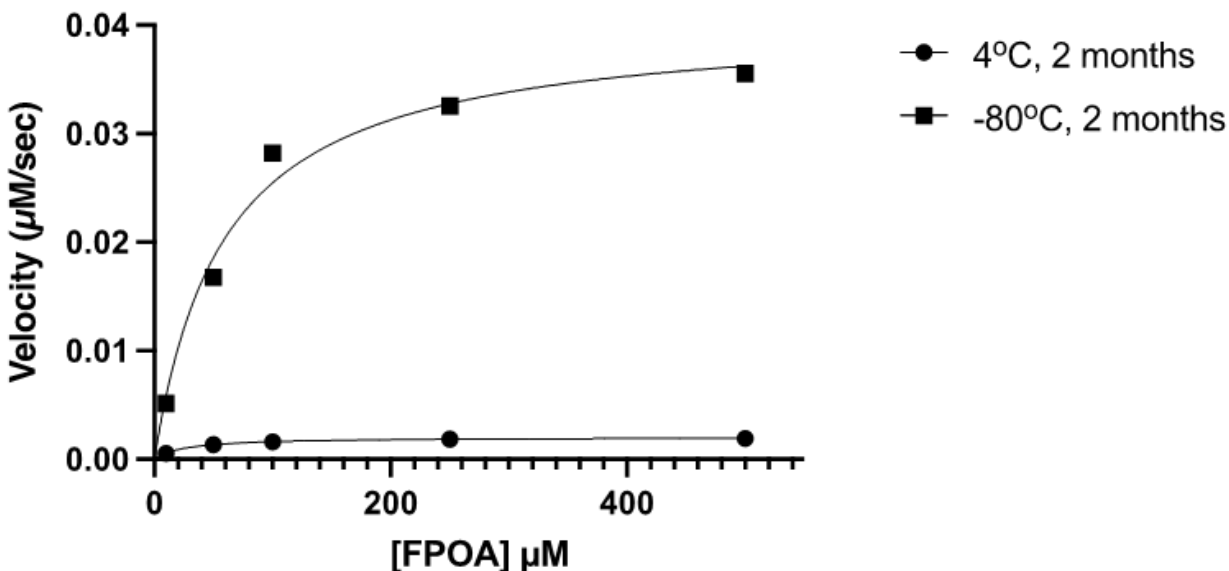


Figure 2.4: Michaelis-Menten curves for W371 LpIA solutions stored at 4 °C and -80 °C for 2 months.

Overall, we demonstrated that it was possible to significantly scale-up the production of W371 LpIA and that the [18 F]FPOA / W371 LpIA system achieved higher ligations to a model LAP system than the previously reported iteration of ECR. However, the long-term stability studies revealed that, even when stored at -80 °C, W371 LpIA exhibits instability which impacts its use for the ECR method. Unfortunately due to interruptions caused by the COVID-19 pandemic it was not possible to obtain a full picture of W371 LpIA stability across all proposed temperatures. That being said, the instability observed precluded the development of ECR-based kits. Further research into W371 LpIA stability under a range of buffers and conditions is required to determine whether the enzymatic reagent is suitable for centralized production, storage, and distribution.

We were able to simplify the purification protocol for ECR by retaining the His₆ tag on W371 LpIA and ensuring that the protein to be labeled was not His₆ tagged. Hence, terminal purification of 18 F-labeled proteins could be achieved either via SEC alone (if the molecular weight was sufficiently different from W371 LpIA), or by simply passing the ligation reaction mixture through a nickel-affinity column prior to SEC. W371 LpIA proved unsuitable for long-term storage

even at -80 °C, preventing us from pursuing kit development as originally proposed. Hence no high activity radiosynthesis with 2G10-Fab-LAP were executed.

The goal of the project changed from simply generating a set of instructions for introducing the LAP-tag to a protein of interest to engaging a commercial contract research organization (CRO) to produce a LAP-tagged protein. We chose to work with Cimzia (certolizumab pegol), a PEGylated Fab' antibody fragment which targets Tumor Necrosis Factor α (TNF α) due to the previous experience of Dr. VanBrocklin's group with this model. Previously, zirconium-89 radiolabeled Cimzia derivatives have been used to image TNF α expression in rodent inflammation models with a view to creating a PET drug capable of measuring response to therapy for diseases such as rheumatoid arthritis.¹⁶ The favorable imaging characteristics of fluorine-18 along with the appropriate half-life of Cimzia makes development of a radiofluorinated Cimzia derivative an attractive goal.

We engaged LakePharma (CA, USA), a CRO specializing in producing custom biologics, and agreed to terms for the supply of ~20 mg of LAP-tagged Cimzia. Using the publicly available amino acid sequence for certolizumab, we provided Lake Pharma with a target amino acid sequence for certolizumab-LAP, introducing the LAP-tag at the C-terminus of the protein as we had done previously for 2G10-LAP.²⁸ Following production and purification of certolizumab-LAP, site-specific PEGylation based on a previously published protocol⁷ was executed by LakePharma to generate Cimzia-LAP. Initially, LakePharma generated an expression vector for certolizumab-LAP using their proprietary expression vector system and scaled this to 0.03 L. Using their TunaCHO™ platform for transient protein production, certolizumab-LAP was then produced in CHO cells and purified via protein A solid-phase extraction. This process was then scaled up to the 1.0 L DNA scale to generate sufficient certolizumab for PEGylation studies.

PEGylation of certolizumab-LAP to generate Cimzia-LAP required site-specific conjugation of a single 40 kDa branched PEG-maleimide polymer (MPEG2-LYS-MAL), which

was purchased from JenKem technologies, to a cysteine residue on certolizumab-LAP. Crude PEGylation reactions were analyzed using SDS-PAGE to measure conversion and assess the number of PEG moieties conjugated per certolizumab. Initial attempts to replicate the published PEGylation conditions resulted in poor PEGylation yields and little evidence of the formation of Cimzia-LAP. Responsive to these results, various PEGylation conditions were screened on a small scale and the efficacy of PEGylation assessed using SDS-PAGE. Conditions investigated included: Reducing agent: tris(2-carboxyethyl)phosphine (TCEP), cystamine, no reducing agent, concentration of reducing agent, ratio of certolizumab to PEG-maleimide: 1:1 to 1:14, and conjugation time. The optimal PEGylation conditions identified were: reduction with 10 mM TCEP for 30 minutes at ambient temperature, buffer exchange into 20 mM sodium phosphate, 150 mM NaCl, pH 7.2 while also removing TCEP, incubation with PEG-maleimide for 3 hours at molar ratio of 1:3 (certolizumab:PEG-maleimide), and purification via size-exclusion chromatography.

SDS-PAGE was used to analyze the composition of the SEC fractions obtained and revealed that all relevant fractions contained a mixture of mono-, di-, and tri-PEGylated species which could not be further separated. At this juncture, due to time constraints, it was decided to move forward with the mixture of PEGylated material obtained for labeling and imaging studies. These results provide a benchmark to compare results obtained by labeling Cimzia-LAP via ECR and using the resulting imaging agent in equivalent studies. Hence, despite the inability to obtain purely mono-PEGylated Cimzia-LAP, meaningful data on the performance of ECR can be obtained using the Cimzia-LAP mixture from LakePharma.

Overall, LakePharma provided 33.7 mg (370 nmol) of Cimzia-LAP mixture, sufficient for 30-40 labeling reactions, demonstrating that LAP-tagged proteins are accessible from CROs. Although difficulties were encountered with PEGylation of certolizumab, this aspect of Cimzia production is not related to the ECR method and does not impact its general application to a

range of target proteins. The Cimzia-LAP mixture of mono-, di-, and tri-PEGylated species was carried forward for the studies.

The goal after a change of scope was to optimize the synthesis of [¹⁸F]LAP-Cimzia prior to preclinical imaging studies (SA3.2). Initial attempts to ligate [¹⁸F]FPOA to the Cimzia-LAP produced in SA2.3 gave low conjugation yields by TLC (<25%) and no [¹⁸F]LAP-Cimzia could be isolated following purification by size-exclusion chromatography (SEC). To further investigate the root cause for the observed low yields, we measured the enzymatic activity of our ^{W37I}LpIA stock solutions, which had been stored at -80 °C, using the assay described in SA2.1. Unfortunately, the assay revealed that enzymatic activity had decreased by ~88%. In addition, protein concentration measurements also revealed significantly lower ^{W37I}LpIA concentrations than expected, indicating that the enzyme had precipitated during storage. At this juncture, due to time constraints, it was decided to move away from optimizing the conjugation of [¹⁸F]FPOA to Cimzia-LAP as originally envisaged in SA3.1 and instead focus on producing sufficient [¹⁸F]LAP-Cimzia for the preclinical studies in SA3.2. Cimzia-LAP (76.5 μM, 20 nmol) was incubated with [¹⁸F]FPOA (14.6-25 mCi) and ^{W37I}LpIA (2.5-6.8 μM) in PBS with 3 mM ATP and 5 mM Mg(OAc)₂ (~200 μL final volume). Despite the concentration of ^{W37I}LpIA being as high as could be achieved using the available enzymatic stock solutions, poor ligation yields were measured by TLC (5-26%) and only minimal amount of material could be isolated after SEC (180-200 μCi). Due to the low isolated yields, no QC tests were executed and there was insufficient material to be deemed usable for the proposed studies in SA3.2. Overall, the lack of stability ^{W37I}LpIA even when stored at -80 °C prevented any significant optimization of [¹⁸F]LAP-Cimzia synthesis and, due to time and resource constraints, no further batches of the enzyme could be produced.

An established transgenic TNFα mouse model was purchased from Taconic Biosciences for imaging studies to test [¹⁸F]LAP-Cimzia and [¹⁸F]SFB-Cimzia. These mice develop chronic inflammatory arthritis by the age of 20 weeks, and the condition progressively deteriorates as

they age. As such, it has been used previously to image TNF α accumulation in arthritic joints using Cimzia-derived PET drugs.⁶ However, the issues prevented any imaging data being acquired with [¹⁸F]LAP-Cimzia as usable amounts of this radiotracer could not be isolated. In addition, it was not feasible to measure the immunoreactivity or serum stability of [¹⁸F]LAP-Cimzia as had been envisaged.

It was possible to acquire data using Cimzia-LAP labeled using [¹⁸F]SFB, the current gold standard in the field. [¹⁸F]SFB was synthesized on ELIXYS using a previously published protocol.³² Approximately 8 mg of Cimzia-LAP was then labeled with this [¹⁸F]SFB (50.9 mCi) under standard conditions for this conjugation (pH 9 buffer, ambient temperature). The resulting conjugate was then purified via SEC to generate [¹⁸F]-SFB-Cimzia-LAP in a non-decay-corrected yield of 34% from [¹⁸F]SFB. The radiochemical purity of the final product was >99% by analytical SEC. 37-week old transgenic TNF α were injected with [CD1] μ Ci of [¹⁸F]-SFB-Cimzia-LAP. Two hours after injection mice were imaged by PET/CT using a 20-minute acquisition time to generate the images (**Fig. 2.5a**); for comparison, images acquired using commercially available Cimzia also labeled with [¹⁸F]SFB ([¹⁸F]SFB-Cimzia) are also shown (**Fig. 2.5b**). Comparable uptake in knee joints, heel joints, and paws is exhibited using both Cimzia radiotracers, supporting the conclusion that introduction of the LAP-tag does not affect the affinity of Cimzia for TNF α .

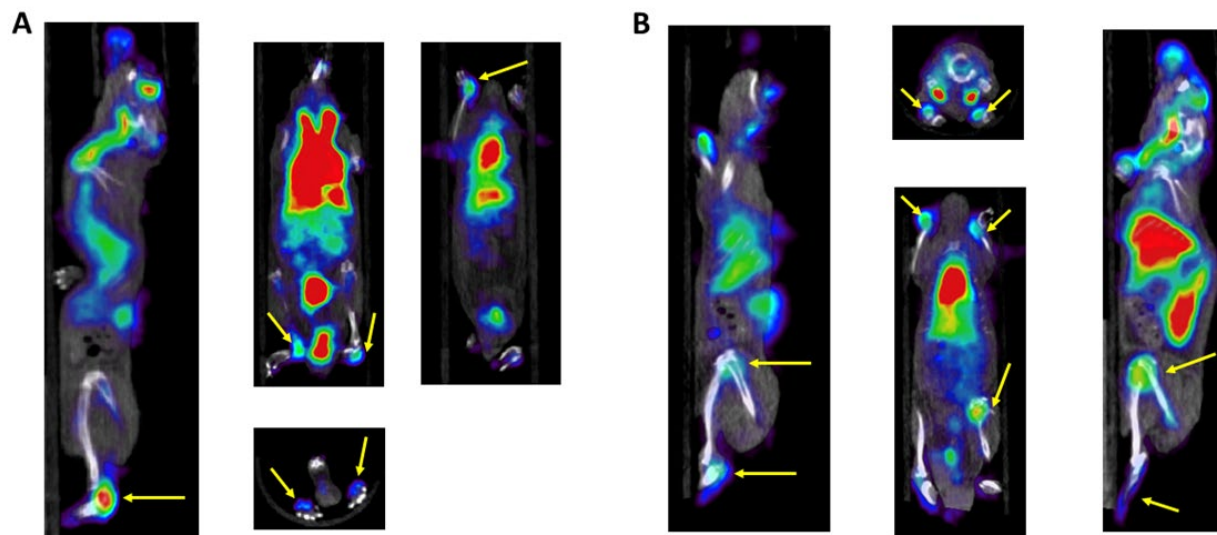


Figure 2.5: Imaging of transgenic TNF α mice. (a) [^{18}F]SFB-Cimzia-LAP and (b) [^{18}F]SFB-Cimzia. Sagittal, coronal, and axial viewpoints included for both cohorts. Areas of PET radiotracer uptake in knee joints, heel joints, and paws, indicating areas of TNF α infiltration, are highlighted with arrows.

2.4 Discussion

All-in-all significant progress was made in many aspects of developing ECR into a commercial product, however the instability of the W371 LpIA to storage (even at $-80\text{ }^{\circ}\text{C}$) hindered progress for many of the later goals. We successfully developed a reliable method for producing high molar activity [^{18}F]FPOA in reasonable radiochemical yields on the ELIXYS module. We scaled-up W371 LpIA production to a batch of 102 mg, far greater than our targeted 25 mg batch scale and sufficient for ~ 400 radiosyntheses. We also established an enzymatic activity assay for W371 LpIA and utilized it to start assessing enzymatic stability at various storage temperatures. Unfortunately these studies were interrupted by the COVID-19 pandemic, and when we were able to restart them we discovered that the enzyme had lost $\sim 88\%$ of its activity despite rigorous storage conditions of $-80\text{ }^{\circ}\text{C}$. This was highly unexpected as we had not previously observed loss of enzymatic activity for the wild-type enzyme under similar storage conditions. Further investigation is required to establish a root cause for the loss of activity and to develop conditions which permit long-term storage. Until this issue is resolved, developing an ECR kit is

not feasible. Additionally, we employed a CRO to generate a LAP-tagged protein, Cimzia-LAP. Introducing the LAP-tag proved straightforward, demonstrating that this aspect of the ECR method should not prevent its use by other groups. Our goal was to optimize the radiosynthesis of [^{18}F]LAP-Cimzia, test it in an established preclinical murine model and benchmark the data against [^{18}F]SFB-Cimzia. These studies were severely impacted by the instability of our ^{37}I LpIA stocks which resulted in poor ligation yields for [^{18}F]FPOA to Cimzia-LAP and prevented us producing sufficient [^{18}F]LAP-Cimzia for the preclinical studies. After the completion of the funding period, we were able to produce another batch of ^{37}I LpIA and use it to produce [^{18}F]LAP-Cimzia for preclinical studies. This data is not reported herein as it did not fall within the funding period of this award, however we expect to report it via publication in due course.

2.5 Methods

FPOA Synthesis

Precursor **5** was purchased from a commercial source (Rieke Metals). Various typical conditions for nucleophilic aromatic radiofluorinations were explored using radio-TLC to measure radiofluorination yields. Solvents include: t -Butanol (t BuOH), Dimethylsulfoxide (DMSO), Acetonitrile (MeCN). Bases/eluents include: Potassium carbonate / Kryptofix (K_2CO_3 / $\text{K}_{2.2.2}$), a reaction volume of 1.0 mL, base to precursor ratios of 0.3-2.0, and temperatures include 130 °C, 150 °C, 180 °C. The optimal conditions identified, which gave radiofluorination yields of 71% ($n=2$), were 4.5-5.0 mg precursor **5**, 1.0 mg K_2CO_3 / 6.0 mg $\text{K}_{2.2.2}$; 1.0 mL acetonitrile; 180 °C; 10 min.

Precursor **6** was synthesized by CalChem (San Diego, CA) on a 250 mg scale; the identity of the compound was confirmed by ^1H NMR and mass spectrometry and its purity was measured to be >95% by analytical HPLC. Various radiofluorination conditions based on literature precedent for boronate pinacol esters were explored^{28,29} and radiofluorination yields were measured using radio-TLC. A summary of the conditions/reagents screened is: the solvent Dimethylformamide (DMF), Catalysts including $\text{Cu}(\text{OTf})_2$ + pyridine, $\text{Cu}(\text{OTf})_2(\text{py})_2$ + pyridine,

Cu(OTf)₂(py)₂, bases/eluents including K₂CO₃/ K_{2.2.2}, Tetrabutylammonium bicarbonate (TBAHCO₃), Potassium acetate (KOAc), Potassium oxalate (K₂C₂O₄), Potassium triflate (KOTf) / K₂CO₃, reaction volumes including 0.53-1.04 mL, base to precursor ratios including 1.36-6.8, and temperatures of 110 °C, 120 °C.

Initial radiofluorination tests were executed using 1.4-2.8 mg of precursor **6** and low radiofluorination yields of ≤25% were obtained. Raising the amount of precursor **6** to 3.23-4.29 resulted in higher radiofluorination yields of 51-70%. The optimal conditions identified, which gave radiofluorination yields of 63 ± 6 % (n=17) were 3-3.8 mg precursor **6**, 14-15 mg Cu(OTf)₂(Py)₂ catalyst with 30 µL pyridine additive, 0.5 mL DMF as solvent, 6 mg KOTf and 100 µg K₂CO₃ as base, 120 °C, 20 mins.

Precursor **3** was synthesized by CalChem on a 250 mg scale; the identity of the compound was confirmed by ¹H NMR and mass spectrometry and its purity was measured to be >95% by analytical HPLC. Various radiofluorination conditions based on literature precedent for iodonium salts were explored³⁰ and radiofluorination yields were measured using radio-TLC. A summary of the conditions/reagents screen is: solvents including DMF, DMSO, bases/eluents including K₂CO₃/K_{2.2.2}, TBAHCO₃, Tetraethylammonium bicarbonate (TEAB), reaction volumes including 0.4 mL, 0.5 mL, base to precursor ratios of 4-20, and temperatures of 120 °C, 150 °C.

Ligase Expression

^{W371}LpIA was cloned into a PQE-2, ampicillin-resistant bacterial vector, which was then transformed into BL21 bacterial cells. The plasmid was purified and characterized to verify it contained the correct ^{W371}LpIA sequence. 10 mL overnight cultures of BL21 cells with the expression vector were started in LB-broth containing ampicillin. Each 10 mL starter culture was then added to 1 L LB media with ampicillin and shaken at 200 rpm at 37°C. OD was monitored and upon OD₆₀₀=0.6, isopropyl β-D-1-thiogalactopyranoside was added to induce ^{W371}LpIA expression. Upon initiation of induction, cells were shaken at 200 rpm at 30 °C for 4 hours. Cell-

containing media was then taken and centrifuged to pellet cells, which were then resuspended in lysis buffer. Resuspended cells were then sonicated and the resultant cell lysate centrifuged. The supernatant was decanted and incubated with Nickel-NTA beads overnight while rotating at 4°C. Beads were then washed with 20 mM imidazole and then eluted with 500 mM imidazole and at least ten 1.5 mL fractions were collected. Fractions were analyzed via SDS-gel and fractions containing bands at ~39 kDa, the molecular weight of ^{W37I}LpIA, were carried forward. Fractions containing ^{W37I}LpIA correlating bands were buffer exchanged into PBS, pooled, and purified via SEC. Purified product was then verified for purity using FPLC, SDS-gel, and anti-His-tag staining western-blot (Figure 1). Yield was verified by BCA assay to determine protein concentration.

In-Vitro Kinetics

The ^{W37I}LpIA enzyme (500 nM) was incubated with LAP peptide (750 μM), ATP (300 mM), and Mg(OAc)₂ (2 mM) with various concentrations of non-radioactive reference standard FPOA (10, 50, 100, 250, and 500 μM; n =3 for each concentration) at 30 °C. At 1, 3, 5, 10, 15, and 30 minute time-points, aliquots were taken and quenched with an EDTA solution to a final concentration of 50 mM. The conversion of LAP to the ligated LAP-FPOA species was measured via HPLC and peak intensities were converted to molar concentrations using a standard curve of LAP-FPOA. Molar concentration was calculated over time for each FPOA concentration to calculate molar velocities that were then used to plot Michaelis-Menten curves and derive the kinetic values K_M , k_{cat} , and V_{max} .

2.6 References

- (1) Cho, S. Y.; Huff, D. T.; Jeraj, R.; Albertini, M. R. FDG PET/CT for Assessment of Immune Therapy: Opportunities and Understanding Pitfalls. *Seminars in Nuclear Medicine* **2020**, *50* (6), 518–531. <https://doi.org/10.1053/j.semnuclmed.2020.06.001>.
- (2) Alauddin, M. M.; Khawli, L. A. Advances in Immuno-PET for the Detection of Cancer and Assessment of Response to Therapy. *Current Medicinal Chemistry* **2021**, *28* (4), 647–672. <https://doi.org/10.2174/0929867327666200128102958>.
- (3) Ahn G-One; Tseng Diane; Liao Cho-Hwa; Dorie Mary Jo; Czechowicz Agnieszka; Brown J. Martin. Inhibition of Mac-1 (CD11b/CD18) Enhances Tumor Response to Radiation by Reducing Myeloid Cell Recruitment. *Proceedings of the National Academy of Sciences* **2010**, *107* (18), 8363–8368. <https://doi.org/10.1073/pnas.0911378107>.
- (4) Börjesson, P. K. E.; Jauw, Y. W. S.; de Bree, R.; Roos, J. C.; Castelijns, J. A.; Leemans, C. R.; van Dongen, G. A. M. S.; Boellaard, R. Radiation Dosimetry of ⁸⁹Zr-Labeled Chimeric Monoclonal Antibody U36 as Used for Immuno-PET in Head and Neck Cancer Patients. *J Nucl Med* **2009**, *50* (11), 1828. <https://doi.org/10.2967/jnumed.109.065862>.
- (5) Lammering, G.; De Ruyscher, D.; van Baardwijk, A.; Baumert, B. G.; Borger, J.; Lutgens, L.; van den Ende, P.; Öllers, M.; Lambin, P. The Use of FDG-PET to Target Tumors by Radiotherapy. *Strahlentherapie und Onkologie* **2010**, *186* (9), 471–481. <https://doi.org/10.1007/s00066-010-2150-1>.
- (6) Miao, Z.; Ren, G.; Liu, H.; Qi, S.; Wu, S.; Cheng, Z. PET of EGFR Expression with an ¹⁸F-Labeled Affibody Molecule. *J Nucl Med* **2012**, *53* (7), 1110. <https://doi.org/10.2967/jnumed.111.100842>.
- (7) Xavier, C.; Blykers, A.; Vaneycken, I.; D’Huyvetter, M.; Heemskerk, J.; Lahoutte, T.; Devoogdt, N.; Caveliers, V. ¹⁸F-Nanobody for PET Imaging of HER2 Overexpressing Tumors. *Nuclear Medicine and Biology* **2016**, *43* (4), 247–252. <https://doi.org/10.1016/j.nucmedbio.2016.01.002>.

- (8) Cai, W.; Olafsen, T.; Zhang, X.; Cao, Q.; Gambhir, S. S.; Williams, L. E.; Wu, A. M.; Chen, X. PET Imaging of Colorectal Cancer in Xenograft-Bearing Mice by Use of an ^{18}F -Labeled T84.66 Anti-Carcinoembryonic Antigen Diabody. *J Nucl Med* **2007**, *48* (2), 304.
- (9) Lütje, S.; Franssen, G. M.; Sharkey, R. M.; Laverman, P.; Rossi, E. A.; Goldenberg, D. M.; Oyen, W. J. G.; Boerman, O. C.; McBride, W. J. Anti-CEA Antibody Fragments Labeled with [^{18}F]AIF for PET Imaging of CEA-Expressing Tumors. *Bioconjugate Chem.* **2014**, *25* (2), 335–341. <https://doi.org/10.1021/bc4004926>.
- (10) Morris, O.; Fairclough, M.; Grigg, J.; Prenant, C.; McMahon, A. A Review of Approaches to ^{18}F Radiolabelling Affinity Peptides and Proteins. *Journal of Labelled Compounds and Radiopharmaceuticals* **2019**, *62* (1), 4–23. <https://doi.org/10.1002/jlcr.3634>.
- (11) Yu, S. Review of F-FDG Synthesis and Quality Control. *Biomed Imaging Interv J* **2006**, *2* (4), e57–e57. <https://doi.org/10.2349/bij.2.4.e57>.
- (12) Liu, Z.; Li, Y.; Lozada, J.; Schaffer, P.; Adam, M. J.; Ruth, T. J.; Perrin, D. M. Stoichiometric Leverage: Rapid ^{18}F -aryltrifluoroborate Radiosynthesis at High Specific Activity for Click Conjugation. *Angewandte Chemie* **2013**, *125* (8), 2359–2363.
- (13) Page, M. J.; Lourenço, A. L.; David, T.; LeBeau, A. M.; Cattaruzza, F.; Castro, H. C.; VanBrocklin, H. F.; Coughlin, S. R.; Craik, C. S. Non-Invasive Imaging and Cellular Tracking of Pulmonary Emboli by near-Infrared Fluorescence and Positron-Emission Tomography. *Nature Communications* **2015**, *6* (1), 8448. <https://doi.org/10.1038/ncomms9448>.
- (14) Drake, C.; Blecha, J.; Sevillano, N.; Craik, C.; VanBrocklin, H.; Moore, M. **Enzymatic Radiofluorination of Biomolecules: Development and Automation of Second Generation Prosthetic on ELIXYS Radiosynthesizer**. *J Nucl Med* **2017**, *58* (supplement 1), 1.
- (15) Kaptj, J.; Kniess, T.; Wuest, F.; Mercer, J. R. Radiolabeling of Phosphatidylserine-Binding Peptides with Prosthetic Groups N-[6-(4-[^{18}F] Fluorobenzylidene)

- Aminoxyhexyl] Maleimide ([¹⁸F] FBAM) and N-Succinimidyl-4-[¹⁸F] Fluorobenzoate ([¹⁸F] SFB). *Applied Radiation and Isotopes* **2011**, *69* (9), 1218–1225.
- (16) Beckford-Vera, D. R.; Gonzalez-Junca, A.; Janneck, J. S.; Huynh, T. L.; Blecha, J. E.; Seo, Y.; Li, X.; VanBrocklin, H. F.; Franc, B. L. PET/CT Imaging of Human TNF α Using [⁸⁹Zr]Certolizumab Pegol in a Transgenic Preclinical Model of Rheumatoid Arthritis. *Mol Imaging Biol* **2019**, *22* (1), 105–114.
- (17) Roscales, S.; Kniess, T. Access to ¹⁸F-Labelled Isoxazoles by Ruthenium-Promoted 1,3-Dipolar Cycloaddition of 4-[¹⁸F]Fluoro-N-Hydroxybenzimidoyl Chloride with Alkynes. *Journal of Labelled Compounds and Radiopharmaceuticals* **2019**, *62* (8), 393–403. <https://doi.org/10.1002/jlcr.3708>.
- (18) Li, Z.; Cai, H.; Hassink, M.; Blackman, M. L.; Brown, R. C.; Conti, P. S.; Fox, J. M. Tetrazine–Trans-Cyclooctene Ligation for the Rapid Construction of ¹⁸F Labeled Probes. *Chemical Communications* **2010**, *46* (42), 8043–8045.
- (19) Bernard-Gauthier, V.; Bailey, J. J.; Liu, Z.; Wängler, B.; Wängler, C.; Jurkschat, K.; Perrin, D. M.; Schirmacher, R. From Unorthodox to Established: The Current Status of ¹⁸F-Trifluoroborate-and ¹⁸F-SiFA-Based Radiopharmaceuticals in PET Nuclear Imaging. *Bioconjugate chemistry* **2016**, *27* (2), 267–279.
- (20) Yan, X.; Niu, G.; Wang, Z.; Yang, X.; Kiesewetter, D. O.; Jacobson, O.; Shen, B.; Chen, X. Al [¹⁸F] NOTA-T140 Peptide for Noninvasive Visualization of CXCR4 Expression. *Molecular imaging and biology* **2016**, *18* (1), 135–142.
- (21) Martarello, L.; McConathy, J.; Camp, V. M.; Malveaux, E. J.; Simpson, N. E.; Simpson, C. P.; Olson, J. J.; Bowers, G. D.; Goodman, M. M. Synthesis of Syn- and Anti-1-Amino-3-[¹⁸F]Fluoromethyl-Cyclobutane-1-Carboxylic Acid (FMACBC), Potential PET Ligands for Tumor Detection. *J. Med. Chem.* **2002**, *45* (11), 2250–2259. <https://doi.org/10.1021/jm010242p>.
- (22) Liu, W.; Huang, X.; Placzek, M. S.; Krska, S. W.; McQuade, P.; Hooker, J. M.; Groves, J.

- T. Site-Selective ^{18}F Fluorination of Unactivated C–H Bonds Mediated by a Manganese Porphyrin. *Chem. Sci.* **2018**, *9* (5), 1168–1172. <https://doi.org/10.1039/C7SC04545J>.
- (23) Drake, C. R.; Sevillano, N.; Truillet, C.; Craik, C. S.; VanBrocklin, H. F.; Evans, M. J. Site-Specific Radiofluorination of Biomolecules with 8- ^{18}F -Fluorooctanoic Acid Catalyzed by Lipoic Acid Ligase. *ACS Chem Biol* **2016**, *11* (6), 1587–1594. <https://doi.org/10.1021/acscchembio.6b00172>.
- (24) Pretze, M.; Wuest, F.; Peppel, T.; Köckerling, M.; Mamat, C. The Traceless Staudinger Ligation with Fluorine-18: A Novel and Versatile Labeling Technique for the Synthesis of PET-Radiotracers. *Tetrahedron Letters* **2010**, *51* (49), 6410–6414. <https://doi.org/10.1016/j.tetlet.2010.09.134>.
- (25) Drake, C. R.; Evans, M. J.; VanBrocklin, H. F. Enzymatically Catalyzed Radiofluorination of Biomolecules. In *Bioconjugation: Methods and Protocols*; Massa, S., Devoogdt, N., Eds.; Springer New York: New York, NY, **2019**; pp 191–205. https://doi.org/10.1007/978-1-4939-9654-4_13.
- (26) Arimitsu, K.; Kimura, H.; Arai, Y.; Mochizuki, K.; Taki, M. ^{18}F -Containing Positron Emission Tomography Probe Conjugation Methodology for Biologics as Specific Binders for Tumors. *Current Topics in Medicinal Chemistry* **2016**, *16* (24), 2703–2724.
- (27) Bernard-Gauthier, V.; Lepage, M. L.; Waengler, B.; Bailey, J. J.; Liang, S. H.; Perrin, D. M.; Vasdev, N.; Schirmacher, R. Recent Advances in ^{18}F Radiochemistry: A Focus on B- ^{18}F , Si- ^{18}F , Al- ^{18}F , and C- ^{18}F Radiofluorination via Spirocyclic Iodonium Ylides. *J Nucl Med* **2018**, *59* (4), 568. <https://doi.org/10.2967/jnumed.117.197095>.
- (28) Mossine, A. V.; Brooks, A. F.; Makaravage, K. J.; Miller, J. M.; Ichiishi, N.; Sanford, M. S.; Scott, P. J. H. Synthesis of ^{18}F Arenes via the Copper-Mediated ^{18}F Fluorination of Boronic Acids. *Org. Lett.* **2015**, *17* (23), 5780–5783. <https://doi.org/10.1021/acs.orglett.5b02875>.
- (29) Mossine, A. V.; Brooks, A. F.; Bernard-Gauthier, V.; Bailey, J. J.; Ichiishi, N.;

- Schirrmacher, R.; Sanford, M. S.; Scott, P. J. H. Automated Synthesis of PET Radiotracers by Copper-Mediated (18) F-Fluorination of Organoborons: Importance of the Order of Addition and Competing Protodeborylation. *J Labelled Comp Radiopharm* **2018**, *61* (3), 228–236. <https://doi.org/10.1002/jlcr.3583>.
- (30) Rotstein, B. H.; Stephenson, N. A.; Vasdev, N.; Liang, S. H. Spirocyclic Hypervalent Iodine(III)-Mediated Radiofluorination of Non-Activated and Hindered Aromatics. *Nature Communications* **2014**, *5* (1), 4365. <https://doi.org/10.1038/ncomms5365>.
- (31) Fernández-Suárez, M.; Baruah, H.; Martínez-Hernández, L.; Xie, K. T.; Baskin, J. M.; Bertozzi, C. R.; Ting, A. Y. Redirecting Lipoic Acid Ligase for Cell Surface Protein Labeling with Small-Molecule Probes. *Nat Biotechnol* **2007**, *25* (12), 1483–1487. <https://doi.org/10.1038/nbt1355>.
- (32) Lazari, M.; Collins, J.; Shen, B.; Farhoud, M.; Yeh, D.; Maraglia, B.; Chin, F. T.; Nathanson, D. A.; Moore, M.; van Dam, R. M. Fully Automated Production of Diverse 18F-Labeled PET Tracers on the ELIXYS Multireactor Radiosynthesizer without Hardware Modification. *J Nucl Med Technol* **2014**, *42* (3), 203–210. <https://doi.org/10.2967/jnmt.114.140392>.

CHAPTER 3

SCREENING FOR NOVEL SARS-COV-2 MAJOR PROTEASE NON-COVALENT AND COVALENT INHIBITORS

SCREENING FOR NOVEL SARS-COV-2 MAJOR PROTEASE NON-COVALENT AND COVALENT INHIBITORS

3.1 Abstract

Antiviral therapeutics to treat SARS-CoV-2 are much desired for the on-going pandemic. A well-precedented viral enzyme is the main protease (MPro), which is now targeted by an approved drug and by several investigational drugs. Retaining liabilities, and facing viral resistance, there remains a call for new chemical scaffolds against MPro. We virtually docked 1.2 billion non-covalent and a new library of 6.5 million electrophilic molecules against the enzyme structure. From these, 148 inhibitors were found from 19 different series, the most potent having an IC_{50} of 29 μ M and 20 μ M, respectively. Several series were optimized, in several cases resulting in inhibitors active in the low μ M range. Subsequent crystallography confirmed the docking predicted binding modes and may template further optimization of compounds that have been shown to be antiviral. Together, these compounds reveal new chemotypes to aid in further discovery of MPro inhibitors for SARS-CoV-2 and other future coronaviruses.

3.2 Introduction

SARS-CoV-2 encodes two cysteine proteases that have essential roles in hydrolyzing viral polyproteins into nonstructural proteins, enabling virus replication. The main protease (MPro, or 3CL protease) cleaves 11 different sites in viral polyproteins and is considered to be a particularly promising antiviral drug target. While MPro is highly conserved across other coronaviruses such as SARS-CoV-1 and MERS, it has no close human homolog. This makes it attractive for potential pan-coronavirus targeting, and for selective toxicity.

The therapeutic potential of MPro inhibitors was substantiated by the approval, in December 2021, of Paxlovid. Paxlovid combines nirmatrelvir, which covalently inhibits MPro, with ritonavir, which slows nirmatrelvir's metabolism.¹ Nirmatrelvir was developed from PF-00835231, an inhibitor of the SARS-CoV-1 MPro in response to the 2002 SARS outbreak. Meanwhile, other potent MPro inhibitors are advancing through the drug development pipeline. Among them is the orally active MPro inhibitor S-217622², which has entered clinical trials. Other inhibitors show much promise³⁻⁷, including a non-covalent MPro inhibitor from the international Covid-19 Moonshot consortium that may be characterized as an advanced clinical candidate, and more experimental molecules that are relatively potent but have not proceeded far from hit to lead⁸.

Notwithstanding these successes, both the resistance that may be expected to emerge, and the liabilities of the established inhibitors support the discovery of new scaffolds. Accordingly, we targeted the structure of MPro for large library docking, seeking to find new starting points for lead discovery. Docking a library of over 1.2 billion “tangible” (make-on-demand) lead-like molecules and 6.5 million tangible electrophiles led to MPro inhibitors in over 50 scaffolds, with affinities ranging from the low mM to 200 mM. Crystal structures for eight of the new inhibitors bound to MPro largely confirmed the docking predictions, while cell-based antiviral activity for two of the new inhibitors supports their further optimization

3.3 Results

MPro is the fifth nonstructural protein (Nsp5) encoded by SARS-CoV-2 and is a homodimeric cysteine protease with a catalytic diad of Cysteine 145 and Histidine 41. MPro has a P1 primary specificity determinant of glutamine and also has a preference for aliphatic residues in the P4 and P2 positions, while alanine and serine in the P1' position. As with many other cysteine proteases, the catalytic Cys145 is primed by proton transfer to His41, such that acylation then occurs where Cys145 nucleophilically attacks the peptide substrate's carbonyl carbon and the scissile bond is broken, releasing the prime side peptide chain with an amine terminus. The thioester bond is then hydrolyzed by an attacking water to reveal the nonprime side peptide product with a carboxylic acid terminus, regenerating the protonated active site cysteine, and thus free enzyme is able to repeatedly turnover.

Crucial to inhibitor testing was the design and synthesis of an optimal substrate⁹ (**Fig. 3.1**). The endogenous Nsp substrates of MPro were compiled and a consensus sequence was observed that closely matched the individual sequence of the Nsp7 cleavage site (ATLQAIAS) (**Fig. 3.1c**). This sequence was flanked with an N-terminal Lysine-MCA fluorophore and a C-terminal DNP-quencher. Noting the preference for nonpolar residues at multiple sites, we were concerned that this substrate would have low solubility. Accordingly, two D-Arginines were coupled N-terminal to the Lysine-MCA to increase solubility (**Fig. 3.1a**). This Nsp7-like substrate yielded a favorable K_m of 12 M and a k_{cat}/K_m of 93,000 M⁻¹ s⁻¹, 3.5-fold better than that of the commonly used commercial substrate (Nsp4: AVLQSGFR; $k_{cat}/K_m = 26,500$ M⁻¹ s⁻¹)¹⁰; this substrate was used in all enzyme inhibition assays (**Fig. 3.1b**). The more efficient Nsp7-like substrate described here is readily synthesized and provides the field with an optimized MPro substrate.

In early proof-of-concept testing, we observed intolerance of MPro activity to high concentrations of DMSO, which can occur owing to delivery of substrate and candidate inhibitors from DMSO stocks (the sensitivity to DMSO may reflect oxidation of the catalytic

cysteine). The increased solubility of the D-Arginine-modified substrate reduced this DMSO effect by reducing the amount of organic solvent necessary to deliver the substrate. In addition, we found that ethanol and acetonitrile were more tolerated by the enzyme, though these solvents had issues with volatility (**Fig. 3.S2a**). These observations highlight the importance of controlling and minimizing compound solvent concentrations for MPro activity assays and provide other solvents when DMSO is not suitable for in-vitro biochemical assays. It was also noted that the presence of detergent was crucial for retaining Mpro activity in our *in-vitro* assays. Removing the 0.05% Tween-20 resulted in no observed substrate cleavage. Activity was then recovered by increasing addition of bovine serum albumin (BSA), highlighting the need of detergent or enzyme stabilizing additives (**Fig. 3.S2b**).

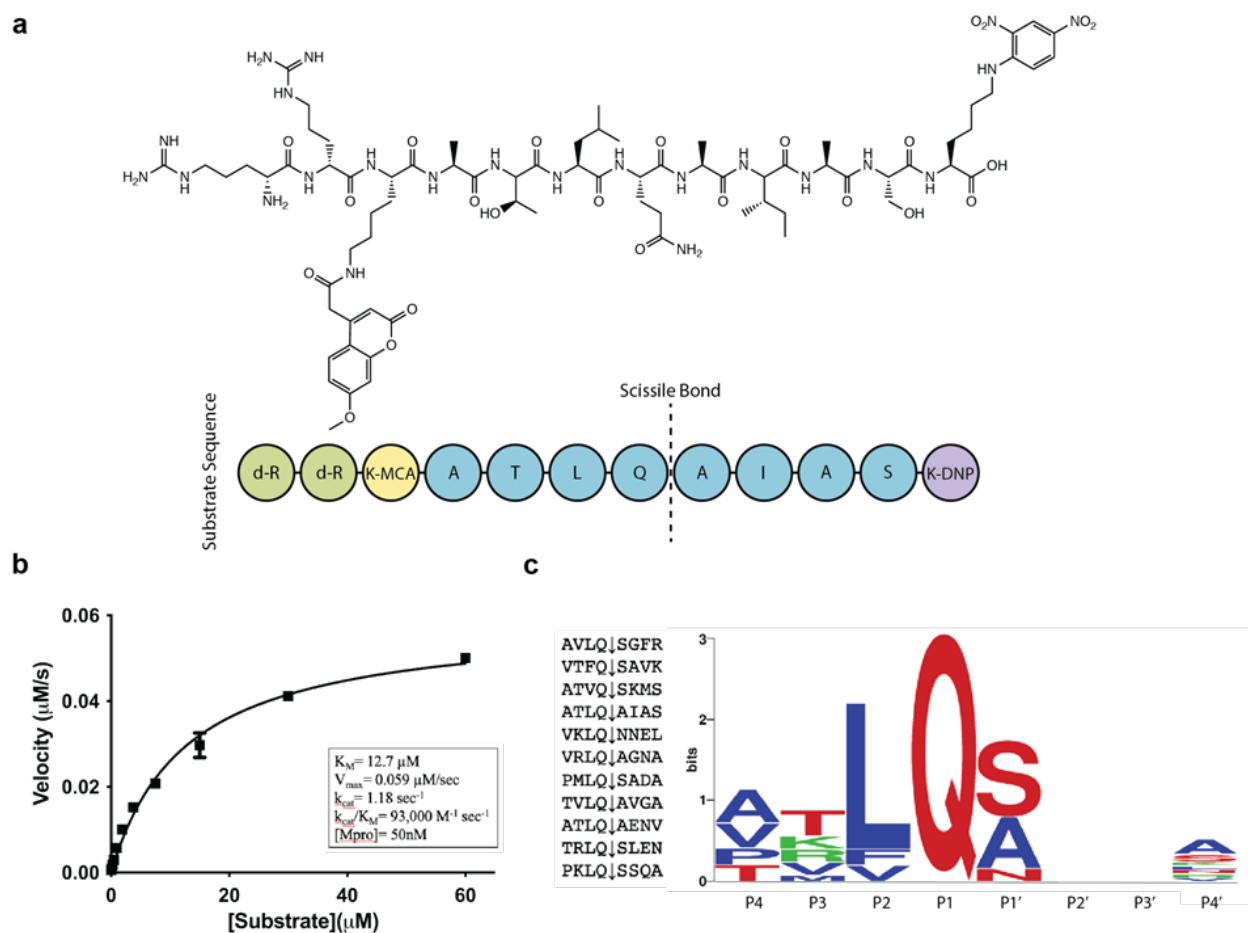


Figure 3.1: Substrate design for assay development. (a) The chemical structure of the optimized NSP7 substrate. (Top) A schematic of the substrate sequence highlights the role of each residue (Bottom). The substrate contains the P4-P4' NSP7 extended substrate sequence (Blue), the fluorophore (Yellow), the fluorescent quencher (Purple), and the residues for increasing solubility (Green). (b) The Michaelis-Menten kinetics for the NSP7 substrate with MPro yield parameters indicative of an optimized, efficient substrate. (c) A list of the viral polypeptide NSP sequences (P4-P4') that are cleaved by MPro. (Left) The sequenceLOGO highlighting the substrate specificity of MPro, yielding a P4-P4' consensus sequence:ATLQ(S/A)XXA.

Seeking new inhibitors, we began with a SARS-CoV-2 MPro crystal structure in complex with a covalent alpha-ketoamide inhibitor (PDB 6Y2G).¹¹ To define hot-spots for ligand docking in the active site, we generated a complex of SARS-CoV-2 MPro bound to a non-covalent SARS-CoV MPro inhibitor (PubChem: SID87915542) (non-covalent inhibitor complex structures were at that time unavailable). The crystal structure of the non-covalently ligated SARS-CoV

MPro (PDB 3V3M)¹² was structurally aligned onto the SARS-CoV-2 structure, the atomic coordinates of the alpha-ketoamide inhibitor were replaced with those of SID87915542 and the complex was energetically minimized. After calibration of the docking parameters¹³, approximately 225 million neutral molecules, mainly from the lead-like subset of the ZINC15 library¹⁴ (molecular weight (MWT) ranging from 250-350 amu and calculated (c)logP <4.5) were docked against MPro. Another 110 million molecules with 350 < MWT > 500 were docked in a separate screen. Docked molecules were filtered for intramolecular strain¹⁵ and selected for their ability to hydrogen bond with Gly143, His163, or Glu166, and make favorable non-polar contacts with Met49 and Asp187. Ultimately, 120 molecules were purchased from the lead-like docking screen, 105 (87.5%) of which were successfully synthesized. Another 89 molecules were synthesized from the higher molecular weight molecules.

Initially, 175 compounds were experimentally tested against MPro at a single concentration of 100 M using the fluorescence-based substrate cleavage assay. 19 molecules (11%) showed >30% inhibition of enzyme activity. Subsequently, we determined full dose response curves for 14 molecules, with IC₅₀ values ranging from 97 to 300 M (**Table 3.1, Table 3.S1, Fig. 3.S2.1, Fig. 3.S2.2**). As mentioned above, DMSO was observed to lower enzyme activity, consequently the actives were re-tested against MPro from 30 mM acetonitrile (ACN) or ethanol (EtOH) stocks. Ten compounds showed clear dose-response with IC₅₀ values ranging from 30 to 325 M. Of note, although not explicitly targeted with this docking campaign, three initial docking hits (ZINC338540162: IC₅₀[ACN] = 30 M, ZINC271072260: IC₅₀[ACN] = 143 M and ZINC795258204: IC₅₀[DMSO] = 177 M) may inhibit MPro covalently as they contain warheads (nitrile or aldehyde) known to attack the catalytic Cys145 .

Table 3.1: Hits from the first non-covalent docking screen.

Chemical Structure	Compound ID	IC50 [μ M] (solvent)	Chemical Structure	Compound ID	IC50 [μ M] (solvent)
	ZINC346371112	214 (DMSO) 98 (ACN)		ZINC274326055	300 (DMSO)
	ZINC894230117	225 (DMSO) 164 (ACN)		ZINC813360541	275 (DMSO) 94 (ACN)
	ZINC1339780091	224 (DMSO) 121 (ACN)		ZINC553840273	200 (DMSO) 88 (ACN)
	ZINC433294115	97 (DMSO)		ZINC336912805	250 (DMSO) 177 (ACN)
	ZINC618071006	290 (DMSO) 200 (EtOH)		ZINC271072260	115 (DMSO) 143 (ACN)
	ZINC301553312	122 (DMSO) 63 (EtOH)		ZINC338540162	281 (DMSO) <30 (ACN)
	ZINC915668084	291 (DMSO) 184 (ACN)		ZINC795258204	177 (DMSO) 325 (ACN)

We focused on four initial hits (ZINC346371112: IC50[ACN] = 98 M, ZINC301553312: IC50[EtOH] = 63 M, ZINC813360541: IC50[ACN] = 90 M and ZINC553840273: IC50[ACN] = 88 M) for structure-based optimization. We used the SmallWorld search engine (NextMove Software, Cambridge UK)¹⁶ to identify purchasable analogs of these inhibitors within a 12 billion compound version of the REAL library (<https://enamine.net/compound-collections/real-compounds/real-space-navigator>), docking each analog into the MPro structure to assess

complementarity. Between 10-20 analogs of each of the four inhibitors were selected for testing (**Fig. 3.2, Table 3.S1**).

Crystal structures of the non-covalent inhibitors. To investigate how the docked poses of the new inhibitor scaffolds corresponded to true binding modes, and to template future optimization, crystal structures of three of the optimized non-covalent inhibitors were determined. For the '0237 analog, SG-0001 (IC₅₀ = 55μM), the obtained crystal structure showed placement of the tetrahydrobenzoxazepine in the P2 subpocket (**Fig 3.2c**) as suggested in the docked pose of the parent compound (**Fig 3.2a**), while the isoquinoline group forms a hydrogen bond with His163 in the P1 subpocket. The crystal structure of MPro in complex with the '0541 analog '5548 superposed with high fidelity to the docking-predicted pose of this compound (**Fig. 3.2e**). Here, the compound's central hydantion scaffold hydrogen-bonds with the backbone amine of Glu166 and Gly143. The crystal structure of MPro in complex with '6137 confirms this interaction pattern and shows placement of the isoquinoline into the P1 subpocket as well as insertion of the hydrophobic (1-methyl)-tetraline into the P2 pocket.

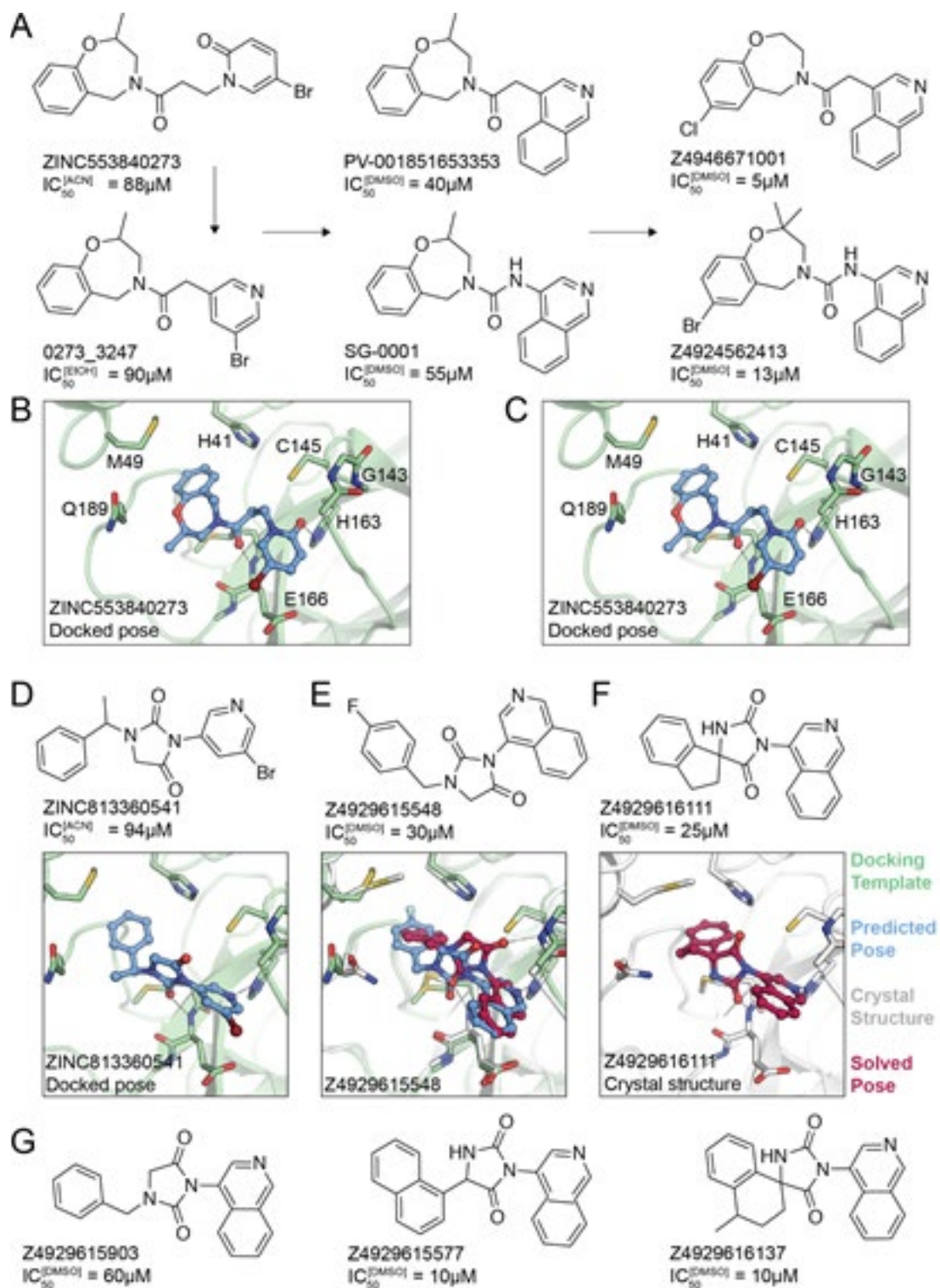


Figure 3.2.: Non-covalent compound optimization to low-μM potencies.

A second docking screen for non-covalent inhibitors of MPro. As several groups have identified potent inhibitors, several with scaffolds resembling our own, and have published an extraordinary amount of structure-activity-relationship (SAR) data, we thought to perform a second docking campaign. Here, we tried to incorporate insights emerging from our own results and those from other studies^{3,8} emphasizing the discovery novel chemotypes.

The new docking screen targeted the SARS-CoV-2 MPro crystal structure in complex with MAT-POS-b3e365b9-1 (MPro-x11612.pdb), a non-covalent ligand reported by the Moonshot consortium. Compared to the previous docking template (PDB 6Y2G), the MAT-POS-b3e365b9-1-bound site is slightly smaller, with the 2-turn alpha helix between Thr45 and Leu50, and the loop between Arg188 and Ala191 shifted inwards by roughly 2 Å, constricting the shape of the P2 sub-pocket. After calibration of docking parameters, ensuring the model prioritizes 15 previously reported MPro inhibitors against different decoy sets^{13,17}, 862 million neutral compounds with 18-29 non-hydrogen atoms from the Enamine REAL database were docked.

The high-ranking docked molecules were filtered for novel chemotypes by removing those with ECFP4-based Tanimoto coefficients (Tc) greater than 0.35 to 1,717 SARS-CoV-2 MPro inhibitors (Methods). Roughly 9,500 of these were graphically evaluated for favorable contacts, and 146 compounds were purchased from Enamine. Of these, 17 (12%) inhibited MPro with IC₅₀ values < 200 M (**Table 3.2**). To our knowledge, none of the new activities fell into scaffolds that have been previously reported for MPro. Compared to the first docking screen, several initial hits from the second screen showed slightly higher activity, such as Z3535317212, with an IC₅₀ value of 29 μM (estimated K_i of 15 μM). For '7212, the docked pose suggests hydrogen bonds between the compound's central dihydrouracil scaffold and Glu166 as well as Gly143, in addition to hydrogen bonds between the compound's pyridinol (**Fig. 3.S2.3**). Five docking hits (Z5420225795: IC₅₀ = 40 M, Z1669286714: IC₅₀ = 110 M, Z1355254448: IC₅₀ = 110 M, ZINC5420738300: IC₅₀ = 160 M, Z2195811405: IC₅₀ ~200 M) share a common ketoamide functional group predicted to form one hydrogen bond to Glu166,

however, we note that ketoamide might also inhibit MPro through covalent linkage to Cys145. Taken together, the actives from this campaign explored ten different scaffold classes with IC₅₀ values better than 150 μ M (estimated K_i values better than 75 μ M). These scaffolds represent new points of departure for MPro inhibitor discovery.

Table 3.2: Hits from the second non-covalent docking screen.

Chemical Structure	Compound ID	IC50 [μ M] (solvent)	Chemical Structure	Compound ID	IC50 [μ M] (solvent)
	Z3535317212	29		Z1425997900	110
	Z4124468376	33		Z3541227016	130
	Z3555684465	33		Z3382155230	140
	Z5420225795	40		Z5420738300	160
	Z1716270280	60		Z2195811405	200
	Z5420228488	60		Z4289708272	200
	Z3079159560	90		Z5385490967	200
	Z1669286714	110		Z4335534517	200
	Z1355254448	110			

A covalent docking screen targeting MPro Cys145. We aimed to target the catalytic Cys145 proximal to the binding site as the crystal ligand of PDB 6Y2G did with an α -ketoamide warhead in early crystal structures of MPro11. Three Cys-reactive covalent warheads, aldehydes, nitriles, and -ketoamides, were prioritized for covalent docking by covalent docking (DOCKoalent)¹⁸. Each chemical group was searched in the ZINC15/ZINC2014,16 1.4 billion databases. Dockable 3D molecules were built, specifically for covalent docking with DOCK 3.7/DOCKoalent (Methods). The molecules and their DOCKoalent files for the final 6.5 million molecules are available at <http://covalent2022.docking.org>.

We then virtually screened 3.6 million nitriles, 1.5 million aldehydes, and 1.4 million α -ketoamides, all newly built, against MPro (PDB 6Y2G)¹¹. The top-ranked molecules were filtered for torsional strain¹⁵, for favorable enzyme interactions, and clustered for chemical similarity using an ECFP4-based best first clustering algorithm. Remaining molecules were visually prioritized for favorable interactions with His41, Cys145, Gly143, Thr26, or Glu166. Ultimately, 35 aldehydes, 41 nitriles, and 21 -ketoamides were selected for synthesis, of which 27, 31, 16, respectively, were successfully synthesized and tested for activity against MPro. Those compounds with percent inhibition >33% at 100 μ M were tested in full concentration-dose-response.

Defining actives as molecules with IC₅₀s less than 200 μ M, the hit rate for covalent docking was 18% (13 actives/74 compounds tested); the most potent had an IC₅₀ of 20 μ M (**Fig. 3.3**). Eight others had IC₅₀ values 25 to 100 μ M. Initial nitriles and aldehyde docking hits had activities as low as 20 M in compound '5103, and 55 M in compound '3620, respectively. The ketoamide docking screens resulted in two actives of the same chemotype with weaker IC₅₀s of \sim 200 μ M.

The covalent inhibitors were diverse, docking to fill different enzyme subpockets (**Fig. 3.3, Fig. 3.S3**). In the P1' pocket, hydrophobic interactions were made by compounds '3620, '6345, '6792. Hydrogen bonding with His163 in the P1 pocket was made by '5103, '0431, '2961.

Several compounds, such as '0892 and '0292, fit into the P2 pocket, making non-polar interactions with Met49 and Phe181. Other compounds, like '5156, fit down the 'tunnel' of the binding site between the P1 and P2 pockets as in '5156, hydrogen-bonding to Glu166. Many compounds, such as '3620 and '6792, hydrogen-bonded with the peptide backbone atoms of Cys145, Ser144 and Gly143.

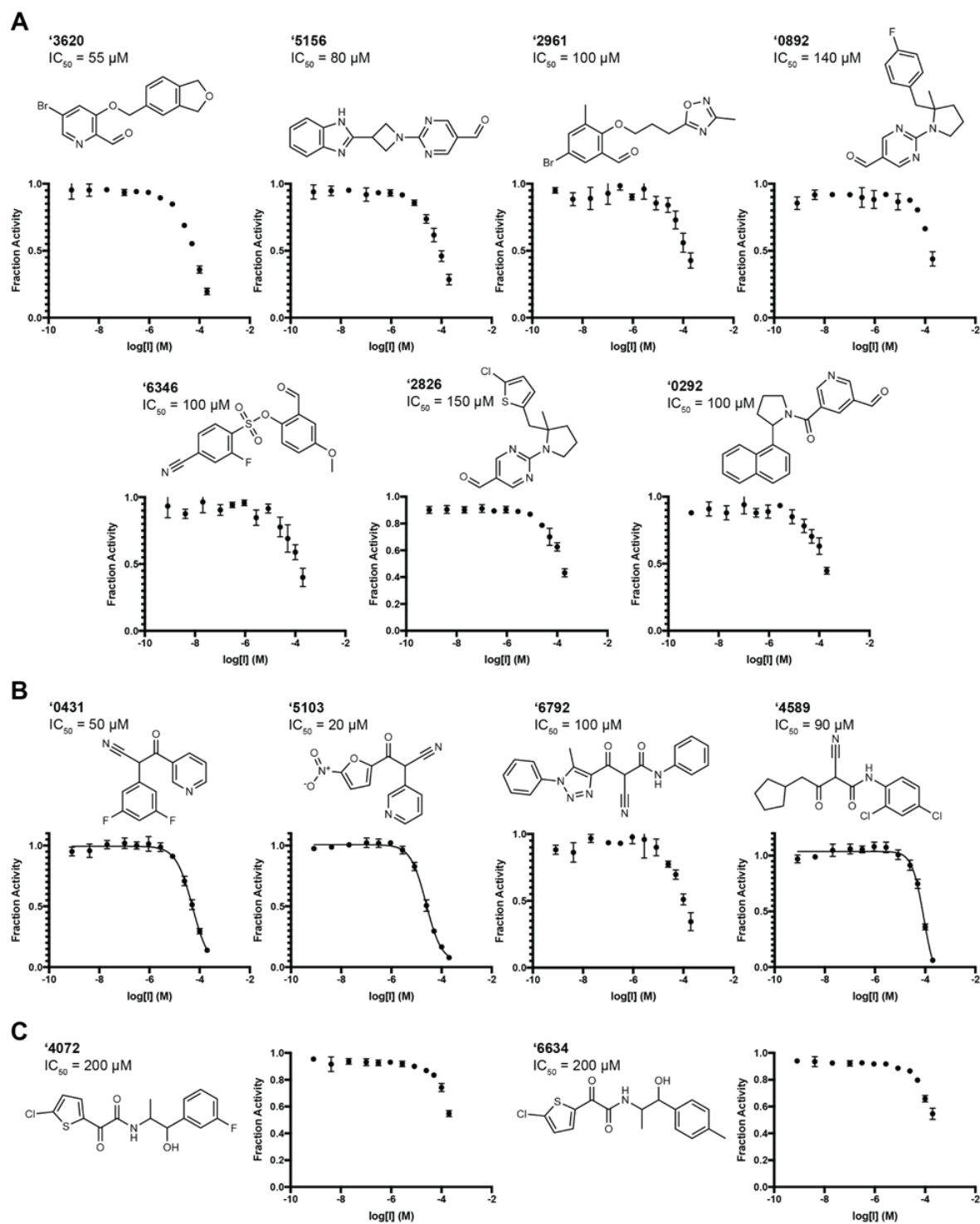


Figure 3.3: Covalent hits from 6.5 million virtual screen. Dose response curves for (a) aldehyde (b) nitrile and (c) ketoamide docking hits. IC₅₀ values shown. All measurements done in triplicate.

We sought to optimize several of the new covalent inhibitors, focusing on the 55 M aldehyde '3620 (Table S1). These analogs were identified through multiple strategies, including simply seeking readily available “make-on-demand” congeners that fit in the enzyme site, using SmallWorld and Arthor (NextMove Software, Cambridge, UK)¹⁶, or testing perturbations to what seemed to be key interactions. From these studies emerged 36 analogs with IC₅₀s better than '3620, the most potent of which had an IC₅₀ of 1 M ('7021). Other analogs ranging from 2 to 48 M had changes to different benzene substituents or bicyclic systems of '3620 (**Fig. 3.4, Table 3.S2**).

In its docked pose, the pyridine nitrogen of '7021 hydrogen bonds in the pocket (**Fig. 3.4c**). To test the importance of this interaction, the phenyl analog of the pyridine, compound '4218, was synthesized and tested. This molecule lost all measurable activity (IC₅₀ > 200 μM), consistent with the importance of the pyridine hydrogen bonds (**Fig. 3.4c**). Meanwhile, removing non-polar groups from the distal phenyl ring of '7021, as in analogs '9313 and '9112, increased IC₅₀ values to 22 M and 35 μM, respectively, indicating more hydrophobic bulk was preferred in the shallow subsite in which this substituted phenyl was docked.

Crystal structures of the covalent inhibitors. To investigate how the docked poses of the covalent inhibitors corresponded to true binding modes, and to template further optimization, crystal structures of five aldehyde inhibitors were determined: '7021 (IC₅₀ = 1 μM), analog_18/'9105 (IC₅₀ = 6 μM), '8252 (IC₅₀ = 6 μM), analog_6/'9121 (IC₅₀ = 12 μM), and '7356 (IC₅₀ = 26 μM) (**Fig. 3.4b, Fig. 3.4d, Fig. 3.S4**). The structures of these compounds recapitulated the docking predictions with high fidelity (**Fig. 3.4b**). Consistent with the docking, and with the results of the analogs, the pyridine nitrogen in each inhibitor hydrogen bonds with X (**Fig. 3.4c**), while the hydroxyl of what had been the aldehyde warhead hydrogen bonds in the oxyanion hole of the enzyme, and the ether-alkyl linker hydrogen bonds with His41. The hydrophobic groups on the distal aryl ring interact with residues in the P2 site (**Fig. 3.4d**).

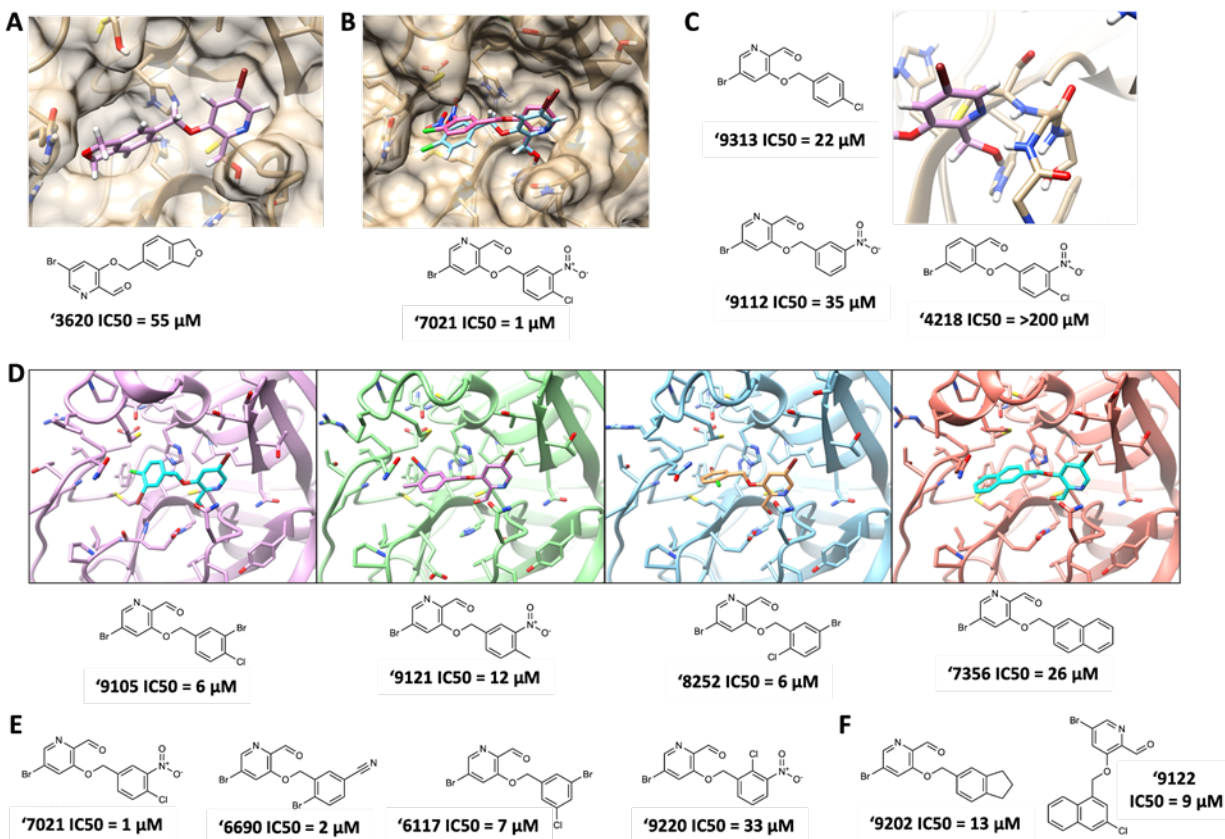


Figure 3.4: Compound optimization of aldehyde '3620. (a) Docked pose of docking hit '3620. (b) Crystal structure (pink carbons) and docked pose (blue carbons) comparison for analog '7021 (RMSD X Å; PDB X). (c) Hypothesis testing analogs of '7021 included removing the nitro in '9313 and the chlorine in '9112, both with weaker inhibition. Analog '4218 replaced the pyridine with a benzene eliminating inhibition. The pyridine of '7021 is shown with its docked pose (purple carbons) forming hydrogen bonds with backbone atoms of MPro (tan carbons). (d) Crystal structures of additional '3620 analogs. (e) Analogues with different benzene substituent orientations ('7021, '6690, '6117) inhibit MPro at similar potencies. Substituents oriented like '9220 were weaker inhibitors. (f) Examples of the most potent larger hydrophobic analogs of '3620. IC50 values shown. All measurements done in triplicate.

Lead inhibitors are antiviral with pan-coronaviral MPro inhibition. With the progression covalent and non-covalent series, we tested several compounds in an RT-qPCR viral infectivity assay in vero cells. Compounds '7021 and '7356 had antiviral IC50 values of 6.2 μ M and 19.5 μ M, respectively, reflecting their in vitro IC50 values of 1 M and 26 M, respectively (**Fig. 3.5a, Table 3.S3**). Encouragingly, the cell viability remained high for the two compounds. Meanwhile,

no measurable antiviral activity was observed for the covalent aldehyde '6690 (IC₅₀ = 2 μM), the covalent nitrile '5103 (IC₅₀ = 20 μM), and the non-covalent '6137 (IC₅₀ = 8 μM). What separates the antiviral actives from the inactives remains unclear. We also tested '7021 for its ability to inhibit MPros of other coronaviruses, SARS-CoV-1 and MERS. '7021 inhibited the SARS-CoV-1 MPro with an IC₅₀ of 8 μM, very similar to that of SARS-CoV-2 MPro IC₅₀ of 1 μM, however was a weaker inhibitor for the MERS MPro with an IC₅₀ of 50 μM (**Fig. 3.5b**, **Table 3.S4**).

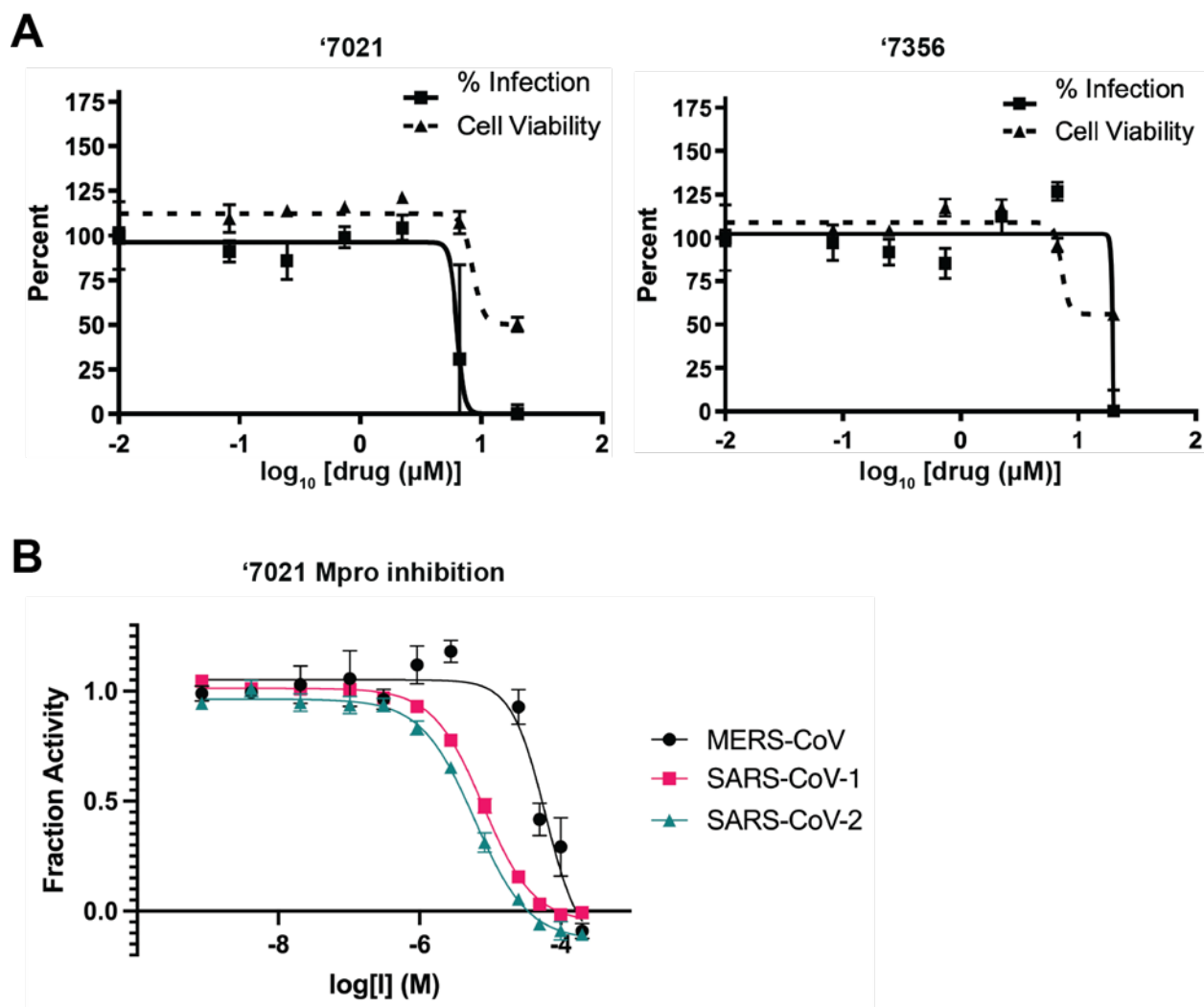


Figure 3.5: Antiviral activity and pan-coronaviral MPro inhibition by covalent analogs. (a) '7021 and '7356 inhibit SARS-CoV-2 infectivity with minimal impacts on cell viability. (b) '7021 also inhibits SARS-CoV-1 and MERS-CoV MPro. All measurements done in triplicate.

3.4 Discussion

From this study emerged 148 inhibitors with IC₅₀ values less than (better than) 150 µM covering 19 different scaffold classes. Of these, 15 inhibitors in 3 scaffolds inhibited the enzyme with IC₅₀ values less than 10 µM. We present an optimized MPro substrate for future inhibitor characterization. We note that to dock the electrophile library, we first had to create it, drawing on aldehydes, nitriles, and ketoamides in the expanding library of tangible molecules. This resulted in a library of over 6.5 million new electrophiles, which is openly available to the

community at <https://covalent2022.docking.org>. Crystal structures of eight of the new inhibitors closely corresponded to the docking predictions. Two of the new aldehyde inhibitors had antiviral activities close to those of their enzymatic IC50 values, suggesting that further optimization of this class for on-enzyme potency may presage antiviral activity.

While the strengths of this study were the identification of multiple new MPro inhibitor scaffolds, with subsequent crystal structures supporting the docking predictions, this work also revealed liabilities of docking screens. In contrast to campaigns against G protein coupled receptors¹⁹⁻²¹ and other integral membrane receptors²² which were in the 25 to 60% range as previously demonstrated. Moreover, the activities of the better MPro docking hits were in the 20 to 100 μ M range, not the low- to mid-nM range of the integral membrane proteins. Here, the MPro docking campaigns resemble those against other soluble proteins such as β -lactamase^{20,23} and the macrodomain of SARS-CoV-2²⁴, or even against allosteric sites in GPCRs^{25,26}. For physics-based scoring functions like that used in DOCK3.7, well-enclosed binding sites characterized by a key polar interaction are more amenable to ligand discovery than the more open, flatter sites such as those in MPro. This both reflects the physical characteristics of the site, and the sorts of molecules in our docking libraries, where chemical space coverage is best in the fragment and lead-like ranges and erodes among larger and more hydrophobic molecules better suited to sites like MPro's.

These caveats should not distract from the key observations of this study. Large library docking of both lead-like molecules and covalent electrophiles has revealed 19 scaffold families of MPro inhibitors, the best of which act in the low μ M range. Whereas neither hit rates nor affinities rose to levels seen against targets with well-defined binding sites, eight crystal structure of characteristic lead molecules confirmed the docking poses, when the docking was right it was right for the right reasons. These structures may template the further optimization of these new MPro inhibitors, several of which show initial antiviral activity against the virus.

3.5 Methods

Non-covalent molecular docking

The protein template was modeled based on the crystal structure of the MPro dimer in complex with a covalent alpha-ketoamide inhibitor (6y2g.pdb). All water molecules except for HOH 585 and HOH 602, which are located at the dimeric interface, were deleted. The binding pocket of the crystal structure's chain A was selected for docking. The alpha-ketoamide inhibitor was replaced by the non-covalent SARS-CoV inhibitor SID87915542. Here, the SID87915542-bound MPro crystal structure (3v3m.pdb) was aligned onto the SARS-CoV-2 MPro crystal structure in order to project SID87915542 into the SARS-CoV-2 MPro binding site. Next, the modeled protein-ligand complex and selected water molecules were prepared for docking with the protein prepwizad protocol of Maestro (Schrödinger v. 2019-3). Protons were added with Epik and protonation states were optimized with PropKa at pH 7. The C-terminus (Ser301) of each protein monomer structure was capped with N-methyl groups while the N-termini (Ser1) were positively charged. Subsequently, the modeled complex was energetically minimized using the OPLS3e force field. To better accommodate the modeled non-covalent ligand SID87915542, the CE atom of Met49 was displaced by 1.7Å from its initial position in the covalently ligated crystal structure (6y2g.pdb).

Computational docking was performed using DOCK3.7. Precomputed scoring grids for efficient quantification of van der Waals interaction between MPro and docked molecules were generated with CHEMGRID. Using the AMBER united-atom partial charges, electrostatic potentials within the binding pocket were computed following the numerical solution of the Poisson-Boltzmann equation with QNIFFT. The partial charges of the hydrogen at the epsilon nitrogen of His163, as well as the hydrogen atoms of the backbone amines of Gly143 and Glu166 were increased by 0.4 elementary charge units (e). In turn, the partial charges of oxygen atoms of the corresponding backbone carbonyl groups were decreased by 0.4e to maintain the initial net charge of each residue. The low dielectric protein environment was extended by 1.2Å

from the protein surface [cite]. Similarly, the low dielectric boundary was extended by 0.7Å from the protein surface for the calculation of ligand desolvation scoring grids with Solvmap. The atomic coordinates of SID87915542 (3v3m.pdb), the alpha-ketamide inhibitor of the initial crystal structure (6y2g.pdb), BDBM512845 (4mds.pdb) as well as fragment hits MAT-POS-7dfc56d9-1 (MPro-x0161) and AAR-POS-d2a4d1df-5 (MPro-x0305) obtained from the Covid-19 Moonshot screening efforts were used to generate 80 matching spheres for ligand placement in the docking calculations.

The obtained docking parameters were evaluated based on their ability to prioritize 34 previously reported ligands of SARS-CoV MPro obtained from the ChEMBL database [cite], against a background of 1,805 property matched decoys generated with the DUDE-Z approach [cite]. In addition, an 'Extrema' set [cite] of 194,921 molecules, including compounds with net-charges ranging from -2 to +2, was screened against the docking model in order to assess the parameters' ability to prioritize neutral molecules.

Using the ZINC15 database, 225,327,212 neutral molecules mainly from the lead-like chemical space, i.e. molecular weight (MWT) between 250 and 350 amu and calculated (c)logP < 4.5, from the make-on-demand compound libraries from Enamine and WuXi, were screened. Thereby, 219,305,079 molecules were successfully scored with each molecule sampling on average 3,588 orientations and 425 conformations which resulted in the evaluation of approximately 148 trillion complexes in roughly 70 hours on a 1,000-core computer cluster. In addition, 110,898,461 molecules with 350 < MWT < 500 and clogP < 4.5 from ZINC15 were screened in a separate docking campaign. 107,486,710 compounds were successfully scored, each exploring on average 4,175 orientations and 540 conformations within the binding pocket. Nearly 90 trillion complexes were scored in roughly 45 hours using a 1,000-core cluster.

From each docking screen, the predicted binding poses of the 500,000 top-ranked molecules were analyzed for internal molecular strain using the approach described in Shuo et al. [cite]. Molecules that passed the strain criteria (total strain <6.5 TEU; maximum single torsion

<1.8 TEU [cite]), were judged by their ability to form hydrogen bonds with Gly143, His163 (P1 subpocket) or Glu166 and proximity to residues forming the P2 subpocket such as Met49 or Asp187.

Finally, 120 compounds, selected from the lead-like docking screen, were ordered from Enamine, of which 105 were successfully synthesized (87.5%) in addition to 100 molecules of larger MWT that were ordered from the second docking screen, 89 of which were successfully synthesized by Enamine.

A second docking campaign for non-covalent inhibitors was performed against the crystal structure of MPro in complex with MAT-POS-b3e365b9-1 (MPro-x11612) from the Covid-19 Moonshot consortium. All water molecules except HOH6 and HOH300 were removed and the protein-ligand complex structure was prepared for docking following the protein prepwizard protocol of Maestro (Schrödinger v. 2019-3) as described above.

As in the previous docking campaign, the partial charges of the hydrogen atoms at the epsilon nitrogen of His163 and the backbone amine of Glu166 were increased by 0.4e, whereas the partial charges of corresponding backbone carbonyl oxygen atoms were decreased by 0.4e to maintain the net charge of each residue. For calculating electrostatic scoring grids, the low-dielectric volume of the protein was extended by 1.9Å from the protein surface (based on surface mapping spheres generated by Sphgen). In addition, the low dielectric boundary was extended by 1.0Å from the protein surface for calculating ligand desolvation scoring grids with Solvmap [cite]. The atomic coordinates of MAT-POS-b3e365b9-1 were used to generate 45 matching spheres for ligand placement with DOCK3.8. The performance of the obtained docking grids was evaluated by their ability to enrich 15 previously reported SARS-CoV-2 MPro inhibitors over 650 property matched decoys [cite DUDE-Z] or an Extrema set containing 153,256 molecules with net charges ranging from -2 to +2, molecular weight between 300 and 500 amu. Finally, 862,382,088 neutral compounds with 18-29 heavy atoms from the Enamine REAL chemical library were screened using the ZINC22 database [link]. Molecules with strained

conformations as estimated by the method by Shuo et al. (total strain > 8 TEU, maximum single strain > 3 TEU), were excluded by the docking program. 778,517,250 molecules were successfully scored, each sampled in approximately 836 conformations and 3,439 orientations, leading to the evaluation of roughly 905.8 trillion complexes within 481h on a 1000-core computer cluster.

21,284,498 compounds scored lower than -35 kcal/mol and the poses of top scoring 5,004,192 compounds were extracted. 214,580 compound formed favorable interactions with key residues such as His163, Glu166 and the P2 subpocket, 181,866 of which obtained ECFP4-based TC coefficients of less than 0.35 to the 1,716 known SARS-CoV and SARS-CoV-2 MPro inhibitors reported in the literature (cite: Moonshot, PMC8014119, 10.1021/jm0603926, 10.1038/s41586-020-2223-y, 10.1038/s41586-020-2223-y, 10.1126/science.1085658, <https://doi.org/10.1101/2020.09.15.275891>, PMC1112131, PMC2258912, PMC2745596, PMC3486288, PMC3569073, PMC7098070, PMC7111201, PMC7112044, PMC7119080, PMC7127700, PMC7134594, PMC7164518, PMC7179937, PMC7294525, PMC7571312, PMC7574915, PMC7931627, PMC7979488, PMC8099175, PMC8291137, PMC8353992, PMC8610012). Finally, roughly 9,000 top-ranking compounds were visually inspected and 167 molecules were ordered from Enamine, 146 of which (87.4%) were successfully synthesized.

Covalent molecular docking

Cysteine-reactive warheads of aldehydes, nitriles, and alpha-ketoamides were searched in the ZINC20/Enamine REAL databases of 1.4 billion molecules using their respective SMARTS patterns (ketoamides O=[CR0]([#6])[CR0](=O)N[#6]; aldehydes [CX3H1](=O)[#6]; nitriles [CX4]-C#N). This returned 25.7 million nitriles, 2.5 million aldehydes, and 1.5 million ketoamides. Molecules were filtered to have at least 1 ring, and to be fragment to lead-like molecular weights (<350). Three-dimensional dockable conformations were generated with molecules in their transition-state form and a dummy atom in place for the covalent docking algorithm to indicate

which atom should be modeled covalently bound to the Cys sulfur. Aldehydes were formatted with OH, nitriles with X, and ketoamides had both a negative and a neutral X. Overall, 6.5 million molecules were docked – 3.6 million nitriles, 1.4 million ketoamides, and 1.5 million aldehydes.

The receptor was prepared in BlasterMaster in DOCK3.7. Pose reproduction of the truncated covalent molecule of PDB 6Y2G (smiles of dockable ligand: O=C1NCC[C@H]1CC[C@](O)([SiH3])C(=O)NCc2ccccc2) was checked for the docking setup. Default blastermasted-generated grids were used for electrostatic (radius size 1.9Å) and VDW scoring, and no matching spheres were used in docking calculations as they are not used by the covalent docking DOCKoValent algorithm. For covalent docking, the Cys145 SH was indicated as the anchor for molecules screened. The distance was slightly relaxed from the C-C bond distance to 1.85Å. For His41 protonation, aldehydes, nitriles, and neutral ketoamides used HID, while negative ketoamides used HIP. Each warhead was docked separately with a total 6.5 million molecules screened. Accordingly, each warhead was also processed separately.

For the aldehydes, the top 300,000 ranked molecules were evaluated for torsional strain (cite), and those with a total torsional strain greater than 9.8 (around 3.7 incurred due to strain on atom types on the warhead and this was disregarded, therefore total energy was 6) and single torsional strain greater than 2.5 were excluded (155,386 left). Molecules making more than 1 hydrogen bond to the protein, having no hydrogen bond clashes, no unpaired hydrogen bond donors (56,969 left) were prioritized (cite open eye interaction filter). Remaining molecules were clustered for chemical similarity based on ECFP4-based Tanimoto coefficient (Tc) of 0.5. Viable poses filling the P1', P1 or P2 sites were selected during visual inspection. A total of 35 aldehydes were selected for make-on-demand synthesis of which 27 were successfully synthesized.

For the nitriles, the top 100,000 ranked molecules were evaluated for torsional strain (17,424 left), then interaction filter (6,201 left). Clustered? Lastly, we visually filtered for

favorable to hydrogen bonds formed to His41, Gly143, Thr26, Glu166, or Cys145, of which 41 ordered for parallel synthesis (31 arrived for testing).

For the ketoamides (Shuo) the top 393,000 ranked molecules with scores less than 0.0 were evaluated for torsional strain (121,234 left), than the same interaction filter as nitriles (37,267 left). Clustered? Visual inspection of remaining molecules focused on those making hydrogen bonds with His41, Cys145, Gly143, Thr26. In total 21 molecules were purchased and 16 were successfully synthesized.

Make-on-demand synthesis

X non-covalent and X covalent compounds purchased from docking screens could be successfully synthesized by Enamine, Ltd. for a total fulfilment rate of X%. The purities of molecules were at least X% and typically above X% (SI analytical)

Compound optimization

Optimization of docking hits ZINC346371112, ZINC301553312, ZINC813360541, ZINC553840273, '3620, '0431, '4589, '5103, '5156, '6246, '6792, '0292, '2826/'0892, and '6634/'4072 were attempted and IC50 values can be found in X. Analogs were designed for desired chemical perturbations or searched in SmallWorld and Arthor catalogs and synthesized by Enamine. For '3620, compounds were also designed from the '7356 and '3620 crystal structures and were modeled with covalent docking or with Maestro (v. 2021-X, Schrödinger, LLC) ligand alignment.

Protein purification

As previously described.¹¹

MPro Inhibition assay

A fluorescence-quenched substrate with the sequence H₂N(d-Arg)(d-Arg)-K(MCA)-ATLQAIAS-K(DNP)-COOH was synthesized via the Fmoc solid-phase peptide synthesis as previously described²⁷. Kinetic measurements were carried out in Corning black 384-well flat-bottom plates and read on a BioTek H4 multimode plate reader. The quenched fluorogenic peptide had a final concentration of KM = 12.7 μM, and MPro had a final concentration of 50 nM. The reaction buffer was 20 mM Tris, 150 mM NaCl, 1 mM EDTA, 0.05% Tween-20 (v/v), and 1 mM DTT, pH 7.4. Compounds were incubated with protease prior to substrate addition at 37 °C for 1 h. After incubation, the substrate was added, and kinetic activity was monitored for 1 h at 37 °C. Initial velocities were calculated at 1 to 30 min in RFU/s. Velocities were corrected by subtracting the relative fluorescence of a substrate-only control, and fraction activity was calculated using a substrate-corrected no-inhibitor control where DMSO was added instead of a drug. Kinetics measurements were carried out in triplicate. SARS-CoV-1 and MERS major protease were both purchased from Bio-Techne (catalogue #: E-718-050 and E-719-050, respectively). KM was derived with the NSP7 substrate for each protease (supp figure), which was the substrate concentration used for each protease for comparative dose-response curves. Enzyme concentration was 50nM for SARS-CoV-1 and 100nM for MERS. The same assay buffer described above was used for all kinetic assays with each protease.

Data availability

All crystallographic structures have been deposited in the PDB as <codes>. The identities of compounds docked in non-covalent screens can be found at ZINC15/ZINC20 (<http://zinc15.docking.org> and <http://zinc20.docking.org>) and ZINC22 (< website >). The 30 million covalent compounds have been deposited in covalent2022.docking.org along with their DOCKoalent files. Active compounds may be purchased from Enamine (other vendors?). All other data are available from the corresponding authors on request.

Code availability

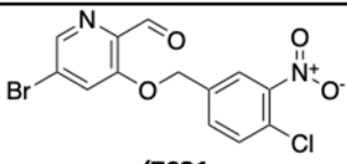
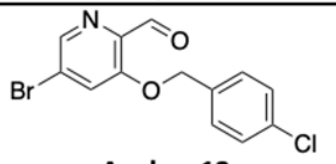
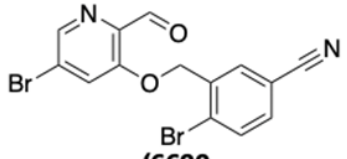
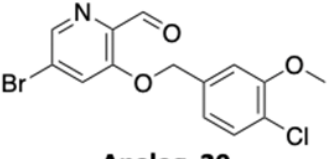
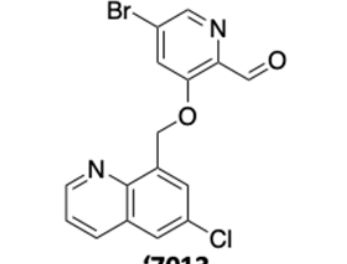
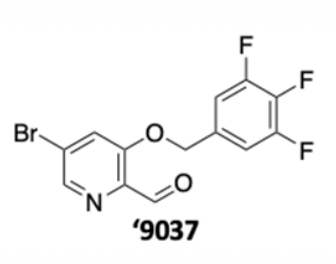
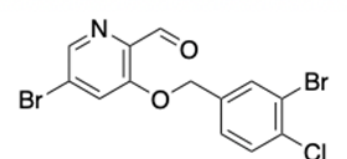
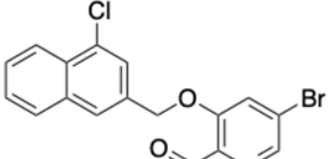
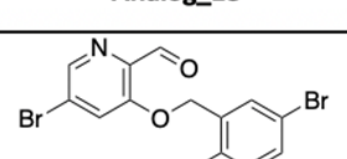
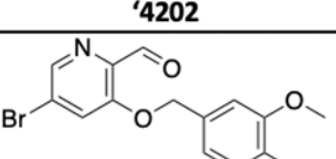
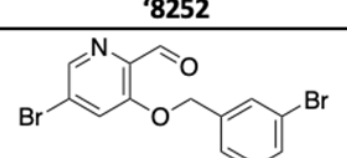
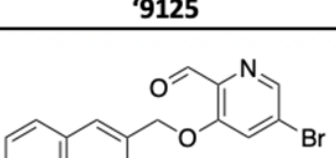
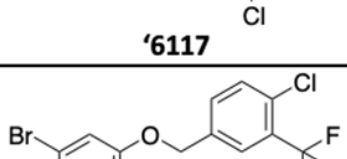
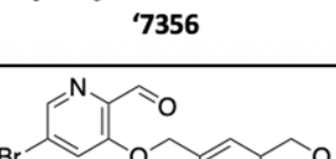
DOCK3.7 and DOCK3.8 are freely available for non-commercial research from the authors; commercial licenses are available via the UC Regents. An open source web-based version of the program is available without restriction to all (<https://blaster.docking.org>), as are the Arthor and Small World analoging tools used in this study.

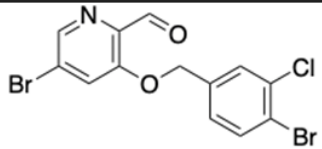
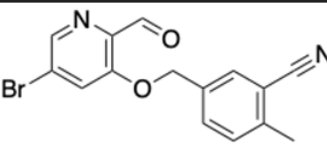
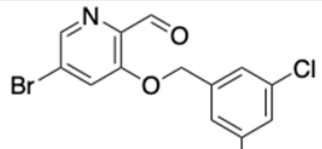
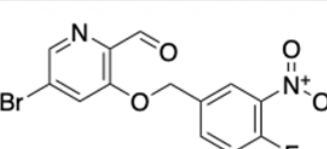
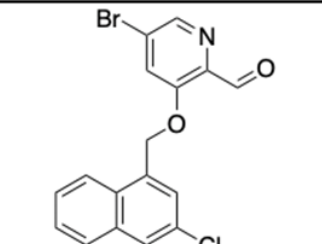
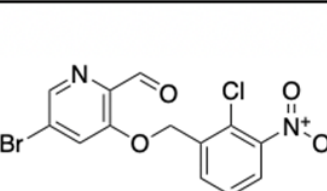
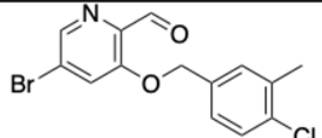
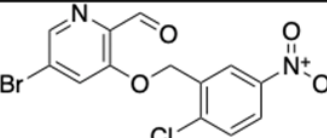
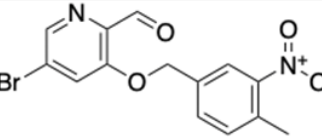
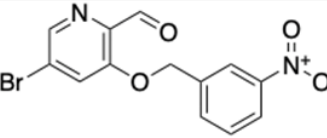
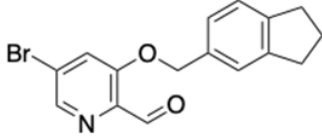
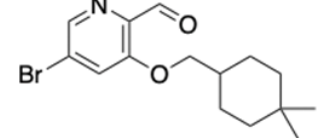
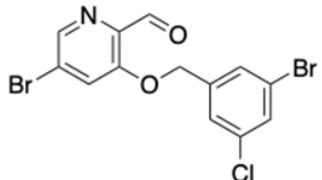
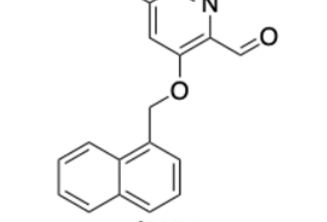
3.6 Supplementary Materials

Table 3.S1: All compound tested from docking screens and compound optimization.

<https://docs.google.com/spreadsheets/d/1QDRiKRKuLjryJVnP5OKZpSSL76Aq8FHt/edit#gid=1443882961>)

Table 3.S2. Analogs of covalent docking hit '3620 with improved potencies.

Compound	IC50 [μ M]	Compound	IC50 [μ M]
 <p>'7021</p>	1	 <p>Analog_12</p>	22
 <p>'6690</p>	2	 <p>Analog_20</p>	22
 <p>'7013</p>	5	 <p>'9037</p>	23
 <p>Analog_18</p>	6	 <p>'4202</p>	24
 <p>'8252</p>	6	 <p>'9125</p>	25
 <p>'6117</p>	7	 <p>'7356</p>	26
 <p>Analog_19</p>	9	 <p>'8474</p>	27

Compound	IC50 [μ M]	Compound	IC50 [μ M]
 <p>'4217</p>	9	 <p>'0481</p>	27
 <p>'9033</p>	9	 <p>Analog_7</p>	28
 <p>'9122</p>	9	 <p>Analog_8</p>	33
 <p>Analog_17</p>	11	 <p>Analog_10</p>	34
 <p>Analog_6</p>	12	 <p>Analog_11</p>	35
 <p>Analog_49</p>	13	 <p>'9009</p>	38
 <p>'0156</p>	14	 <p>'3251</p>	40

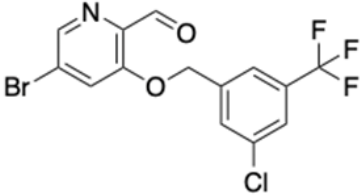
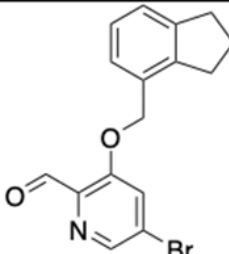
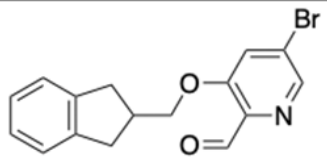
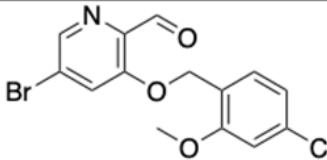
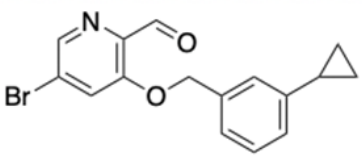
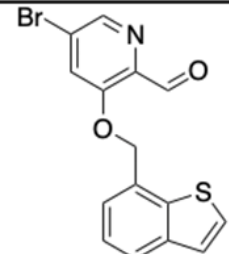
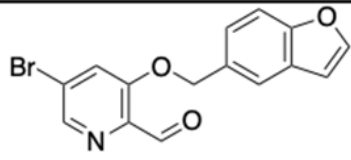
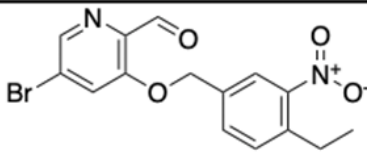
Compound	IC50 [μ M]	Compound	IC50 [μ M]
 <p>'9028</p>	14	 <p>'3250</p>	40
 <p>'4221</p>	19	 <p>Analog_21</p>	43
 <p>'3264</p>	20	 <p>'3252</p>	45
 <p>'4212</p>	20	 <p>'3564</p>	48

Table 3.S3. Antiviral activities.

a Efficacy in RT-qPCR viral infectivity assay in X cells.

b Reduction in cell viability (cytotoxicity).

Compound	Antiviral IC50 ^a [μ M]	Antiviral IC90 ^a [μ M]	CC10 ^b [μ M]
'7021	6.2	7.3	8.03
'7356	19.53	19.9	6.93

Table 3.S4. Pan-viral enzymatic activities of '7021.

Viral MPro	IC50 [μ M]
MERS	50
SARS-CoV-1	8
SARS-CoV-2	1

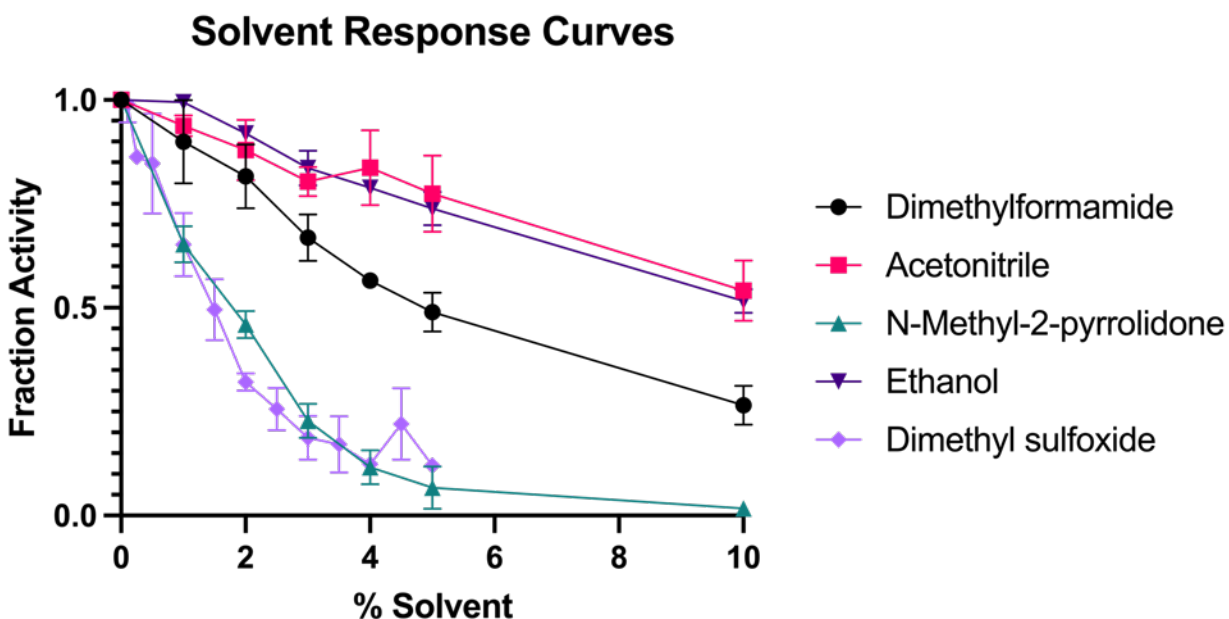


Figure 3.S1: Solvent effect on enzymatic activity

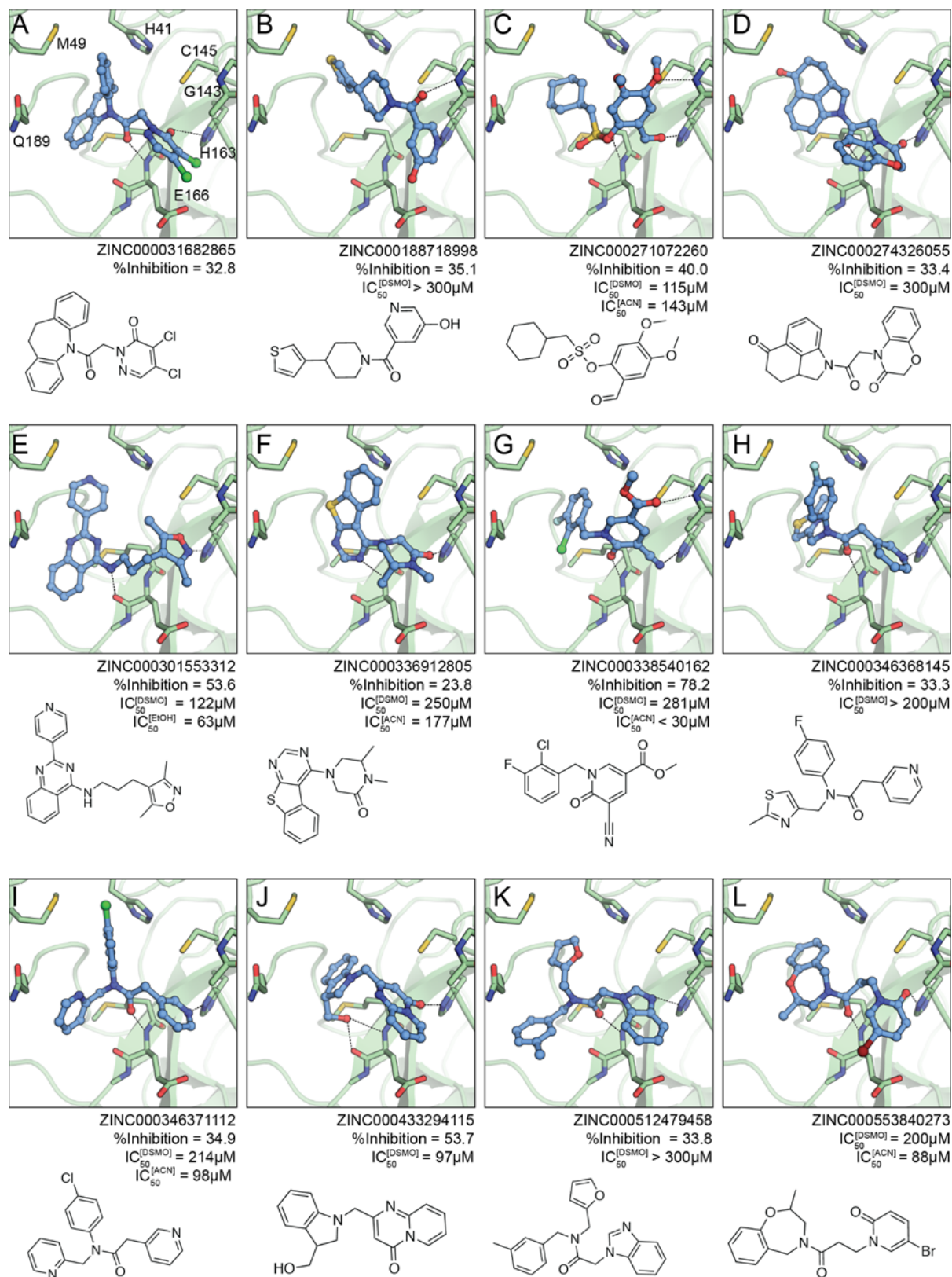


Figure 3.S2.1: Non-covalent docking hits from first virtual screen.

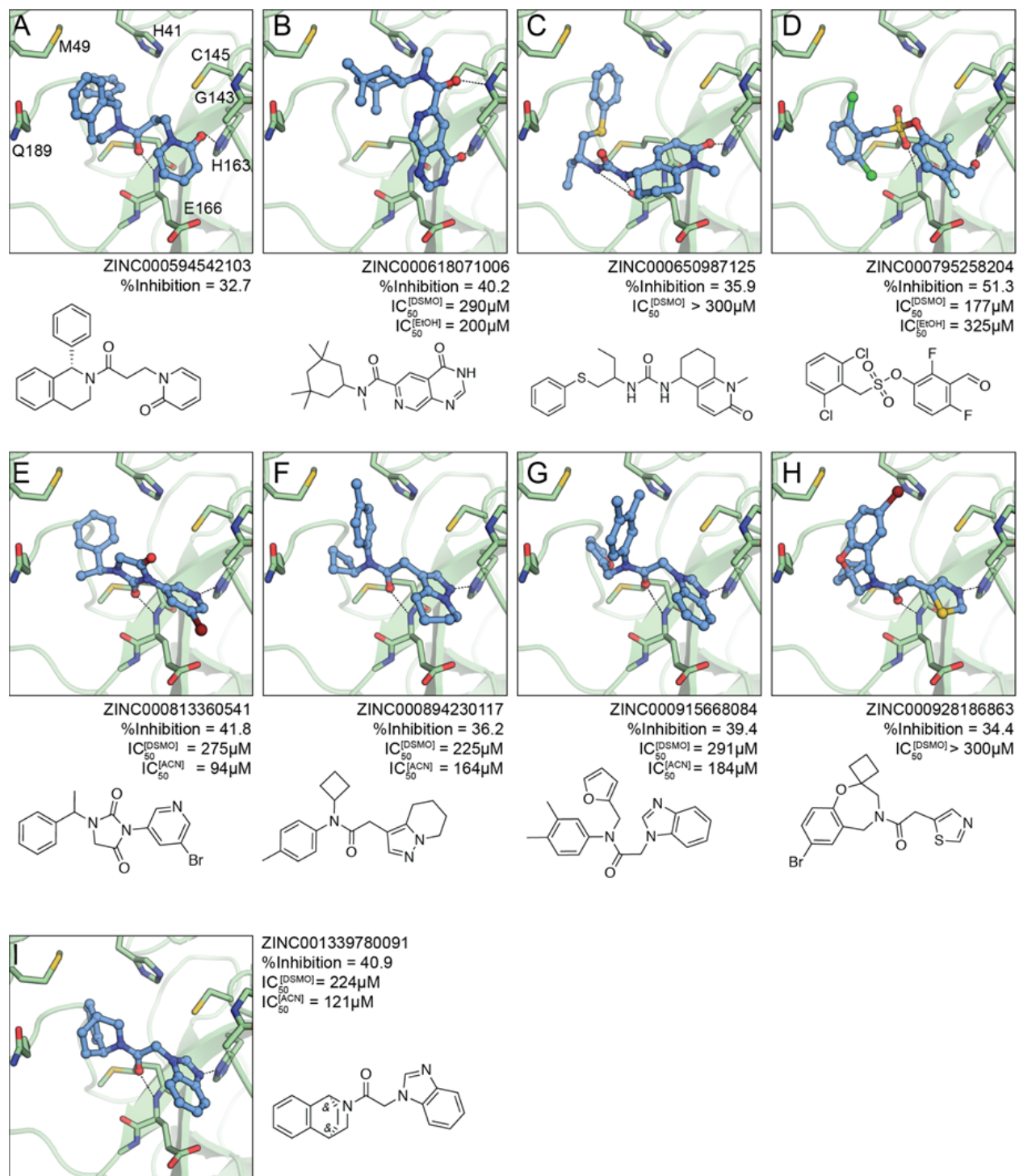


Figure 3.S2.2: Non-covalent docking hits from first virtual screen.

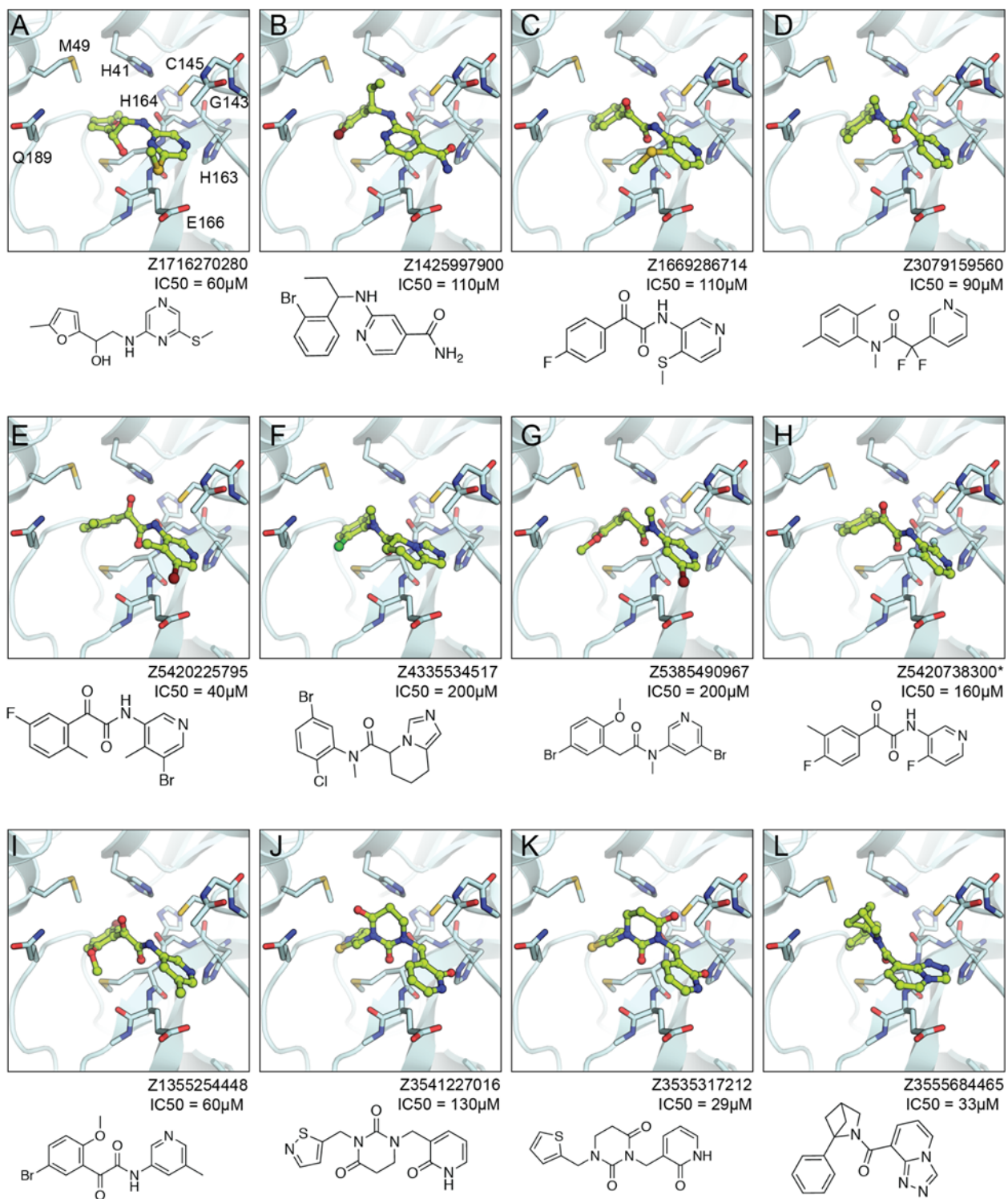


Figure 3.S2.3: Non-covalent docking hits from second virtual screen

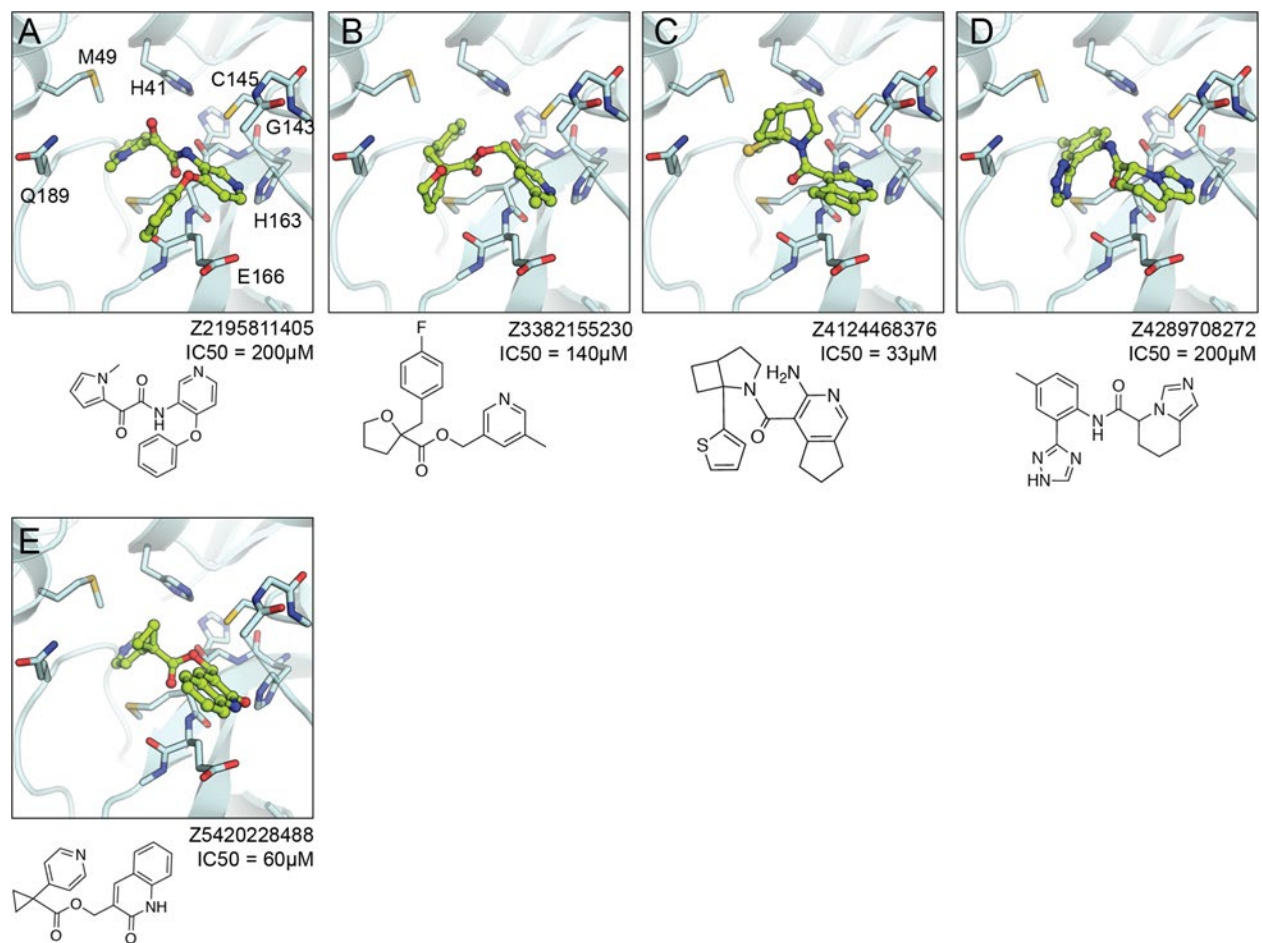


Figure 3.S2.4: Non-covalent docking hits from second virtual screen.

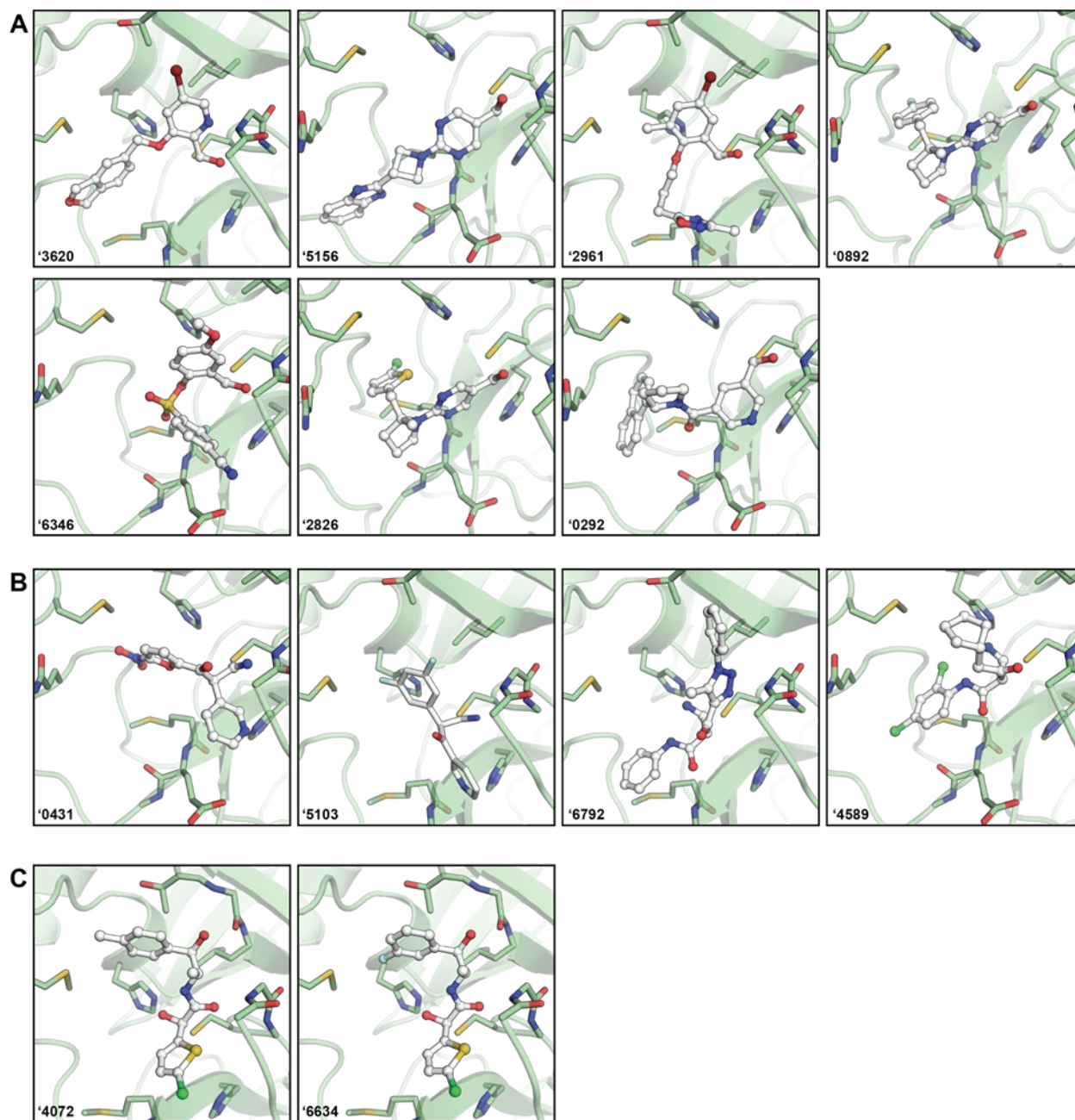


Figure 3.S3: Docked poses of covalent hits. (A) Aldehydes. (B) Nitriles. (C) Ketoamides. Covalent bonds between the warhead and Cys145 and not explicitly modeled in docking.

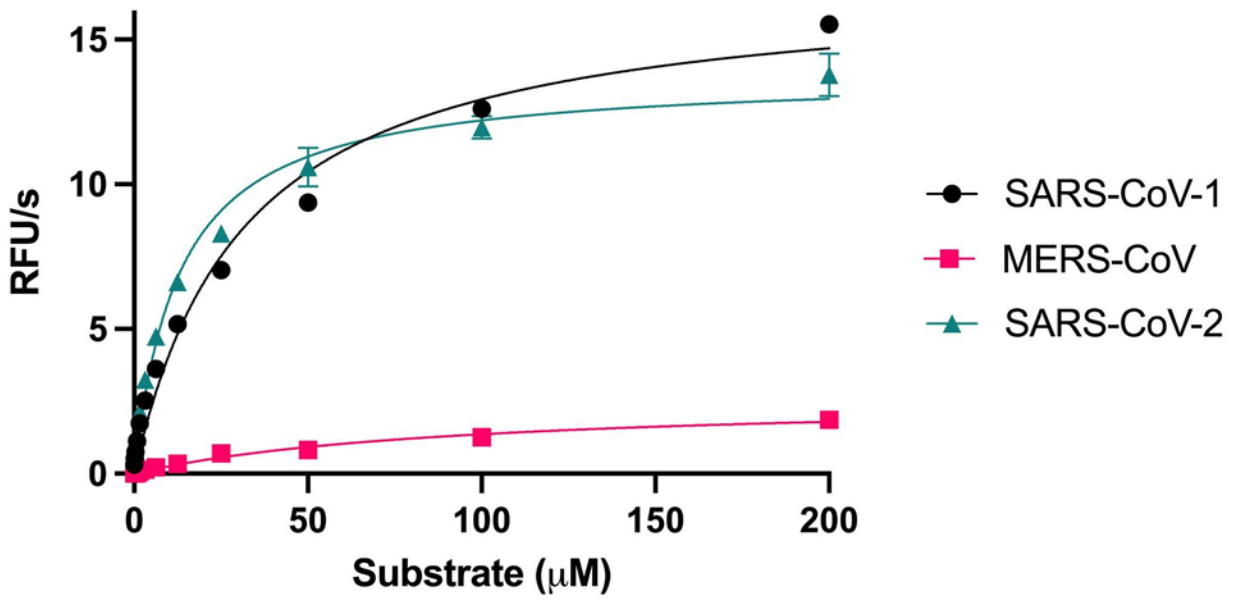


Figure 3.S4: Pan-viral enzymatic activities.

3.7 References

- (1) Owen, D. R.; Allerton, C. M. N.; Anderson, A. S.; Aschenbrenner, L.; Avery, M.; Berritt, S.; Boras, B.; Cardin, R. D.; Carlo, A.; Coffman, K. J.; Dantonio, A.; Di, L.; Eng, H.; Ferre, R.; Gajiwala, K. S.; Gibson, S. A.; Greasley, S. E.; Hurst, B. L.; Kadar, E. P.; Kalgutkar, A. S.; Lee, J. C.; Lee, J.; Liu, W.; Mason, S. W.; Noell, S.; Novak, J. J.; Obach, R. S.; Ogilvie, K.; Patel, N. C.; Pettersson, M.; Rai, D. K.; Reese, M. R.; Sammons, M. F.; Sathish, J. G.; Singh, R. S. P.; Steppan, C. M.; Stewart, A. E.; Tuttle, J. B.; Updyke, L.; Verhoest, P. R.; Wei, L.; Yang, Q.; Zhu, Y. An Oral SARS-CoV-2 Mpro Inhibitor Clinical Candidate for the Treatment of COVID-19. *Science* **2021**, 374 (6575), 1586–1593. <https://doi.org/10.1126/science.abl4784>.
- (2) Unoh, Y.; Uehara, S.; Nakahara, K.; Nobori, H.; Yamatsu, Y.; Yamamoto, S.; Maruyama, Y.; Taoda, Y.; Kasamatsu, K.; Suto, T.; Kouki, K.; Nakahashi, A.; Kawashima, S.; Sanaki, T.; Toba, S.; Uemura, K.; Mizutare, T.; Ando, S.; Sasaki, M.; Orba, Y.; Sawa, H.; Sato, A.; Sato, T.; Kato, T.; Tachibana, Y. Discovery of S-217622, a Noncovalent Oral SARS-CoV-2 3CL Protease Inhibitor Clinical Candidate for Treating COVID-19. *J. Med. Chem.* **2022**, 65 (9), 6499–6512. <https://doi.org/10.1021/acs.jmedchem.2c00117>.
- (3) Zhang, C.-H.; Spasov, K. A.; Reilly, R. A.; Hollander, K.; Stone, E. A.; Ippolito, J. A.; Liosi, M.-E.; Deshmukh, M. G.; Tirado-Rives, J.; Zhang, S.; Liang, Z.; Miller, S. J.; Isaacs, F.; Lindenbach, B. D.; Anderson, K. S.; Jorgensen, W. L. Optimization of Triarylpyridinone Inhibitors of the Main Protease of SARS-CoV-2 to Low-Nanomolar Antiviral Potency. *ACS Med. Chem. Lett.* **2021**, 12 (8), 1325–1332. <https://doi.org/10.1021/acsmchemlett.1c00326>.
- (4) Zhang, C.-H.; Stone, E. A.; Deshmukh, M.; Ippolito, J. A.; Ghahremanpour, M. M.; Tirado-Rives, J.; Spasov, K. A.; Zhang, S.; Takeo, Y.; Kudalkar, S. N.; Liang, Z.; Isaacs, F.; Lindenbach, B.; Miller, S. J.; Anderson, K. S.; Jorgensen, W. L. Potent Noncovalent Inhibitors of the Main Protease of SARS-CoV-2 from Molecular Sculpting of the Drug

- Perampanel Guided by Free Energy Perturbation Calculations. *ACS Cent. Sci.* **2021**, 7 (3), 467–475. <https://doi.org/10.1021/acscentsci.1c00039>.
- (5) Ge, R.; Shen, Z.; Yin, J.; Chen, W.; Zhang, Q.; An, Y.; Tang, D.; Satz, A. L.; Su, W.; Kuai, L. Discovery of SARS-CoV-2 Main Protease Covalent Inhibitors from a DNA-Encoded Library Selection. *SLAS Discov.* **2022**, 27 (2), 79–85. <https://doi.org/10.1016/j.slasd.2022.01.001>.
- (6) Dai, W.; Zhang, B.; Jiang, X.-M.; Su, H.; Li, J.; Zhao, Y.; Xie, X.; Jin, Z.; Peng, J.; Liu, F.; Li, C.; Li, Y.; Bai, F.; Wang, H.; Cheng, X.; Cen, X.; Hu, S.; Yang, X.; Wang, J.; Liu, X.; Xiao, G.; Jiang, H.; Rao, Z.; Zhang, L.-K.; Xu, Y.; Yang, H.; Liu, H. Structure-Based Design of Antiviral Drug Candidates Targeting the SARS-CoV-2 Main Protease. *Science* **2020**, 368 (6497), 1331–1335. <https://doi.org/10.1126/science.abb4489>.
- (7) Ma, C.; Sacco, M. D.; Hurst, B.; Townsend, J. A.; Hu, Y.; Szeto, T.; Zhang, X.; Tabet, B.; Marty, M. T.; Chen, Y.; Wang, J. Boceprevir, GC-376, and Calpain Inhibitors II, XII Inhibit SARS-CoV-2 Viral Replication by Targeting the Viral Main Protease. *Cell Res.* **2020**, 30 (8), 678–692. <https://doi.org/10.1038/s41422-020-0356-z>.
- (8) Lutgens, A.; Gullberg, H.; Abdurakhmanov, E.; Vo, D. D.; Akaberi, D.; Talibov, V. O.; Nekhotiaeva, N.; Vangeel, L.; De Jonghe, S.; Jochmans, D.; Krambrich, J.; Tas, A.; Lundgren, B.; Gravenfors, Y.; Craig, A. J.; Atilaw, Y.; Sandström, A.; Moodie, L. W. K.; Lundkvist, Å.; van Hemert, M. J.; Neyts, J.; Lennerstrand, J.; Kihlberg, J.; Sandberg, K.; Danielson, U. H.; Carlsson, J. Ultralarge Virtual Screening Identifies SARS-CoV-2 Main Protease Inhibitors with Broad-Spectrum Activity against Coronaviruses. *J. Am. Chem. Soc.* **2022**, 144 (7), 2905–2920. <https://doi.org/10.1021/jacs.1c08402>.
- (9) Goetz, D. H.; Choe, Y.; Hansell, E.; Chen, Y. T.; McDowell, M.; Jonsson, C. B.; Roush, W. R.; McKerrow, J.; Craik, C. S. Substrate Specificity Profiling and Identification of a New Class of Inhibitor for the Major Protease of the SARS Coronavirus ., *Biochemistry* **2007**, 46 (30), 8744–8752. <https://doi.org/10.1021/bi0621415>.

- (10) Jin, Z.; Du, X.; Xu, Y.; Deng, Y.; Liu, M.; Zhao, Y.; Zhang, B.; Li, X.; Zhang, L.; Peng, C.; Duan, Y.; Yu, J.; Wang, L.; Yang, K.; Liu, F.; Jiang, R.; Yang, X.; You, T.; Liu, X.; Yang, X.; Bai, F.; Liu, H.; Liu, X.; Guddat, L. W.; Xu, W.; Xiao, G.; Qin, C.; Shi, Z.; Jiang, H.; Rao, Z.; Yang, H. Structure of Mpro from SARS-CoV-2 and Discovery of Its Inhibitors. *Nature* **2020**, 582 (7811), 289–293. <https://doi.org/10.1038/s41586-020-2223-y>.
- (11) Zhang, L.; Lin, D.; Sun, X.; Curth, U.; Drosten, C.; Sauerhering, L.; Becker, S.; Rox, K.; Hilgenfeld, R. Crystal Structure of SARS-CoV-2 Main Protease Provides a Basis for Design of Improved α -Ketoamide Inhibitors. *Science* **2020**, 368 (6489), 409–412. <https://doi.org/10.1126/science.abb3405>.
- (12) Jacobs, J.; Grum-Tokars, V.; Zhou, Y.; Turlington, M.; Saldanha, S. A.; Chase, P.; Egger, A.; Dawson, E. S.; Baez-Santos, Y. M.; Tomar, S.; Mielech, A. M.; Baker, S. C.; Lindsley, C. W.; Hodder, P.; Mesecar, A.; Stauffer, S. R. Discovery, Synthesis, and Structure-Based Optimization of a Series of N-(Tert-Butyl)-2-(N-Arylamido)-2-(Pyridin-3-Yl) Acetamides (ML188) as Potent Noncovalent Small Molecule Inhibitors of the Severe Acute Respiratory Syndrome Coronavirus (SARS-CoV) 3CL Protease. *J. Med. Chem.* **2013**, 56 (2), 534–546. <https://doi.org/10.1021/jm301580n>.
- (13) Bender, B. J.; Gahbauer, S.; Lutgens, A.; Lyu, J.; Webb, C. M.; Stein, R. M.; Fink, E. A.; Balius, T. E.; Carlsson, J.; Irwin, J.; Shoichet, B. K. A Practical Guide to Large-Scale Docking. *Nat Protoc* **2021**. <https://doi.org/10.1038/s41596-021-00597-z>.
- (14) Sterling, T.; Irwin, J. J. ZINC 15 – Ligand Discovery for Everyone. *J. Chem. Inf. Model.* **2015**, 55 (11), 2324–2337. <https://doi.org/10.1021/acs.jcim.5b00559>.
- (15) Gu, S.; Smith, M. S.; Yang, Y.; Irwin, J. J.; Shoichet, B. K. Ligand Strain Energy in Large Library Docking; preprint; *Bioinformatics*, **2021**. <https://doi.org/10.1101/2021.04.06.438722>.
- (16) Irwin, J. J.; Tang, K. G.; Young, J.; Dandarchuluun, C.; Wong, B. R.; Khurelbaatar, M.; Moroz, Y. S.; Mayfield, J.; Sayle, R. A. ZINC20—A Free Ultralarge-Scale Chemical

- Database for Ligand Discovery. *J. Chem. Inf. Model.* **2020**, 60 (12), 6065–6073.
<https://doi.org/10.1021/acs.jcim.0c00675>.
- (17) Stein, R. M.; Yang, Y.; Balias, T. E.; O'Meara, M. J.; Lyu, J.; Young, J.; Tang, K.; Shoichet, B. K.; Irwin, J. J. Property-Unmatched Decoys in Docking Benchmarks. *J. Chem. Inf. Model.* **2021**, 61 (2), 699–714. <https://doi.org/10.1021/acs.jcim.0c00598>.
- (18) London, N.; Miller, R. M.; Krishnan, S.; Uchida, K.; Irwin, J. J.; Eidam, O.; Gibold, L.; Cimermančič, P.; Bonnet, R.; Shoichet, B. K.; Taunton, J. Covalent Docking of Large Libraries for the Discovery of Chemical Probes. *Nat. Chem. Biol.* **2014**, 10 (12), 1066–1072. <https://doi.org/10.1038/nchembio.1666>.
- (19) Wang, S.; Wacker, D.; Levit, A.; Che, T.; Betz, R. M.; McCorvy, J. D.; Venkatakrisnan, A. J.; Huang, X.-P.; Dror, R. O.; Shoichet, B. K.; Roth, B. L. D 4 Dopamine Receptor High-Resolution Structures Enable the Discovery of Selective Agonists. *Science* **2017**, 358 (6361), 381–386. <https://doi.org/10.1126/science.aan5468>.
- (20) Lyu, J.; Wang, S.; Balias, T. E.; Singh, I.; Levit, A.; Moroz, Y. S.; O'Meara, M. J.; Che, T.; Alga, E.; Tolmachova, K.; Tolmachev, A. A.; Shoichet, B. K.; Roth, B. L.; Irwin, J. J. Ultra-Large Library Docking for Discovering New Chemotypes. *Nature* **2019**, 566 (7743), 224–229. <https://doi.org/10.1038/s41586-019-0917-9>.
- (21) Stein, R. M.; Kang, H. J.; McCorvy, J. D.; Glatfelter, G. C.; Jones, A. J.; Che, T.; Slocum, S.; Huang, X.-P.; Savych, O.; Moroz, Y. S.; Stauch, B.; Johansson, L. C.; Cherezov, V.; Kenakin, T.; Irwin, J. J.; Shoichet, B. K.; Roth, B. L.; Dubocovich, M. L. Virtual Discovery of Melatonin Receptor Ligands to Modulate Circadian Rhythms. *Nature* **2020**, 579 (7800), 609–614. <https://doi.org/10.1038/s41586-020-2027-0>.
- (22) Alon, A.; Lyu, J.; Braz, J. M.; Tummino, T. A.; Craik, V.; O'Meara, M. J.; Webb, C. M.; Radchenko, D. S.; Moroz, Y. S.; Huang, X.-P.; Liu, Y.; Roth, B. L.; Irwin, J. J.; Basbaum, A. I.; Shoichet, B. K.; Kruse, A. C. Crystal Structures of the σ 2 Receptor Template

- Large-Library Docking for Selective Chemotypes Active in Vivo; preprint; *Pharmacology and Toxicology*, **2021**. <https://doi.org/10.1101/2021.04.29.441652>.
- (23) Babaoglu, K.; Simeonov, A.; Irwin, J. J.; Nelson, M. E.; Feng, B.; Thomas, C. J.; Cancian, L.; Costi, M. P.; Maltby, D. A.; Jadhav, A.; Inglese, J.; Austin, C. P.; Shoichet, B. K. Comprehensive Mechanistic Analysis of Hits from High-Throughput and Docking Screens against β -Lactamase. *J. Med. Chem.* **2008**, 51 (8), 2502–2511. <https://doi.org/10.1021/jm701500e>.
- (24) Schuller, M.; Correy, G. J.; Gahbauer, S.; Fearon, D.; Wu, T.; Díaz, R. E.; Young, I. D.; Carvalho Martins, L.; Smith, D. H.; Schulze-Gahmen, U.; Owens, T. W.; Deshpande, I.; Merz, G. E.; Thwin, A. C.; Biel, J. T.; Peters, J. K.; Moritz, M.; Herrera, N.; Kratochvil, H. T.; QCRG Structural Biology Consortium; Aimon, A.; Bennett, J. M.; Brandao Neto, J.; Cohen, A. E.; Dias, A.; Douangamath, A.; Dunnett, L.; Fedorov, O.; Ferla, M. P.; Fuchs, M. R.; Gorrie-Stone, T. J.; Holton, J. M.; Johnson, M. G.; Krojer, T.; Meigs, G.; Powell, A. J.; Rack, J. G. M.; Rangel, V. L.; Russi, S.; Skyner, R. E.; Smith, C. A.; Soares, A. S.; Wierman, J. L.; Zhu, K.; O'Brien, P.; Jura, N.; Ashworth, A.; Irwin, J. J.; Thompson, M. C.; Gestwicki, J. E.; von Delft, F.; Shoichet, B. K.; Fraser, J. S.; Ahel, I. Fragment Binding to the Nsp3 Macrodomein of SARS-CoV-2 Identified through Crystallographic Screening and Computational Docking. *Sci. Adv.* **2021**, 7 (16), eabf8711. <https://doi.org/10.1126/sciadv.abf8711>.
- (25) Korczynska, M.; Clark, M. J.; Valant, C.; Xu, J.; Moo, E. V.; Albold, S.; Weiss, D. R.; Torosyan, H.; Huang, W.; Kruse, A. C.; Lyda, B. R.; May, L. T.; Baltos, J.-A.; Sexton, P. M.; Kobilka, B. K.; Christopoulos, A.; Shoichet, B. K.; Sunahara, R. K. Structure-Based Discovery of Selective Positive Allosteric Modulators of Antagonists for the M₂ Muscarinic Acetylcholine Receptor. *Proc. Natl. Acad. Sci.* **2018**, 115 (10). <https://doi.org/10.1073/pnas.1718037115>.

- (26) Huang, X.-P.; Karpiak, J.; Kroeze, W. K.; Zhu, H.; Chen, X.; Moy, S. S.; Sadoris, K. A.; Nikolova, V. D.; Farrell, M. S.; Wang, S.; Mangano, T. J.; Deshpande, D. A.; Jiang, A.; Penn, R. B.; Jin, J.; Koller, B. H.; Kenakin, T.; Shoichet, B. K.; Roth, B. L. Allosteric Ligands for the Pharmacologically Dark Receptors GPR68 and GPR65. *Nature* **2015**, 527 (7579), 477–483. <https://doi.org/10.1038/nature15699>.
- (27) Zhao, N.; Bardine, C.; Lourenço, A. L.; Wang, Y.-H.; Huang, Y.; Cleary, S. J.; Wilson, D. M.; Oh, D. Y.; Fong, L.; Looney, M. R.; Evans, M. J.; Craik, C. S. In Vivo Measurement of Granzyme Proteolysis from Activated Immune Cells with PET. *ACS Cent. Sci.* **2021**, 7 (10), 1638–1649. <https://doi.org/10.1021/acscentsci.1c00529>.

Publishing Agreement

It is the policy of the University to encourage open access and broad distribution of all theses, dissertations, and manuscripts. The Graduate Division will facilitate the distribution of UCSF theses, dissertations, and manuscripts to the UCSF Library for open access and distribution. UCSF will make such theses, dissertations, and manuscripts accessible to the public and will take reasonable steps to preserve these works in perpetuity.

I hereby grant the non-exclusive, perpetual right to The Regents of the University of California to reproduce, publicly display, distribute, preserve, and publish copies of my thesis, dissertation, or manuscript in any form or media, now existing or later derived, including access online for teaching, research, and public service purposes.

DocuSigned by:

Conner Baldoni

052D5AE1031B414...

Author Signature

7/17/2022

Date